RANS CFD Based Analysis of Low Speed Wind Tunnel Tare and Interference and Wall Corrections for Supersonic Aircraft Configurations

Kenneth C. Wiersema

A thesis
submitted in partial fulfillment of the
requirements for the degree of

Masters of Science in Aeronautics and Astronautics

University of Washington

2026

Committee:

Eli Livne

Chester Nelson

Program Authorized to Offer Degree:
Aeronautics and Astronautics

University of Washington

Abstract

RANS CFD Based Analysis of Low Speed Wind Tunnel Tare and Interference and Wall Corrections for Supersonic Aircraft Configurations

Kenneth C. Wiersema

Chair of the Supervisory Committee:
Professor Eli Livne
Aeronautics & Astronautics

RANS CFD simulations were used to analyze the low speed wind tunnel corrections that were applied to the wind tunnel tests of a proposed commercial supersonic transport aircraft. The wind tunnel data used as reference and comparison for the CFD simulations was generated from the NASA SCALOS program's testing at the University of Washington's Kirsten Wind Tunnel. Three different configurations were studied, a cranked delta wing, and two full 3-surface configurations: a low tail and a T-tail. A series of simulations with the wind tunnel models in free air were performed to provide a baseline comparison between the fully corrected wind tunnel data and the CFD free air simulations. A CFD investigation into the 3-step T&I process used to remove the effects of the model mounting system was performed. The CFD investigation consisted of simulating all 3 of the steps of the experimental T&I process: upright, inverted, and inverted with image support system. The 3-step process was then applied to the CFD simulations and was compared to a direct simulation of model in the tunnel without the support system present. The results showed that the T&I process matched closely with a simulation of the model without the support system in the tunnel. Following, an analysis of Shindo's wall and blockage corrections was performed to determine how well these traditional corrections apply to the large delta wings typical for supersonic aircraft configurations. It was found that the wall corrections produced from CFD generally produced corrections of greater magnitudes than the conventional methods suggested for this class of aircraft geometries.

TABLE OF CONTENTS

LIST OF FIGURES

LIST OF TABLES

NOMENCLATURE

Variables

α: Pitch Angle, angle of attack (degrees)

β: Yaw Angle, side slip angle (degrees)

C_L: Coefficient of Lift

C_D: Coefficient of Drag

C_M: Coefficient of Pitching Moment

C_Y: Coefficient of Side Force

C_R: Coefficient of Rolling Moment

C_N: Coefficient of Yawing Moment

Λ_{LE}: Leading Edge Sweep Angle (degrees)

Γ: Dihedral Angle (degrees)

b: Wing Span (feet)

c: Mean Aerodynamic Chord (feet)

c_{ref}: Longitudinal Reference length (in)

b_{ref}: Lateral Reference span (in)

S_{ref}: Wing Reference Area (feet^2)

t/c_{max}: Max Airfoil Thickness

AR: Aspect Ratio

d: maximum diameter

l: length

$S_{wet,ext}$: External Wetted Area (feet^2)

S_f: Frontal Projected Area (feet^2)

$S_{wet,int}$: Internal Wetted Area (feet^2)

y: Distance from the wall (ft)

y^+: Dimensionless distance from the wall

Re: Reynolds Number

u: Velocity (ft/s)

$\bar{u}$: Average fluid velocity (ft/s)

u': Instantaneous fluid velocity (ft/s)

Abbreviations

AOA: Angle of Attack

SA: Spalart-Allmaras Turbulence model

SST: Menter Shear Stress Turbulence model

KWT: Kirsten Wind Tunnel

RANS: Reynolds Average Navier Stokes

SCALOS: Supersonic Configurations at Low Speeds

T&I: Tare and Interference

RUAV: Research Unmanned Aerial Vehicle

BMC: Balance Moment Center

MMC: Model Moment Center

CFD: Computational Fluid Dynamics

CAD: Computer Aided Design

MSS: Model Support System

Model Configuration Names

"Step A": Model upright on the model support system inside the wind tunnel

"Step B": Model inverted on the model support system inside the wind tunnel

"Step C": Model inverted on the model support system with image fairing inside the wind tunnel

"Step D": Model upright inside the wind tunnel without the model support system

"Free Air": A simulation of the wind tunnel model alone without the presence of the tunnel

ACKNOWLEDGMENTS

Firstly, I would like to acknowledge Dr. Eli Livne for his guidance and assistance through both my undergraduate and graduate experiences at UW, and for taking me on as a member of the SCALOS team after my time with the SCALOS project as an undergraduate. Additionally, I would like to thank Chet Nelson for his knowledge and guidance on both creating the final configuration of the RSAC for the final SCALOS contractor report and his guidance on interpreting the CFD results within and knowledge of supersonic aircraft configurations. Additionally, I would like to thank Eddie Ting as my Ph.D student mentor and providing me with guidance as a graduate student and assisting with processing the SCALOS data. I would like to thank the Kirsten Wind Tunnel as whole for providing the wind tunnel and correction process for the SCALOS project and providing me with employment during my time as a Master's student. Several of the ideas in this paper wouldn't have fully come to fruition without my time spent at the tunnel. Specifically of the KWT crew, I would like to thank Miguel Salguero for his inputs and opinions on my work for both my master's thesis and the tunnel as a whole, and Stuart Dickson for assisting with the SCALOS reduction. Finally, I would like to acknowledge the resources of the University of Washington's supercomputer Hyak where I ran the CFD simulations presented in this thesis.

Chapter 1

INTRODUCTION

1.1 Background

The work presented here was an addition and extension of the University of Washington's contribution to the NASA-funded Supersonic Configurations At LOw Speeds (SCALOS) research project. The objective of the SCALOS project was to investigate the low speed performance and stability of proposed conceptual designs for long-range supersonic cruise aircraft, including commercial supersonic transports (SST). The University of Washington's contributions to the project included semi-parametric model geometries, collection of an extensive wind tunnel database, and the definition of a representative supersonic airliner concept [1]. The rationale behind the study was that most research and investigation of supersonic aircraft focus on the high speed aspects of the design, but many design considerations for high speed flight have negative impacts on the low speed flight performance and stability. With the wind tunnel testing comes the need for a set of post-test "corrections" that need to be applied to the measured data in order to remove the presence and effects of the model being and attached to the tunnel. This includes the model mounting system and the presence of the tunnel walls constricting and redirecting the flow around and behind the model. The model support system connects the model to the balance that measures the forces and moments on the model and is necessary for testing, but unwanted for the final results. Without corrections, the forces and moments measured directly by the wind tunnel balance include both the aerodynamic forces on the model supports themselves and the interference of the support with the air flowing over the model. While the Kirsten Wind Tunnel has a standard set of tares for estimating the forces and moments of the model support, and a set of blockage and wall corrections that were developed using a relatively thick, medium aspect ratio, unswept wing providing data more appropriate for conventional subsonic aircraft, and not the low aspect ratio delta wing configurations that SST's posses.

To analyze the validity of the standard wind tunnel corrections Computational Fluid Dynamics

(CFD) was employed to produce comparisons and calibrations that would be impossible to test physically. These are the wind tunnel model in free-stream conditions or the model in the test section without a support system to act as a simulated answer for what the corrections should produce as the final model.

1.2 Methodology

To analyze the validity of the wind tunnel corrections on the supersonic aircraft, a series of CFD simulations were preformed to replicated the effects of the corrections. These simulation were both performed to replicated the measured wind tunnel data and to provide the results of the corrections and compare the effects generated from the normal wind tunnel corrections and what is predicted in CFD.

1.2.1 Turbulence Methods Comparison

As a consequence of using a RANS CFD code (see Chapter 3 for the theoretical details) a turbulence model must be used to close the system of equations. It's often referenced that turbulence models "... the choice of turbulence model is oftentimes analogous to the choice of political party or religion" [2]. This doesn't mean that turbulence models are entirely arbitrary choices, some will perform far better than others in certain circumstances. For exterior aerodynamic configuration analysis and general purposes, both the Spalart-Allmaras (SA) one equation turbulence model, and the Menter-Shear Stress Turbulence (SST) model, a two equation model, are considered to perform well. For most simulations, there was a comparison between two different turbulence models, without much discussion to their different variants. The comparison between them in terms of accuracy is the primary focus point that is discussed when comparing the different results and seeing corrections generated using different turbulence models.

1.2.2 Free-Air Analysis of Aircraft Models

The simplest check of the wind tunnel correction process is to simulate the wind tunnel model in "Free-Air", where the edge of the computational domain is very far away from the model and there is no presence of the support system. The simulations performed here were selected to provide some initial calibration and study of some of the behaviors of the models before looking at simulations of the models in the test section and analyzing their performance. Additionally the build up of one of the model was accessed in comparison to the wind tunnel results to analyze an offset in the pitching moment curve that was not present in a wing alone simulation of the model. The differences between the CFD simulations and the wind tunnel results provide the motivation to analyze the correction process step by step to see where the discrepancies between the wind tunnel test and the CFD simulations occur. The three main corrections under analysis of the wind tunnel's data reduction process is the strut tare, discussed under the 3-Step Tare and Interference, the blockage correction and the wall effects correction, both combined in the wall effects section.

1.2.3 The Three Step Tare and Interference Process

The three-step Tare and Interference (T&I) correction is a process used to remove the effects of the model mounting system. The "tare" element represents the direct lift drag and moments of the supports themselves. The "interference" term represents both the aerodynamic flow changes induced by the support's presence on the test configuration, and the aircraft's flow-field's perturbation of the flow around the support which impacts the "tare". Accordingly, the three-step T&I process is more complicated beyond a simple tare of subtracting a model support system tare, where the support system without the model is run and then subtracted from the data of the model and the support system. However, this method only serves to remove the intrinsic properties of the support system itself and not how it may effect the flow field around the model. These effects change greatly from support system to support system and model to model, so creating a generic strut tare is a compromise. With most of the prior testing at the KWT being done with high aspect-ratio conventional wings, so the effects of the model support system on a low aspect-ratio delta wing has not be well quantified. The typical T&I process is detailed in Pope, Barlow and Rae's Low Speed Wind Tunnel Testing textbook [3].

The more complicated method of the 3-Step Tare and Interference (T&I) correction is to run three different model orientations in the tunnel, and then add and subtract them to remove the effect of the model supporting system. The first step of the T&I process, called "Step A", is the standard upright configuration of the model on the test stand that the bulk of the testing would be performed with, shown in Fig. 1.1a. "Step A" has the bottom side of the model occluded and the top of the model unobstructed. The "Step B" is inverting the model on the support system so that the model is upside-down shown in Fig. 1.1b. The top of the model is obstructed while the bottom surface is unobstructed. The third step, "Step C" is where the model is inverted with an image fairing and model support system mounted from the ceiling, mirroring the normal model support system and fairing. "Step C" is shown in Fig. 1.1c. The "Step C" has both the top and bottom of the wind tunnel model occluded by the support systems. The process is to then add "Steps A" and "Step B" together and then subtract "Step C" from them, shown in Eq. 1.1. The final result from the process is called "Step D" shown in Fig. 1.1d where the model is in the test section without the support system.

$$A + B - C = D \tag{1.1}$$

Noting that the angle of attack for "Step B" and "Step C" need to be flipped to match the coordinate system of step A for proper comparisons. The rational behind this is that through the linear sum of "Step A" and "Step B", there are one full set of unobstructed surfaces and one set of obstructed surfaces, and subtracting one full set of obstructed surfaces will leave behind one set of unobstructed surfaces, leaving a model that does not have the effects of the support system included. However, this process is linear and in general very few things with fluid dynamics are linear. Each step of the process (A,B,C,D) will be simulated individually and then compared against the wind tunnel results and then both processes will be compared with both the suggested wind tunnel corrections and the corrections produced by CFD. Finally, a single step correction between "Step A" and "Step D" will be compared to determine the accuracy of the 3-Step T&I correction process against the "correct" values produced from the CFD simulation of "Step D". This process will analyze both the accuracy of the 3-step process and show that a CFD based correction for the model support system will be nearly as good as performing the process in the wind tunnel.

1.2.4 Blockage and Wall Effects

Traditionally, in the process of the wind tunnel corrections process, the blockage and wall effect corrections are two separate corrections. When running the CFD simulations of the process they end up combined due to how they are applied. The objective of the blockage and wall effect

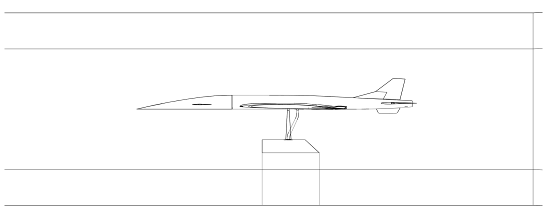

(a) T&I "Step A"

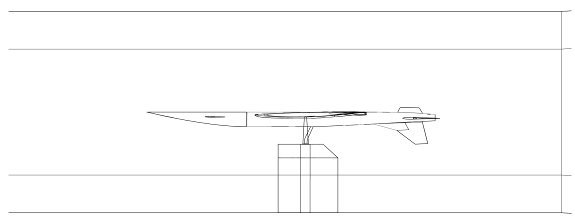

(b) T&I "Step B"

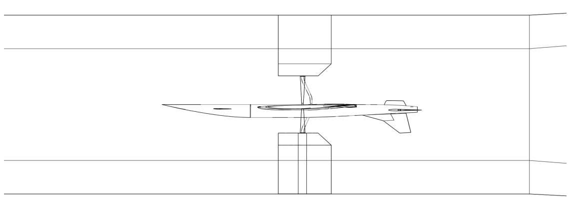

(c) T&I "Step C"

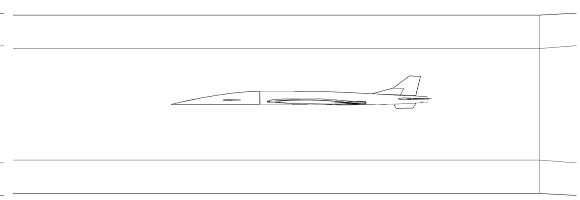

(d) T&I "Step D"

Figure 1.1: The 4 different configurations in the T&I process, with Steps A, B and C being the tested configurations, and Step D being the final "corrected" state of the model with the effects of the support system removed.

corrections is to remove the effects of the walls of the test section from the measured data from the model ("walls" in this sense include the entire perimeter of the test section).

The blockage correction is a correction to the dynamic pressure of the test section due to the measurement of the dynamic pressure of the test section being ahead of the model, and as the model blocks a section of the tunnel , the flow will accelerate around the model (venturi effect), causing the model to see a slightly higher local dynamic pressure than in the tunnel's "free stream" value at the start of the test section. This effect increases with the angle of attack of the model due to more of the cross-sectional area of the test section being blocked by the model itself as well as the displacement effect of the turbulent wake shed down-stream of the model.

The wall effects correction is to adjust for the fact that downwash and side-ward flows generated by the model are distorted by the presence of the tunnel walls rather than just continuing on their free trajectory until the wake dissipates. In subsonic flow, the change to the natural flow-field behavior influences the entire flow-field including that the up-stream in the immediate vicinity of the model. The wall effects correction the is combination of an adjustment on the angle of attack of the model, and an adjustment to the pitching moment of the model due to the wake of the wing and the tail often interacting in ways that would not occur in the freestream. The approximations for these corrections that are typically applied to the measured wind tunnel data were created by Shindo in the 1970's [4]. These semi-empirical mathematical relations rely on a set of wall correction constants that were generated from even earlier work with a set of standard NACA wings [5]. This will be discussed in greater detail later in Chapter 7.

The CFD-based blockage and wall correction is combined due to it being the difference of the "Step D" from the prior T&I section and the free air model, where both the acceleration of the flow around the model and the deflection of the wake of the model are included in a single step. The objectives for this section is to determine whether the wall correction constants used in Shindo's method by the KWT were appropriate and if not, what the new wall correction constants should be.

1.2.5 Objectives of the Thesis

To concisely compile the objectives outlined above, the objective of this thesis is to use CFD to analyze the wind tunnel corrections applied to the SCALOS wind tunnel to determine:

1. The accuracy of the linear 3-step T&I process for a long slender delta wing aircraft model.

2. The accuracy of the standard Shindo's wall and blockage corrections for a long slender delta wing aircraft model.

3. The accuracy of CFD simulations to wind tunnel tests for delta wing aircraft and to compare the results of multiple turbulence models.

This thesis also serves as a compilation and extension of results presented in two conference papers (for which this author was a contributor) presented at the AIAA SciTech conference 2025 and 2026, "Supersonic Configurations at Low Speeds(SCALOS): Correlation of CFD and Wind Tunnel Test Results" [6] and "Wind Tunnel Low-Speed Tare and Interference Corrections: CFD vs Test Results - The Supersonic Configurations (SCALOS) Cases" [7].

Chapter 2

EXPERIMENTAL SETUP

2.1 SCALOS Part Definitions

The SCALOS project (2020-2024) used a wind tunnel model that had been in near continuous use for the Department of Aeronautics and Astronautics since 2013, with the majority of components used dating to 2015 and later. The wind tunnel model was capable of semi-parametric component changes representing a range of potential supersonic cruise conceptual designs. The baseline configuration meant to be a representative 1/22 scale model of a 100 passenger Mach 1.8 transport aircraft. The intent for the baseline design is to be a representative three-surface configuration which was based on results from the Boeing N+2 study [8].

There were over 30 primary interchangeable components at the end of the testing campaign. This thesis will only look at a small subsection of the parts tested. The dimensions of the relevant parts to the configurations tested within are shown in Table 2.1. The general nomenclature for part names is the first letter represents what type of part it is (W for wing, H for horizontal tail, F for fuselage, and N for Nacelle, etc...) and the number following it is either the year the part was first made or which iteration of the part was tested. More specific details about the SCALOS tests and their results can be found here: [1]. Most of the major components are coded by year, with only the sheet metal components being created during the test getting iteration numbers designations. The specifically named configurations in this thesis are labeled as UWS20A and UWS21A, are the “baseline” configurations for the T-tail and low tail configurations, noted that for most of the paper, these configurations were run in CFD without nacelles to match the wind tunnel testing of the T&I process where the nacelles were not used for the bulk of the T&I testing. A detailed overview of the wind tunnel tests can be found [1]. Most of the wind tunnel data from the SCALOS program in this thesis was taken from the SCALOS tests UW2354 and UW2367 performed in 2023 and 2024.

Table 2.1: SCALOS wind tunnel model components specification

	Name	$\Lambda_{LE}(°)$	$\Gamma(°)$	b (ft)	$\bar{c}$ (ft)	$S_{ref}(ft^2)$	t/c_{max}	AR
Canard	C15	50	0	1.22	0.40	0.27	0.04	5.37
Outboard Wing	W15	41.0	4.67	4.67	2.01	8.30	0.05	2.63
	W20	53.5	4.74	4.40	2.10	8.09	0.05	2.39
Horizontal Tail	H20(.T)	49.2	0	1.74	0.59	0.88	0.08	3.43
Vertical Tail	V15	50.1	0	0.74	1.07	0.58	0.05	0.946
	V20	53.3	0	0.777	1.36	0.934	0.05	0.646
Ventral Fin	VF.1	29.9	0	0.17	0.74	0.0033	0.1	0.228
Dorsal Fin	DF.1	73.8	0	0.17	0.75	0.16	0.04	0.181
	Name	d (ft)	l (ft)	$S_{wet,\ ext}$ (ft^2)	S_f (ft^2)	$S_{wet,\ int}$ (ft^2)		
Fuselage	F15	0.54	9.55	10.60	0.22			
Nacelle	N20	0.39	1.95	2.28	0.14	1.71		

2.2 Aircraft Configurations

All CAD geometry of the models were generated from the CAD of the final manufactured parts from AeroTec, where there was an extensive process of cleaning the models for CFD by removing the bolt holes and gaps between the parts. This was a length process due to the need to retain the complex curvature of the parts, while having the CAD software extrapolate the curves. To get water tight parts that STAR-CCM+ considered valid bodies took a significant amount of effort along accurately modeling any sheet metal or tape smoothing that was applied to the model.

2.2.1 W15

The W15 wing shown in an isometric view in Figure 2.1 was the repeatability model used for the SCALOS testing. Every test started with a W15 wing in the test section for inter-test repeatability to see if any changes had occurred from the prior install. It was also one of the 3 configurations tested for T&I testing as a reference for wing alone studies. The W15 wind tunnel model had sets of inboard and outboard leading edge deflections alongside a set of ailerons and trailing edge flaps. CFD of any of these control surface deflections was never studied due to the complexity of generating the cleaned outer model line. The relevant dimensions of the W15 wing are shown in Table 2.1. The 3 defining airfoils of the W15 wing are shown in Figure 2.2 located at the wing root, wing break (the location of the slope change) and the wing tip, with a linear interpolation between them. The wind loft lines were originally generated for use on an RUAV capstone project, with the airfoil thickness increased somewhat and thickness forms modified for model build-ability. As the intent was to focus on configuration general arrangements and planform effects, wing camber and twist were not optimized for supersonic cruise so they are not necessarily representative of an actual supersonic airliner's airfoils.

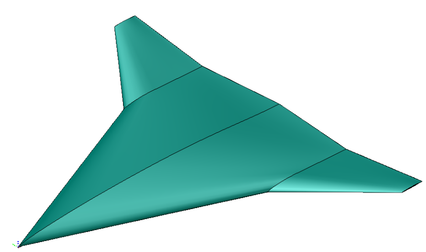

Figure 2.1: Isometric View of the W15 Wing

2.2.2 UWS21A

The UWS21A is the baseline configuration for the SCALOS project. An isometric image of it without nacelles is shown in Figure 2.3. It is the combination of the F15+A15 fuselage/empennage, W15 wing, V15 tail with VF.1 and DF.1 ventral and dorsal fins, the H20.L horizontal stabilator, the C15.F canards and the N20.B nacelles. It is a three-surface model where both canards and the horizontal stabilator can be actuated to control pitch or provide an extra amount of lift. The

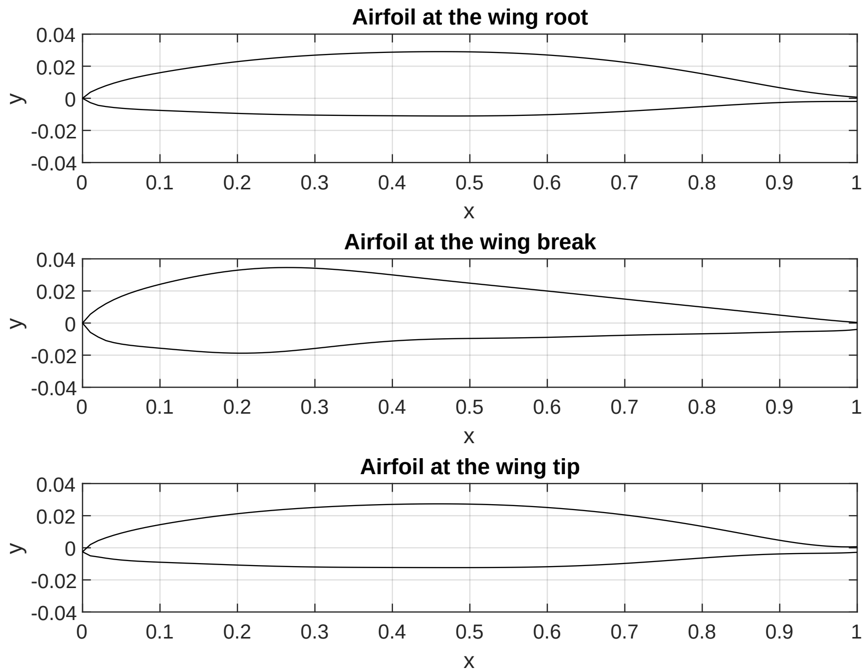

Figure 2.2: Plot of the W15 Airfoils (vertical scale stretched for clarity)

UWS21A configuration had the N20 nacelles mounted underneath the wings, but for the majority of the T&I testing the nacelles were not run, so for the analysis of the T&I process and the Wall corrections the nacelles were not included in the simulations, but the configurations will be still called the UWS21A for convenience. The nacelles were only simulated in the free-air simulations. Selected dimensions of the UWS21A configuration are shown in Figure 2.4

2.2.3 UWS20A

The UWS20A is the reference T-tail configuration for the SCALOS project, where it shares some commonalities with the UWS21A in terms of parts, but it has some key differences. An isometric view of the UWS20A model without nacelles is shown in Figure 2.5. The UWS20A configuration was made up of the F15+A20 Fuselage and Empennage, W20 wing, V20 vertical tail, H20.T vertical tail, C15.F canard and the N20.T nacelles. The H20.T has the same geometry as the H20.L tail

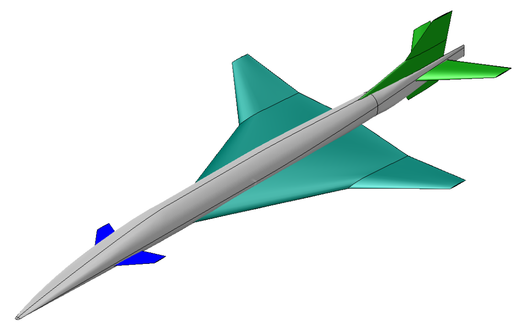

Figure 2.3: Isometric view of the UWS21A model without nacelles

on the UWS21A, just moved up to be a T-tail. The V20 is thickened over the V15 due to the required vertical tail strength for a T-tail. The W20 wing has the same inboard geometry with a slightly higher sweep angle, but otherwise the same leading edge flap and aileron parts, sized for the W20 wing. The N20.T nacelles are the same parts as the N20.B, just with a different set of mounting brackets to mount to the top of the wings rather than the bottom to take advantage of the T-tail configuration. The nacelles were not simulated for the wind tunnel correction process to avoid any potential issues with the simulation. The alternate nacelle and tail arrangement with increased sweep outboard wing panel waas the initial configuration defined for dynamic S&C testing by Boeing Research and Technology in their FVWT facility in Huntington Beach CA. it provided a general arrangement point-of-departure for investigating configuration features proposed to reduce sonic boom and landing/takeoff noise. Specific information on this work can be found in [9], [10], and [11].

2.2.4 Reference Values

For all of the wind tunnel tests completed during the SCALOS test entries, the same reference area, reference lengths and moment centers were used. Additionally nearly all simulations were done at flow velocities representing a dynamic pressure 32 psf or 40 psf to match with existing results

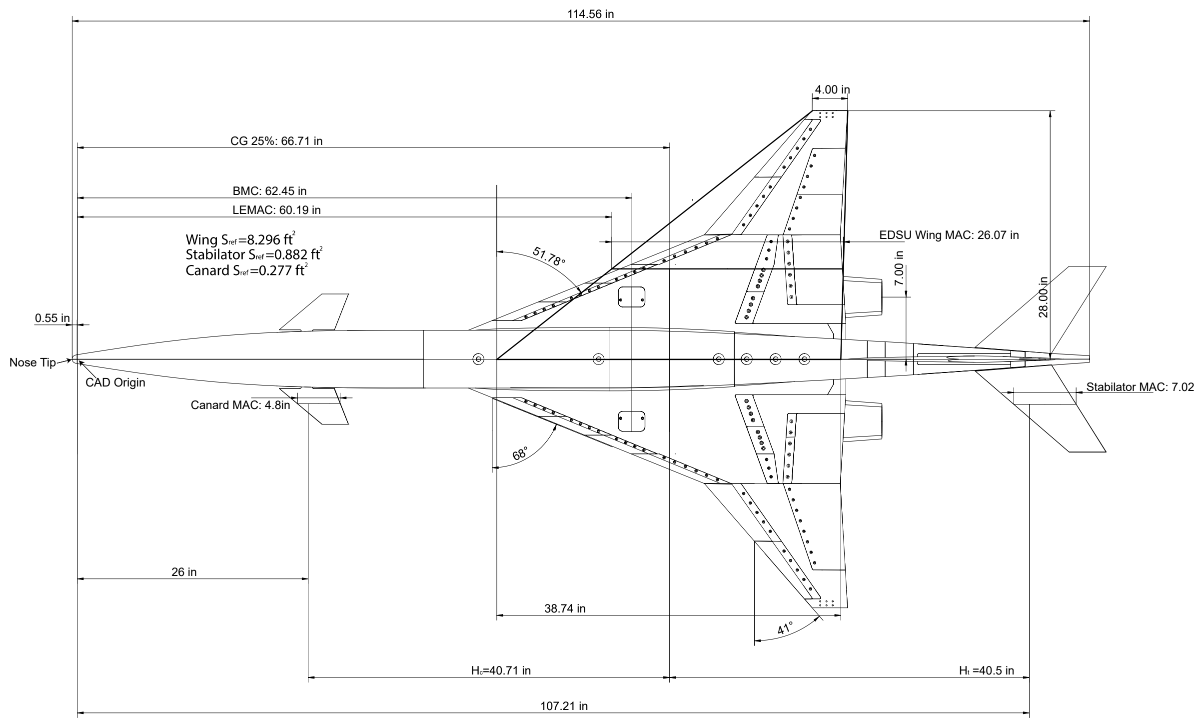

Figure 2.4: Selected dimensions for the UWS21A configuration with moment centers shown

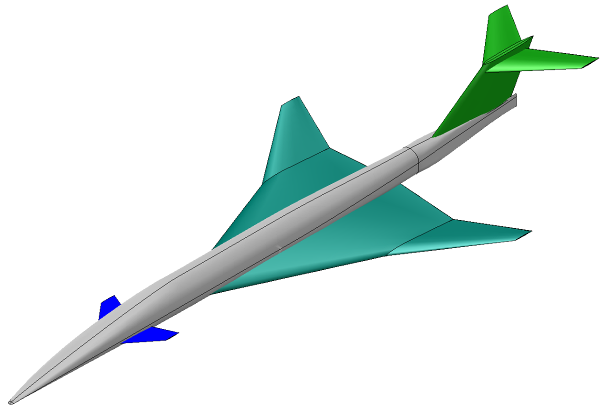

Figure 2.5: Isometric view of the UWS20A model without nacelles

from the tunnel. The T&I work was done at the balance moment center as those corrections are typically applied before the moment transfers to aircraft center of gravity locations, while all free air simulations and wall effects studies were done at the 25% chord reference location CG location as the model moment center for comparisons to the final data.

Table 2.2: CFD Reference Values

Name (units)	Value
S_{ref} (ft^2)	8.296
$\bar{c}_{ref}$ (in)	26.07
b_{ref} (in)	55.93
Balance Moment Center (in)	(62.16,0,0)
Moment Reference (25% $\bar{c}_{ref}$) (in)	(66.71,0,0.55)

2.3 Kirsten Wind Tunnel

All wind tunnel tests were carried out in the Kirsten Wind Tunnel (KWT) at the University of Washington Aerodynamics Labatory (UWAL). The tunnel is a low-speed closed circuit dual-return

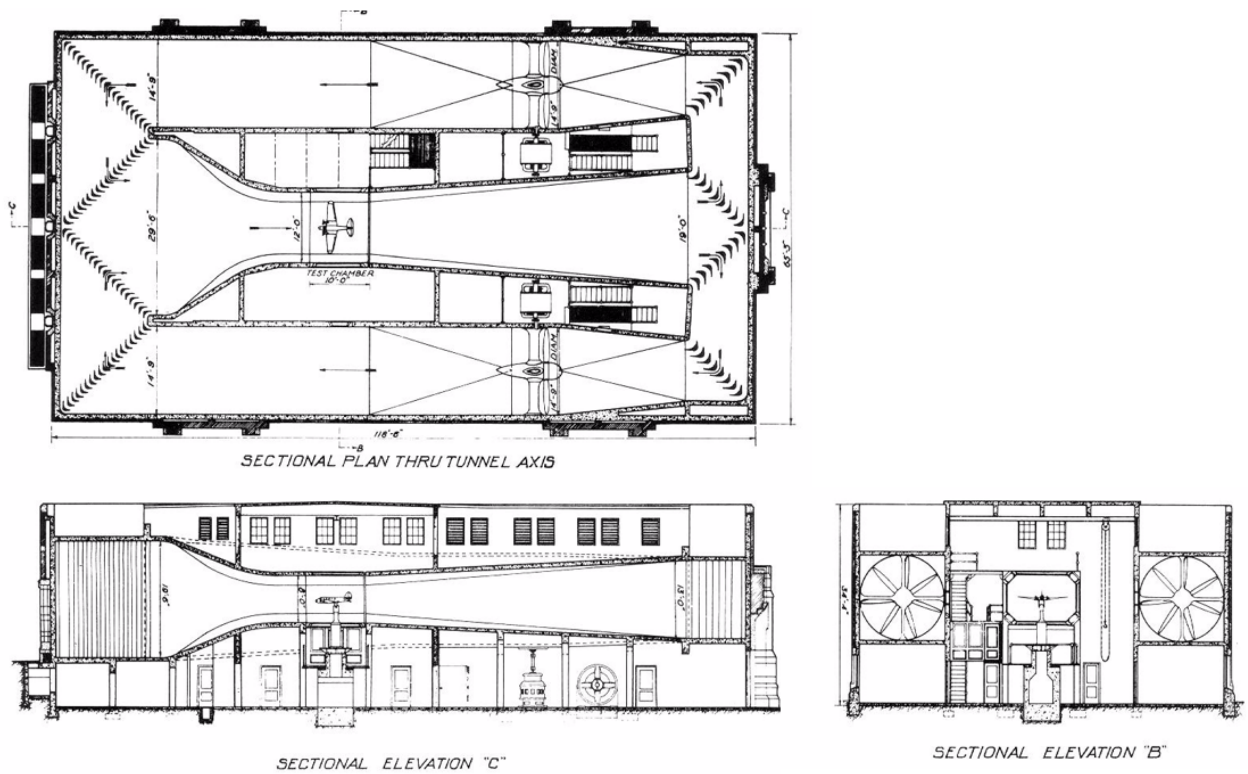

Figure 2.6: A 3-view of the KWT showing the entire circuit, with a model inside the test section.

wind tunnel capable of reaching 200 mph[12]. The tunnel was originally built in 1937 and entered operation in 1939, and has not seen many significant changes to the historical basic circuit or main balance systems since construction. However, over the years multiple generations of improvements to tunnel controls and data systems, and alternative mounting systems have been made, providing increased testing capability and modern data handling. All tests were conducted with the KWT's main external balance mounted below the test section. The balance has the limits of 2500 lbs of lift, 250 lbs of drag and 5000 in-lbs of pitching moment with resolutions of 0.09 lbs, 0.013 lbs, and 0.232 lbs respectively. All data collected in the tunnel is time averaged over 5 seconds after a 5 second settling time at each individual test point (α and β combination) with a 1 Hz low pass filter applied to the data. A three-view of the Kirsten Wind Tunnel is seen in Figure 2.6

The test section of the KWT has a width of 12 ft by a 8 ft height and is 10 ft in long. The edges of the test section have fillets of 1.5 ft in height and length. The diffuser increases to a maximum cross section of 15.8 ft by 12 ft over 47.5 ft distance. The dynamic pressure inside the test section is calculated through a set of static strips at the start of the bell-mouth and the entrance of the test section, which is then corrected by a value derived from a pitot tube. This value is taken to be the dynamic pressure which is then converted to a velocity for the tunnel speed, which is used as the speed of the tunnel in CFD.

2.3.1 Fork and Pylon

The model support system that the T&I method seeks to remove is a combination of a fork/strut and a fairing. For the SCALOS tests the 14H fork with a 7-2 pitch were used where the fork and pitch arm are shown in Figure 2.7a. The fork arms and pitch strut form an inverted tri-pod support for the model. These are components that are "metric" (included in the direct force and moment measurement by the balance). Selected dimensions of the 14H fork are shown in Figure 2.7b The pitch arm is attached to a linear actuator that moves the pitch arm up and down to change the angle of attack of the model. For changing slide-slip angle, the entire fork rotates attached to the inner strut of the balance. Around the circular inner strut a black fairing is placed to remove any aerodynamic forces on the inner strut so only the fork and pitch arm are exposed and to reduce the wake of the fairing to reduce any interference with the model. The fairing is shown in Figure 2.8 with selected dimensions. The fairing itself has a cross-section of a NACA 0018 airfoil. The fork, pitch arm and fairing were used for all SCALOS tests. A custom 3d printed image fork from a 3d scan was used for the "dummy" image supports for T&I testing, and the KWT's standard image fairing was used.

2.4 Specific Flow Conditions

For the data analyzed in this paper, the majority of the results were run at 32 psf. Some of the older data used to get the specific configurations in the configuration build up in the Free Air section was taken from older data run at 40 psf. The lower dynamic pressure was chosen as the standard running condition to avoid over-loading the balance should model dynamics be encountered due to unsteady separated flow at the highest tested angle of attack. For the T&I analysis and Wall and Blockage Corrections, were all run at 32 psf. This results in a Reynolds number of $2.37e6$ for 32 psf and $2.74e6$ for 40 psf. The measured turbulence intensity of the tunnel was around 0.5%[12].

(a) View of the 14H fork and 7-2 pitch arm combined

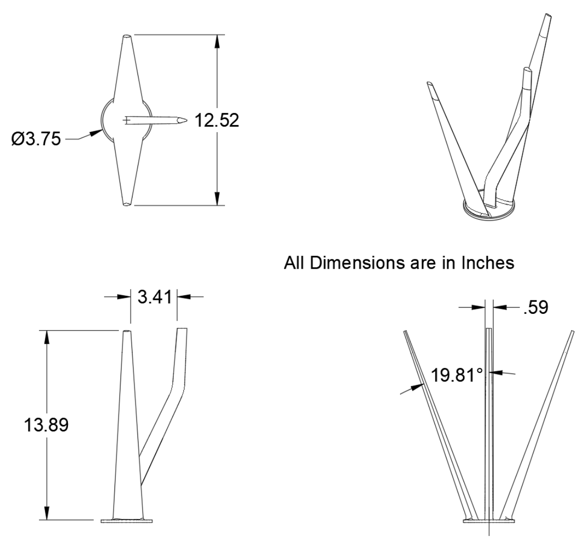

(b) Selected Dimensions of the 14H fork

Figure 2.7: Detail of the fork and pylon and the model in the wind tunnel

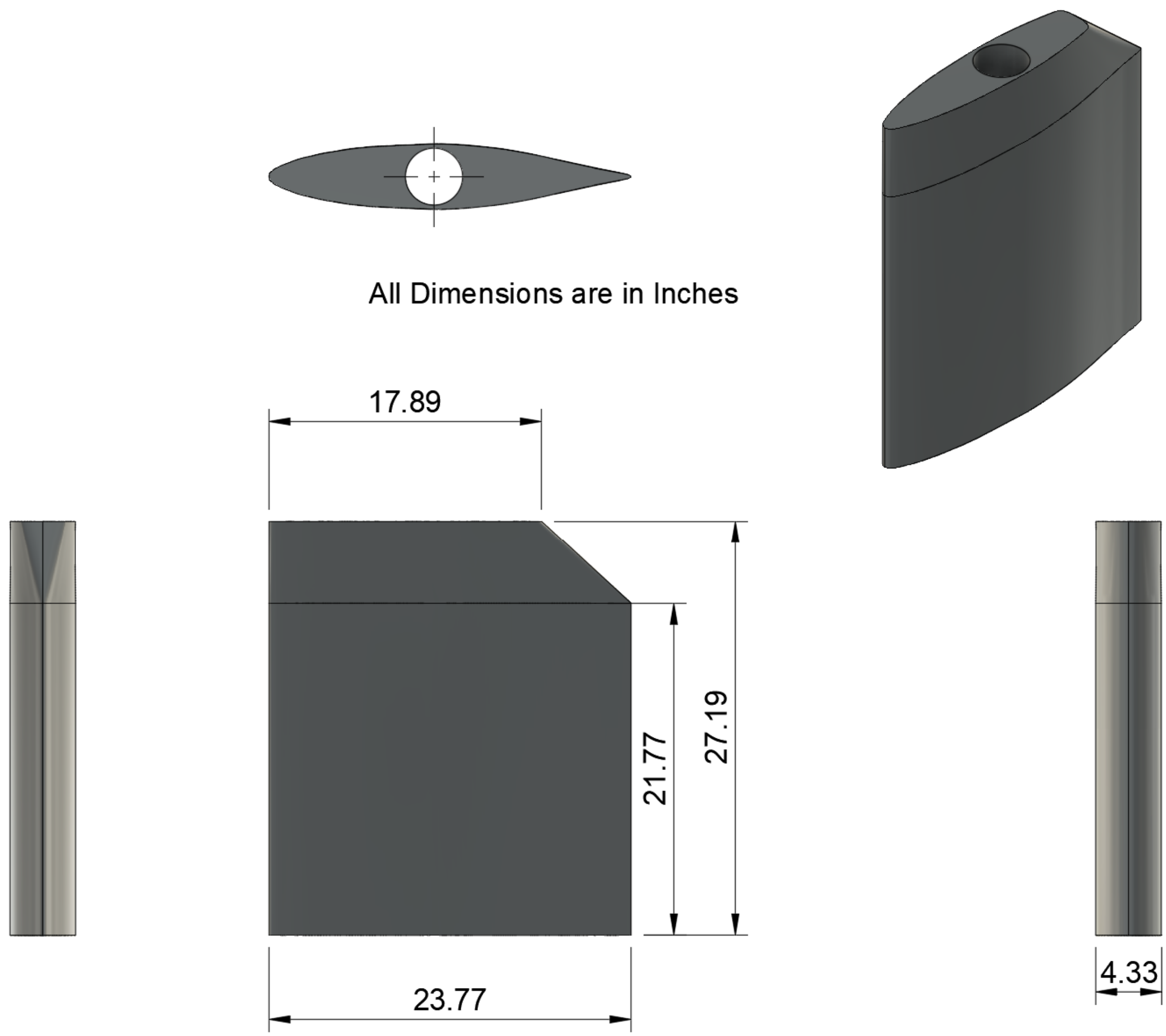

Figure 2.8: Views with dimensions of the fairing with the 4.6 fairing cap.

Chapter 3

COMPUTATIONAL FLUID DYNAMICS

Computational Fluid Dynamics (CFD) has recently become an integral partner with, and sometimes competitor to wind tunnel testing with the rise in computational capabilities reducing the required compute time and increasing the mesh density of simulations. Testing and CFD have complementary capabilities, and systematic choices need to be made over how and when to use both tools effectively. CFD discretizes and simulates a geometry of the fluid of interest, which for this thesis is either the interior of a wind tunnel with a hollow region in the middle for the wind tunnel model with or without support system, or the flow around a model with a spherical far field with a hollow region for the aircraft inside. These fluid domains are then discretized into a mesh with variable cell sizes and shapes depending on the locations in and proximity to surfaces of interest. Then a numerical method solving some variation of the Navier-Stokes equations is implemented on all of those cells to produce the simulated result. However, exactly solving the Navier-Stokes equations is generally unfeasible, so some aspects of the physics are modeled instead. Specifically, the time-averaged behavior of the flow averages over any complex turbulence structures that may be present in the flow, which may be detrimental to simulations of separated or vortex dominated flows. This often leads to CFD having difficulty modeling all fluid regimes and situations with equal accuracy.

3.1 Theory

The Navier Stokes equations represent a total explanation of the behavior of any fluid, shown in Equation 3.1 for continuity or conservation of mass, Equation 3.2 for conservation of momentum and Equation 3.3 for conservation of energy. Noting that all simulations done of the Kirsten Wind Tunnel are done at a velocity less than Mach 0.3, so any compressibility effects are minor and considered negligible where ρ is constant and there is no heat transfer involved, so the energy equation is generally considered unnecessary for most discussions of the physics.

$$\frac{\partial \rho}{\partial t} + \nabla \cdot (\rho \vec{u}) = 0 \tag{3.1}$$

$$\frac{\partial \rho \vec{u}}{\partial t} + \nabla \cdot (\rho \vec{u} \otimes \vec{u}) = -\nabla p + \mu \nabla \cdot \boldsymbol{\tau} \tag{3.2}$$

$$\frac{\partial \rho e}{\partial t} + \nabla \cdot (\rho e \vec{u}) = \rho \dot{Q} + \nabla \cdot (k \nabla T) - \nabla \cdot (\vec{u} P) + \nabla \cdot (u \cdot \tau) + \rho \vec{F} \cdot \vec{v} \tag{3.3}$$

The Navier Stokes equations can be simplified to the following for incompressible flow, for Mach numbers of 0.3, where all studies here represent: the incompressible continuity equation in Equation 3.4 where the density is assumed constant, and the internal energy (temperature) is constant as well. The incompressible momentum equation is shown in Equation 3.5. These will be used going forward for the analysis of the Reynolds Average Naiver Stokes Equations.

$$\nabla \cdot \vec{u} = 0 \tag{3.4}$$

$$\rho \frac{\partial \vec{u}}{\partial t} + \rho \vec{u} \cdot \nabla \vec{u} = -\nabla p + \mu \boldsymbol{\tau} \tag{3.5}$$

There are very few exact solutions to these equations and nearly none for the fully three dimensional formulations of the Navier-Stokes equations. As such several numerical methods have been developed to solve these equations, necessitating the need for numerical methods to solve the Navier Stokes equations.

The general problem with solving and simulating the Navier Stokes equations directly is resolving the effects of turbulence, the chaotic behavior of flows that provide large variations in size of fluctuations. Turbulence is formed of a energy cascade from the largest scale eddies of a flow, which are typically have diameters of the length scale of the model, to the smallest eddy size which has a Reynolds number of 1. Applying a dimensional analysis yields the result that the difference in length scales between the largest and smallest eddies in a single direction scales by $Re^{3/4}$, which becomes $Re^{9/4}$ for a 3d problem. With most aerospace applications for external flows around a body where Reynolds numbers can start at around a 1 million to a few hundred million, the required size of the computation domain grows to be nearly unfeasible to simulation. Additionally with most numerical methods with such large grid sizes limited to direct solvers, the time steps of the problem are typically limited to being roughly on the scale of grid size divided by the greatest speed in the problem (typically the speed of sound if fully compressible) which also means that to fully resolve a solution over a meaningful time scale, the direct numerical implementation of Navier Stokes is unfeasible due to the size of computational grid and amount of time steps required to resolve it.

3.1.1 CFD types

There are multiple different variations of CFD solvers ranging from completely solving the Navier Stokes equations to solving the potential flow equations. These have a variety of different computational complexities and accuracy. In order of computational cost and accuracy the different variations of CFD codes are as follows:

1. DNS: Direct Numerical Solvers, where the Navier Stokes equations are completely solved, but require a grid resolution of the Kolmogorov scale with unfavorable time stepping discussed above. These simulations are generally limited to Reynolds numbers of around 30,000 currently for simple 2d cases [13]. Noting that for the simple NACA 0018 airfoil it took on the order of 10^2 compute hours per angle of attack, rendering DNS still being computationally unfeasible for most exterior aircraft simulations due to the required costs.

2. LES: Large Eddy Simulation, where a filter is applied to the size of eddies in the simulation, where the largest eddies that are believed to drive the flow are simulated, but any below the cut-off point are modeled instead. This helps drive down the required grid size away from the walls of the model, but still retain some of the unsteady vortex dynamics that drive the simulation.

3. DES: Detached Eddy Simulation, which is a hybrid of DNS and RANS, where flows far away from the walls are modeled with an unsteady time stepping model, and wall bounded flows; boundary layers primarily have their dynamics modeled.

4. RANS: Reynolds Averaged Navier Stokes, is the most commonly used variant of CFD in industry due to it lacking significant Reynolds number limitations. RANS solves the Reynolds averaged Navier Stokes equations, where the resulting quantities produced are the averaged quantities of the flow field, where any unsteady turbulent effects are modeled instead. Modeling turbulence is often imprecise and where there are flows that are dominated by turbulent behavior or deviates from a normal boundary layer construction is where RANS solvers have difficulty fully resolving the vortex structure.

5. Euler Methods: Euler methods remove viscous effects entirely and are completely inviscid solvers. Specifically the remove the no-slip condition from the walls of the tunnel so that the flow is tangent to the surface of the wall on the wall. Pressure driven flows can still be analyzed, but any flows with significant turbulent effects are removed. Euler codes however require lighter weight meshes that don't require the prism layers generated on wall that the above codes require. Euler solvers being inviscid do not model boundary layer separation and are unsuited for high angle of attack simulation. However, Euler methods often have an added numerical viscosity effect to increase solver stability. These effects can match the effects of viscosity in the flow, so leading edge vortices can be simulated with appropriate tuning to example data. However, this typically only works for sharp leading edges.

6. Potential Flow: Potential flow solvers are limited to incompressible inviscid flow solvers that are generally unable to take external pressure gradients as well due to them solving Laplace's equation which comes out of the conditions of incompressible and irrotational flows. While standard meshes can be used to solve these methods, oftentimes they're more commonly used with lighter-weight systems that use potential flow theory of horse shoe vortices on a lattice that represents the geometry of the aircraft, which is then solved to get the velocity tangent to the aerodynamic surface. Potential flow solvers do not model stall due to their lack of viscous effects and are generally only useful for small angle of attacks and initial design methods.

Each of the methods have different uses for different situations and at different places in the design cycle. Potential flow codes have seem popular used in optimization schemes where simulation speed is a priority, where LES simulations are often used to verify specific behaviors of mature designs. For the problems analyzed in this thesis, RANS was selected to be the CFD method of choice as it provides all of the required physics for the problem without incurring a significant computational cost. Additionally as the wind tunnel data was collected and time averaged, in theory the time averaging effects of RANS should average out the spatial effects.

3.1.2 Overall RANS Equations

The Reynolds average Navier Stokes equations are derived from applying the Reynolds decomposition into the Navier Stokes equations and then averaging the equation. The Reynolds decomposition states that any fluid quantity can be decomposed into two components, the average value and a fluctuating instantaneous component which has an average of 0. This is represented mathematically as the following: $u = \bar{u} + u'$, where u is the velocity of the flow at a given point and time, $\bar{u}$ which is the average value of the flow's behavior at that point in space over time, and u' is generally treated as a quantity that is very similar to a random variable (the Navier Stokes equations are chaotic, not random, but for experimental purposes describing u' as a random variable works well and can offer significant insight to the dynamics of the flow). Applying this decomposition to the momentum equation results in the following equation for momentum in Equation 3.6. While most of the terms in the RANS momentum equation matches with the normal momentum equation, there is the addition of an extra term being the dyad of the u' vectors. This tensor is often called the Reynolds stress tensor and is the term that is approximated by turbulence models. It is typically combined with the viscous stress tensor $\bar{\boldsymbol{\tau}}$ due to similar shape and behavior.

$$\frac{\partial \bar{u}}{\partial t} + \nabla \cdot (\bar{u} \otimes \bar{u}) = -\frac{\nabla \bar{p}}{\rho} + \nu \nabla \cdot \bar{\boldsymbol{\tau}} - \nabla \cdot \overline{(u' \otimes u')} \tag{3.6}$$

3.1.3 Turbulence Models

Generally, RANS is known to struggle with post-stall conditions and where there are regions of high flow separation or flows that are dominated by large vortex behavior with significant unsteady behavior. There a multitude of different turbulence models in existence for a large variety of flows. For incompressible viscous flows around external aircraft geometry there are two typically recommended turbulence models that are especially well tuned for wall flows, the Spalart-Allmaras (SA) turbulence model and the 2003 Menter Shear Stress Turbulence (SST) model are typically the standard recommendations for flow around external models.

Spalart Allmaras (SA)

The Spalart Allmaras one equation turbulence model was developed in 1992 by P. Spalart and S. R. Allmaras while working for Boeing [14]. The SA turbulence model works by defining the Reynolds stress tensor in Equation 3.7 and introducing a new turbulent viscosity ν_t which describes the increased momentum diffusion from the turbulent behavior.

$$-\overline{u_i'u_j'} = 2\nu_t(\frac{\partial \bar{u}_i}{\partial x_j} + \frac{\partial \bar{u}_j}{\partial x_i}) \tag{3.7}$$

The addition of an extra variable ν_t is treated as a conserved quantity where it's evolution with time is described in Equation 3.8 generically where the equations and constants contained change within to a $\widetilde{\nu}$ and a $\widetilde{S}$ for values within the buffer and viscous sub-layer of the boundary layer, while the main equation shown below is for the main log layer. The rest of the values are constants or specific shape functions that act to model the behavior of a boundary layer.

$$\frac{\partial \nu_t}{\partial t} + \vec{u} \cdot \nabla \nu_t = c_{b1} S \nu_t + \frac{1}{\sigma}[\nabla \cdot (\nu_t \nabla \nu_t) + c_{b2}(\nabla \nu_t)^2] - c_{w1} f_w \left[\frac{\nu_t}{d}\right]^2 \tag{3.8}$$

Other terms can be added to the SA turbulence model to improve it in certain settings slightly. However for this discussion the baseline configuration of the Spalart-Allmaras turbulence model will be used. The other primary detail for the SA turbulence model is that it is recommended to have the first cell height of the boundary layer to be less than a y^+ value of 1. The quantity y^+ is a non-dimensional way of measuring the thickness of a boundary layer consistent between all boundary layers. It is further discussed in the next section.

Menter Shear Stress Turbulence (SST)

The Menter Shear Stress Turbulence Model (SST) used in this thesis was the version published in 2003 by Menter, Kuntz and Langtry [15]. The model itself is a two equation model uses the conservation of two different quantities, k, the turbulent kinetic energy and swaps between ϵ and ω, the turbulent dissipation and average turbulent frequency depending on distance from a wall. The turbulent viscosity can be retrieved from turbulent kinetic energy and turbulence frequency by Equation 3.9 and turbulent kinetic energy and turbulent dissipation by Equation 3.10 [2].

$$\nu_t = \frac{k}{\omega} \tag{3.9}$$

$$\nu_t = \frac{k^2}{\epsilon} \tag{3.10}$$

The model was originally developed due to observations that the $k - \omega$ model worked very well for boundary layer flows and low Reynolds number flows, but did not perform as well for free-stream conditions and the $k-\epsilon$ model did very well for free-shear flows but generally failed in regions of adverse pressure gradients and boundary layers. With both models performing well where the other one did not, they were combined together where flows close to the wall used the $k-\omega$ model and the freestream flow used the $k-\epsilon$ model[2]. To transition between the two models, a hyperbolic tangent function is used as a blending function. The k PDE used is shown in Equation 3.11 and the ω pde is listed in Equation 3.12, and the blending function is shown in Equation 3.13 with the CD_{kw} in Equation 3.14. Additional definition of constants and limiters can be found in [15] for additional details.

$$\frac{\partial \rho k}{\partial t} + \nabla \cdot (\rho U k) = \widetilde{P_k} - \beta^* \rho k \omega + \nabla \cdot [(\mu + \sigma_k \mu_t) \nabla k] \tag{3.11}$$

$$\frac{\partial \rho \omega}{\partial t} + \nabla \cdot (\rho U \omega) = \alpha \rho S^2 - \beta \rho \omega^2 + \nabla \cdot [(\nu + \sigma_\omega \mu_t) \nabla \omega] + 2(1 - F_1) \rho \omega_{w2} \frac{1}{\omega} (\nabla k \cdot \nabla \omega) \tag{3.12}$$

$$F_1 = \tanh \left[\left[\min \left[\max \left(\frac{\sqrt{k}}{\beta^* \omega y}, \frac{500 v}{y^2 \omega} \right), \frac{4 \rho \sigma_{w2} k}{CD_{kw} y^2} \right] \right]^4 \right] \tag{3.13}$$

$$CD_{kw} = \max \left(2 \rho \sigma_{w2} \frac{1}{\omega} \nabla k \cdot \nabla \omega, 10^{-10} \right) \tag{3.14}$$

Notably for the SST turbulence model, the first height of the prism layer cells are less sensitive than the SA turbulence model where a combination of the wall functions, a mixed more and a low Reynolds number model all produced similar results, where typically it's recommended that the first layer needs to be inside of the linear region of the boundary layer if the full simulation of the boundary layer is necessary. This does provide a slight advantage for the SST turbulence model over the SA turbulence model in that regard, especially when complex geometries may cause distortions in the prism layers generated around the model.

3.1.4 Meshing Specific Calculations

To successfully running a CFD simulation to produce as accurate of results as possible, there are several aerodynamic and fluid quantities required to be generated for the mesh. Basic reference quantities, such as the desired fluid speed and reference lengths are required, alongside the density and kinematic viscosity of the fluid. Additionally the Reynolds number is necessary for many different quantities with the equation shown in Equation 3.15 where u is the free-stream velocity and l is the reference length, so that Re_l is the Reynolds number for that reference length.

$$Re_l = \frac{ul}{\nu} \tag{3.15}$$

For meshes, the general parameters when defining a mesh were the target and minimum surface sizes in the free-stream and the target and surface sizes on any surface with walls, and especially any surface that force and moment measurements were to be made on it. To better capture some of the behavior of the wake of the model, a wake refinement region was generated that was typically around 10 times the reference length of the model (10 m for the simulations done here for the wind tunnel model) with an expansion angle double the maximum angle of attack of the model.

To properly model the boundary layer of the model, two different values need to be determined, an approximation of the total thickness of a boundary layer, and the desired y^+ first cell thickness. For the total thickness of the boundary the turbulent flat plate boundary layer equation was used shown in Equation 3.16 which uses x, the length of the object of study and the Reynolds number using that length [16].

$$\delta_t = 0.37xRe_x^{-1/5} \tag{3.16}$$

To determine the value of $y^+ = 1$ for a simulation, the following process needs to be followed. First determine the Reynolds number of the flow from Equation 3.15. Then a skin friction coefficient needs to be determined for the corresponding flow. The typically suggested one the 1/5 power law shown in Equation 3.17, however results will not change significantly if different skin frictions are used.

$$C_f = 0.0592Re^{-1/5} \tag{3.17}$$

This skin friction coefficient can be turned into a wall shear stress, τ_w as shown in Equation 3.18.

$$\tau_w = 0.5\rho u^2 C_f \tag{3.18}$$

The non-dimensionalized velocity of the boundary layer u^+ can then be determined by Equation 3.19.

$$u^+ = \sqrt{\frac{\tau_w}{\rho}} \tag{3.19}$$

The value of y for a $y^+ = 1$ then can be found using a modified Reynolds number calculation, which relates the actual thickness of y to the non-dimensional y^+ shown in Equation 3.20.

$$y_{first} = \frac{y^+ \nu}{u} \tag{3.20}$$

This value can then be inserted into the CFD mesher as the first prism layer height. The total thickness of the prism layer can be set by a small multiple of the boundary layer thickness (2 or 3 times). Boundary layer prism layers typically grow exponentially to avoid requiring a massive amount of them, with a recommended growth rate r of 1.3-1.5 from STAR-CCM+ [2]. To accomplish this, a geometric series was used with the following Equation 3.21. This ended up being around 25 prism layers for most simulations.

$$n = \log_r(1 - \frac{\delta(1-r)}{y_{first}}) \tag{3.21}$$

3.2 STAR-CCM+ Specifics

STAR-CCM+ was selected for its ability to streamline the CFD workflow with containing an integrated mesh and flow solver, and it's integration into the University of Washington's supercomputer Hyak. The general STAR-CCM+ setup was using the coupled energy equation for additional solver rigidity, steady flow solver, with the real gas's equilibrium air model, with the RANS solver and the turbulence models set to SA or SST with their default settings. For the simulations of the wind tunnel model in free air, a spherical computational domain was used that had a radius of 25 times the mean aerodynamic chord of the model. This radius was typically found to allow for the flow around the model to be fully simulated without any prominent flow features exiting the boundaries of the computational domain. In STAR-CCM+ the spherical far-field was set as the freestream condition where a mach number was set, calculated from the standard temperature in the wind tunnel during the UW2354 and UW2367 tests (288 K). The model had it's surfaces set to no-slip walls. For the free-stream model only a single mesh was generated and then the direction of flow entering the simulation was changed for each angle of attack and side-slip angle. Forces and moments were summed over all surfaces of the model. As this left the forces and moments of the model in the body reference frame, the forces and moments needed to be rotated to the wind reference frame using the standard rotation matrix. The freestream models had 25 prism layers and an initial

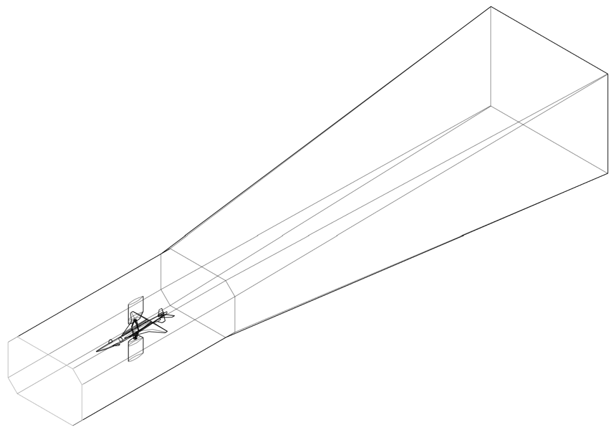

Figure 3.1: Example geometry of a model inside the simulated test section geometry

layer height of 6e-6 m. Simulations were run initially for 1000 iterations, which generally resulted in residuals for condition, momentum and energy all dropping to 1e-8 of their initial values. Later a check on the pitching moment for asymptomatic was applied with a deviation of 0.1% normal change over 30 iterations. This reduced the required iterations to a range of only 300 iterations, with the main continuity, momentum and energy residuals still reaching their standard 1e-8 value. The general setup of the in tunnel simulations had the KWT test section and diffuser model as the computation domain for the tested configurations, with only a 5 ft section of uniform on-set flow added to the start of the test section to assist in convergence. The geometry shown in Fig. 3.1 shows the full computation domain of the KWT's test section and diffuser with the T&I Step C as the model. The walls of the tunnel are labeled as no-slip inviscid walls to reduce cell count with the assumption that the boundary layers of the walls will not impact the solution of the problem significantly. The wind tunnel model, fork and pylon (including the image fork and pylon) had 25 prism layers generated with a first layer height of 6e-6 m, targeting matching the $y^+ < 1$ for flow regime. All mesh settings will be kept the same between simulations of the different cases in order to keep a consistent accuracy of the simulations and to enable direct comparison. Simulations were run for 1000 iterations, which generally yielded residual drops of 4 orders of magnitude for x, y, and z momentum, and residual variation of 10^{-3} for forces and moments.

Forces and moments are calculated by integrating the pressure distributions over the model of the plane and the fork. For the "Step C" of the T&I correction method, the image fork is included in the force calculations as well. The pylon is not included due to it not being attached to the KWT's balance and is not a metric surface to the balance. For "Step A", the forces on the wind tunnel model alone were also generated as an answer to what the model would experience with the fork impinging on the flow field of the model.

Chapter 4
MESH DENSITY STUDIES

Mesh density studies are an important element in supporting the accuracy of CFD simulations to prove that the results of simulations do not vary significantly with mesh density or that better or worse simulations may be achieved with greater or less mesh density. To properly verify the behavior of the variety of simulations performed, four different mesh density studies were performed with the W15 wing and the UWS21A in the two different fluid regimes tested in the paper, in free air and inside the test section. Each mesh size received about 3-4 different sizes and were compared against the wind tunnel results to check for any expected difficulties that CFD would have in producing accurate results. Typically these deviations from wind tunnel results occur where there are large regions of flow separation at AOA's above 10°. This is often best seen in the variation in the pitching moment results varying greatly with the trends being far less consistent than the lower angles of attack, where most of the mesh density studies generally agree on the slope and pitching moment at a condition of zero lift.

4.1 Free Air

All of the free air simulations were done with spherical boundaries with diameters 50x the reference length of the model [2]. These far-fields are considered to be far enough away from the disturbed flow from the model to not noticeably change the flow fields as if the model was in the atmosphere alone. A turbulence intensity of 1% was used for both the Free Air and the in tunnel simulations to improve correlations between them for later studies, however testing with other turbulence intensity values did not yield significant differences. This way, the laminar to turbulent transition points and the flow separation points should be similar. Most of the initial mesh size built upon the prior work of Nicolas Mavriplis from his master's thesis [17] where he analyzed the W15 wing on it's own prior. The wind tunnel data that the CFD results are being compared to and for the later Free Air comparisons, is the fully corrected wind tunnel data produced from the SCALOS study.

These wind tunnel results were corrected with the T&I results that were experimentally generated, Shindo's corrections for blockage and wall corrections, an interior nacelle correction that removed the drag from the interior of the nacelles (being non-physical), and a laminar flow correction for low angles of attack on the model. For later results with nacelles, the interior of the nacelles were not included in the surfaces who's pressure distribution were integrated to generate the forces and moments. With these corrections applied, there is some natural disagreement between the CFD and wind tunnel results due to the different processes applied to the wind tunnel results.

4.1.1 W15

For the W15 in free air, the mesh density studies were done for both the SA and SST turbulence models to see the differences in behavior between the two models. The same meshes were used between the two different turbulence models as the conditions for the prism layers for the SA turbulence model fit the same range of requirements for the SST turbulence model. There were three different mesh sizes tested for the W15, a Coarse, Medium, and "Standard" size mesh, with each being defined by halving the target and minimum mesh sizes of the previous iterations. Additionally the wake isotrope size was halved as well. The extensive meshing settings are detailed in in Table 4.1. Prism layer settings were maintained between the different meshes to follow the best recommended practiced.

Table 4.1: Driving Mesh Parameters for the Free Air W15 Mesh Study

Mesh Parameter	Coarse	Medium	Standard
Target Size (m)	0.04	0.02	0.01
Minimum Size (m)	0.0004	0.0002	0.0001
Surface Growth Rate	1.3	1.3	1.3
Number of Prism layers	25	25	25
Total Height of prism layers (m)	0.025	0.027	0.027
Wake Isotropic Size (m)	0.4	0.2	0.1
Wake Length (m)	10	10	10
Spread Angle (deg)	40	40	40
Volume Growth Rate	1.2	1.2	1.2
Total Number of Volume Cells	811407	1800816	6611951

The results of the mesh density studies are shown in Figure 4.1 and Figure 4.2. Both produce similar results between the two difference turbulence models, so for the future cases, one turbulence model was chosen over the other for the mesh density study. For the actual results presented later, both turbulence models will be compared for the simulation results shown in later chapters. For the lower angles of attack ($-10° < \alpha < 10°$) all the mesh densities produce similar results, even with the C_{D0} not following a distinct trend. Once higher angles of attack are reached, some trends start to appear when compared with the wind tunnel results. For both turbulence models, each shows lower lift produced than what the wind tunnel results show. This leads to an under prediction in drag due to the lower lift causing lower induced drag. However, the SA turbulence model better matches the C_L vs C_D plot the general curvature being matched, with a slightly lower curvature at middle range of the sideways parabola. For both turbulence models, the pitch break point (the point where the linear region of the C_M curve flattens and starts to reverse) for the simulations is extended to around 10° while the wind tunnel has the break point at 7°. This may be due to a mismatch in the separation points for the simulation in comparison to the wind tunnel. The pitching moment curve's curvature is best represented in both cases with the standard mesh. The SA model performs a bit better at this than the SST model does. Either way, this region of large flow separation at high angles of attack is where the mesh density simulations were mismatched suggesting where the turbulence models have difficulties in resolving the behavior consistently.

4.1.2 UWS21A

A mesh density study was performed on the UWS21A in the Free Air without nacelles to assess the effects of mesh size, surface growth rate, prism layer size, and wake conditions. The four different mesh sizes are shown below in Table 4.2, with the sizing and nomenclature mostly taken from the previous mesh density study performed by Marviplis in 2023 [17].

Based on the results from the study shown in Figure 4.3, sizes between standard and fine seem to generate the best results, with the typical target size of 40-50 million cells. Wake isotope sizes were dropped further to 0.07. However, the general mesh sizes were set to a wall target size of 0.01 m and a minimum size of 0.0001 m with a surface growth rate of 1.1 with a greater spread and finer wake refinement region as shown with the closer results shown below. With the increased

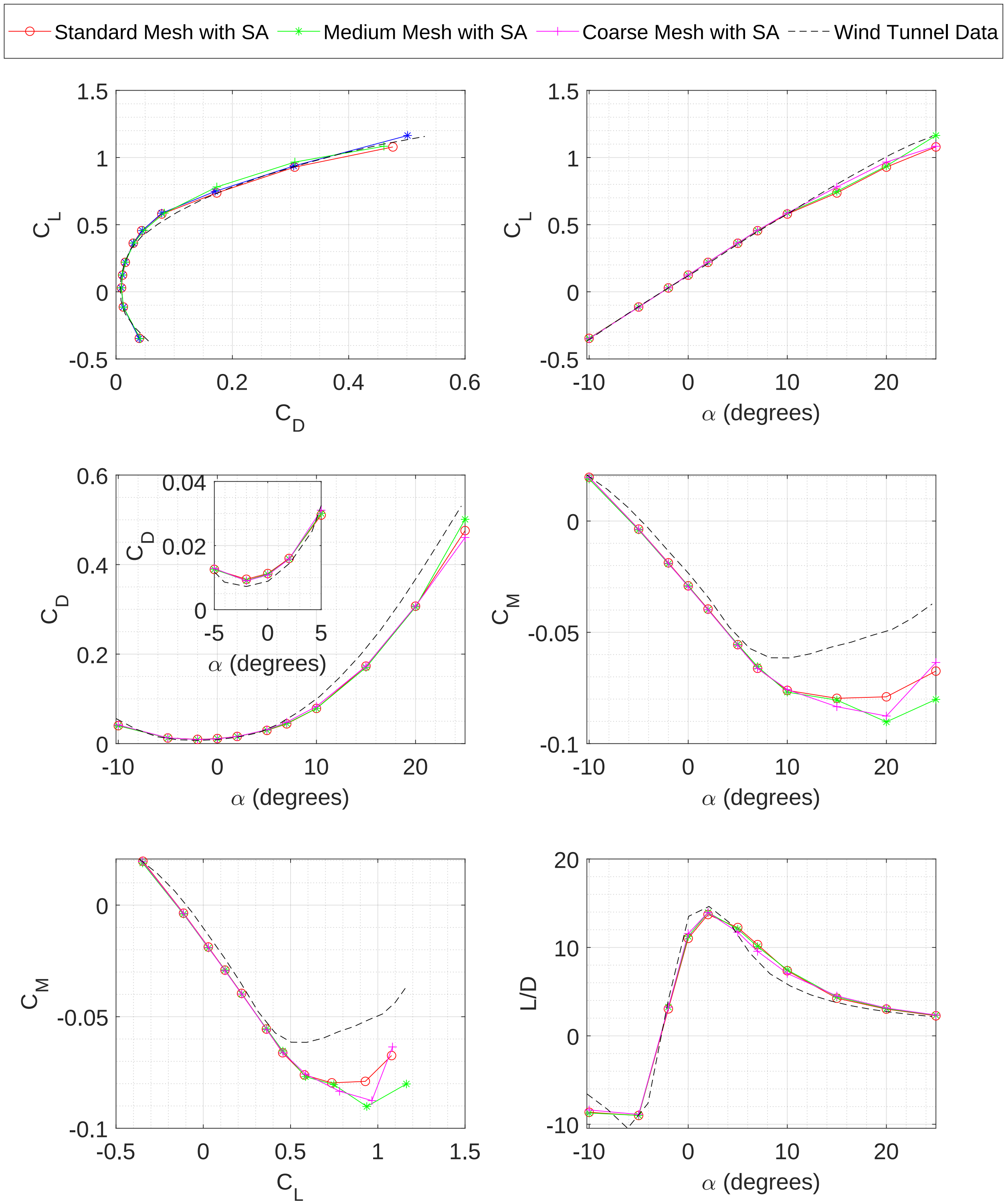

Figure 4.1: Mesh Density Study for the W15 Wing in Free Air with the SA turbulence model

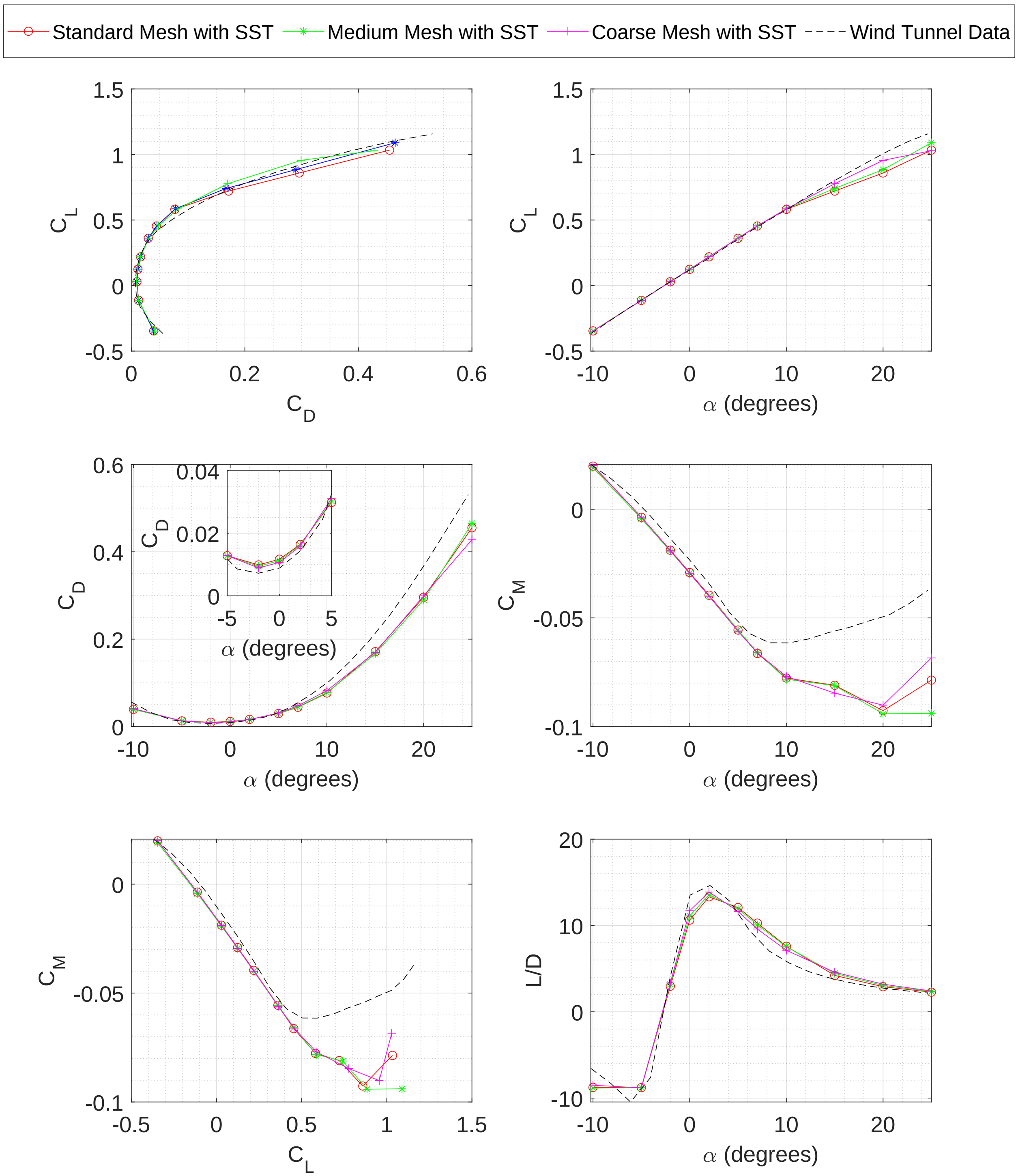

Figure 4.2: Mesh Density Study for the W15 Wing in Free Air with the SST turbulence model

Table 4.2: Driving Mesh Parameter for the UWS21A mesh density study

Run	Coarse	Medium	Standard	Fine
Target Size (m)	0.05	0.025	0.01	0.005
Minimum Size (m)	0.0005	0.00025	0.0001	0.00005
Surface Growth Rate	1.3	1.2	1.1	1.05
Number of Prism layers	20	25	25	35
Total Height of prism layers (m)	0.025	0.027	0.027	0.03
Wake Isotropic Size (m)	0.5	0.25	0.1	0.1
Wake Length (m)	10	10	10	10
Spread Angle (deg)	40	40	40	40
Volume Growth Rate	1.2	1.2	1.2	1.2
Total Number of Volume Cells	3851394	13908777	53282101	68580542

expansion fan size this typically yielded mesh sizes around 30-40 million cells for non-symmetric full configuration cases. Runs with nacelles had slightly higher mesh densities on the interior of the walls and additional wake refinements behind them.

The mesh density study shows trends that were found in the later comparisons for other configurations. CFD Lift and drag can match tests quite well with an offset in C_{D0}. Higher cell counts lead to a closer drag analysis/test match. The medium refinement leads to an acceptable enough analysis/test match for the lift curve. The large analysis/test offset in C_{M0} and the vertical translation of the curve was found in the cases where the H20.L tail was used. In an engineering approach, this could be reduced later by an adjustment in tail angle. The analysis captures the moment versus AOA and versus CL trends well. The offset may be caused by the downwash from the wing not being properly captured with the meshes used, although it is not surprising to have more difficulty in capturing pitching moments by CFD due to the very slender nature of the SCALOS configurations where small differences in force distributions on the nose and tail are magnified by the large moment arms involved. Note the relatively good analysis/test correlation for the lift and the drag polar shape. The C_{D0} mismatch affects the quality of the L/D match, of course.

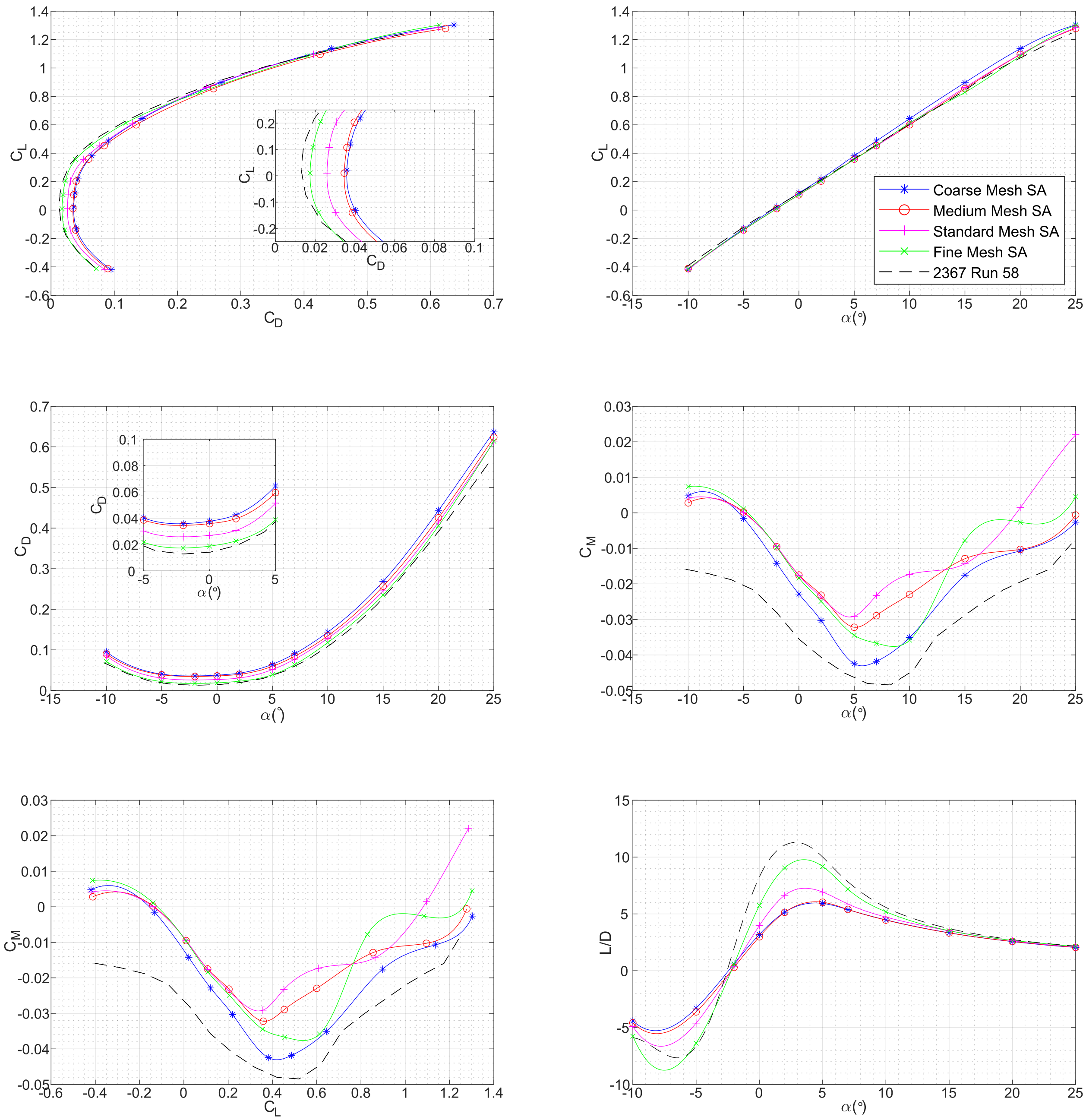

Figure 4.3: Mesh Density study for the UWS21A configuration with the 4 different mesh sizes

4.2 Test Section Replication

A separate set of mesh density studies were run for the in tunnel results where the flow conditions were different than the free air case, with both the tunnel walls and the fork and fairing pylon included in the simulations. The walls of the test section and the fairing were run as slip walls due to model not reaching close enough to the walls to intrude on the boundary layer of the test section, and at the time these simulations were run, detailed information on the KWT boundary layers was not present.

4.2.1 W15

Using the simulation settings for the free-air case that had generated good results were used to set the target surface sizes of the wind tunnel model to 0.01 m and the minimum surface size to 0.0001 m. These surface cell sizes produce a sufficiently dense mesh that matches the wind tunnel results that produces reasonable solution times. For the W15 wing, these settings produce smaller meshes, but still produce results that correlate well to wind tunnel results. To ensure the simulation results are not dependent on the mesh parameters, the surface mesh sizes were halved three times to get the mesh sizes of half, quarter, and eighth meshes, where the surface sizes and wake isotope size were double from each configuration, producing mesh sizes that were about half of the previous simulation. The specific cell counts and surface parameters for each mesh are detailed in Table 4.3. The SST turbulence model was used for the mesh density simulation for the W15 wing.

Name	Model Target Size (m)	Model Minimum Size (m)	Average Cell Count
Eighth	0.08	0.0008	1,689,967
Quarter	0.04	0.0004	4,058,295
Half	0.02	0.0002	9,212,085
Standard	0.01	0.0001	17,638,575

Table 4.3: Cell Counts and other parameters for each of 4 different Mesh Sizes for the W15 Simulations

The 4 simulation results plotted against the wind tunnel results are shown in Figure 4.4 with the SST turbulence model. For angles of attack from $-10°$ to $10°$ all four meshes behave similarly, with the greatest variation being in the zero lift drag of the model. At $15°$ of attack the eighth mesh had a significant over-prediction in lift, which is the lowest cell count mesh. And at high angles of attack there is inconsistency across all four meshes for pitching moment, which is also where the largest deviations from the wind tunnel results occur. This also indicates that the pitching moment results at higher angle of attack is less predictable through RANS CFD simualtions. The lift and drag the simulations are consistent across all angles of attack, with pitching moment at high angles of attack being less consistent.

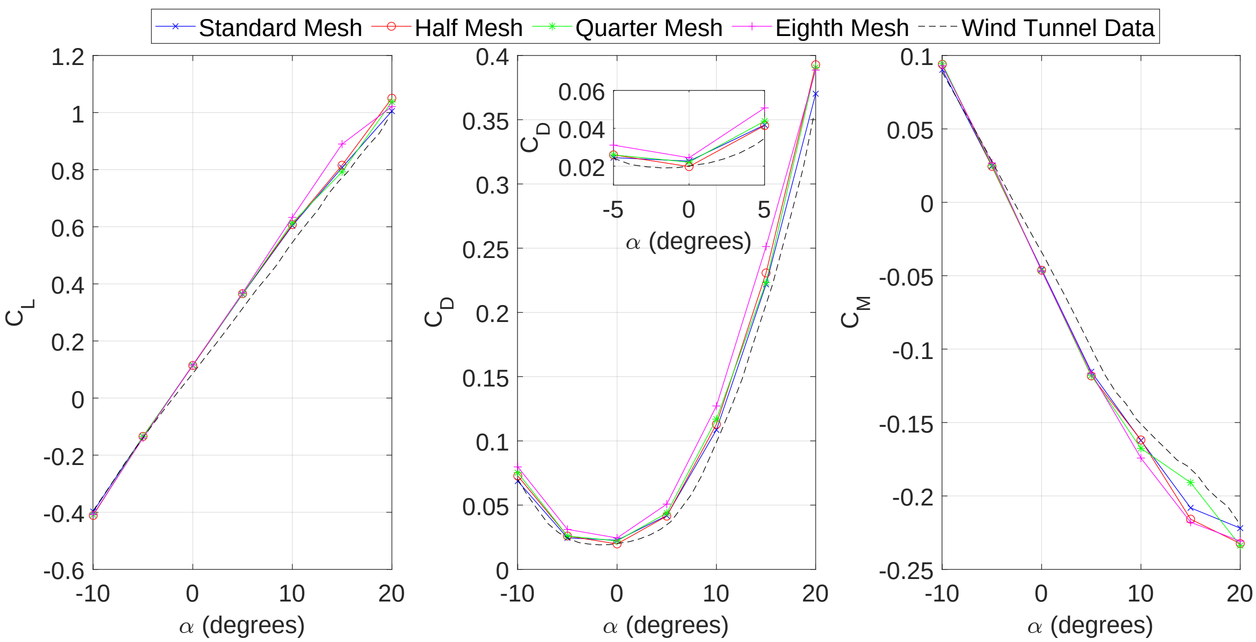

Figure 4.4: Mesh Density Study for the W15 model inside the wind tunnel with the support system

4.2.2 UWS21A

The UWS21A was initially meshed with the previous baseline free-air results of using the 0.01 m target surface size and the 0.0001 m minimum surface size generated a mesh of 60 million cells which initially produced some issues with initial meshing parameters. Scaling the parameters back to the standard settings of a 0.02 m target surface size and a 0.0005 m minimum size which generated a nearly 40 million cell count, rather than the 60 million cell count. From there the medium and rough meshes were generated by doubling and quadrupling the surface sizes respectively. The meshes with target and minimum surface sizes and cell counts are listed in Table 4.4. The SST turbulence model was used for the mesh density simulation for the UWS21A configuration.

Name	Model Target Size (m)	Model Minimum Size (m)	Average Cell Count
Coarse	0.08	0.002	11,300,00
Medium	0.04	0.001	22,400,00
Standard	0.02	0.0005	39,400,00
Fine	0.01	0.0001	60,700,000

Table 4.4: Cell Counts and other parameters for each of 4 different Mesh Sizes for the UWS21A Simulations

The 4 different mesh sizes are all plotted against the wind tunnel results in Figure 4.5. The largest deviation from the wind tunnel results occurs in the fine case, where there is a an under-prediction of both lift and drag at high angles of attack. The pitching moment curve diverges substantially from the other meshes and the wind tunnel models as well, with a slope reversal occurring at 20°. The other 3 meshes, including the standard configuration all match to the wind tunnel results closer with the medium and standard doing the best at matching the pitching moment curve. Otherwise the rough, medium and standard all agree on behavior for small angles of attack, but there is disagreement for the pitching moment, which is the onset of flow separation of the model where the behavior becomes more unpredictable. Noting that the lift diverges at high angles of attack for the fine case, the standard was chosen as the meshing conditions for the rest of the UWS21A simulations for both time efficient simulations while also matching the wind tunnel results the closest.

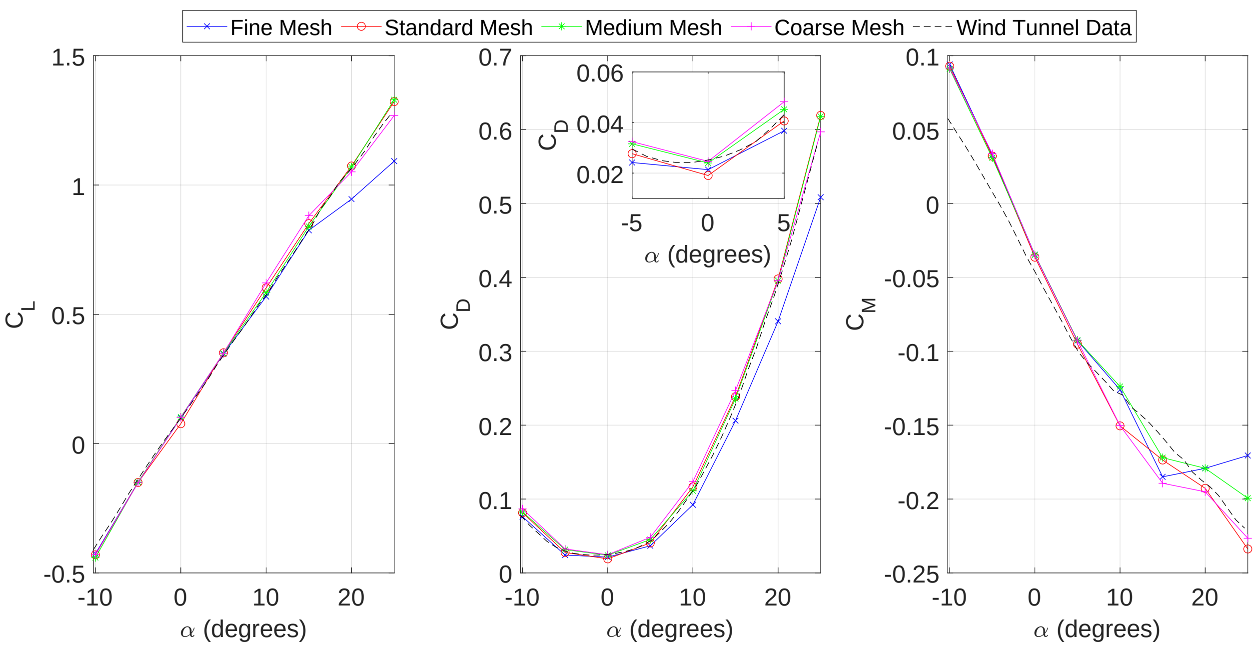

Figure 4.5: Mesh Density Study for the UWS21A model inside the test section and mounted to the model support system.

Chapter 5
FREE AIR SIMULATION ANALYSIS

An initial analysis of the differences between the CFD simulations and the wind tunnel was performed using comparisons between the final corrected wind tunnel data and simulations of the wind tunnel model in free air. Both of these methods should yield comparable results, even with the known difficulties in CFD simulating high angles of attack. However, using the standard or full mesh densities from the prior chapter as a set of baseline simulations, some initial trends are apparent. All results for the pitching moment C_M are located at the 25% MMC location specified in Table 2.2. Specifically for the free air simulation cases, the UWS21A configuration had a larger difference in C_{M0} than the W15 on its own. To further analyze why there is a noticeable change in C_{M0} between the two configurations, a series of simulations "building up" the model from the W15 wing to the full configuration were performed to see where the change in C_{M0} offset comes from. All of the following results use the SA turbulence model. Finally, a small discussion of using CFD to extend the results of the SCALOS tests to a new unproven configuration as supplied, where the corrections used were applied to the final proposed supersonic aircraft configuration included in the final SCALOS report [1].

5.1 W15A and UWS21A Free Air CFD Simulation to Corrected Wind Tunnel data

In Figure 5.1, the results of the standard W15 mesh size are shown and compared with wind tunnel data directly. The CFD predicted less lift at higher angles of attack than the wind tunnel results, which matches with some prior simulations results shown in the mesh density study section. Additionally, while the slope of the pitching moment coefficient curve seems to be replicated closely, the pitch break point, where the slope of the pitching moment curve changes is at a higher angle of attack, but otherwise seems to match the curvature of the wind tunnel simulations results. The L/D plot additionally shows the that the max lift to drag was calculated relatively accurately, but the drag seems to be little under-predicted at higher angles of attack relative to the lift on the model.

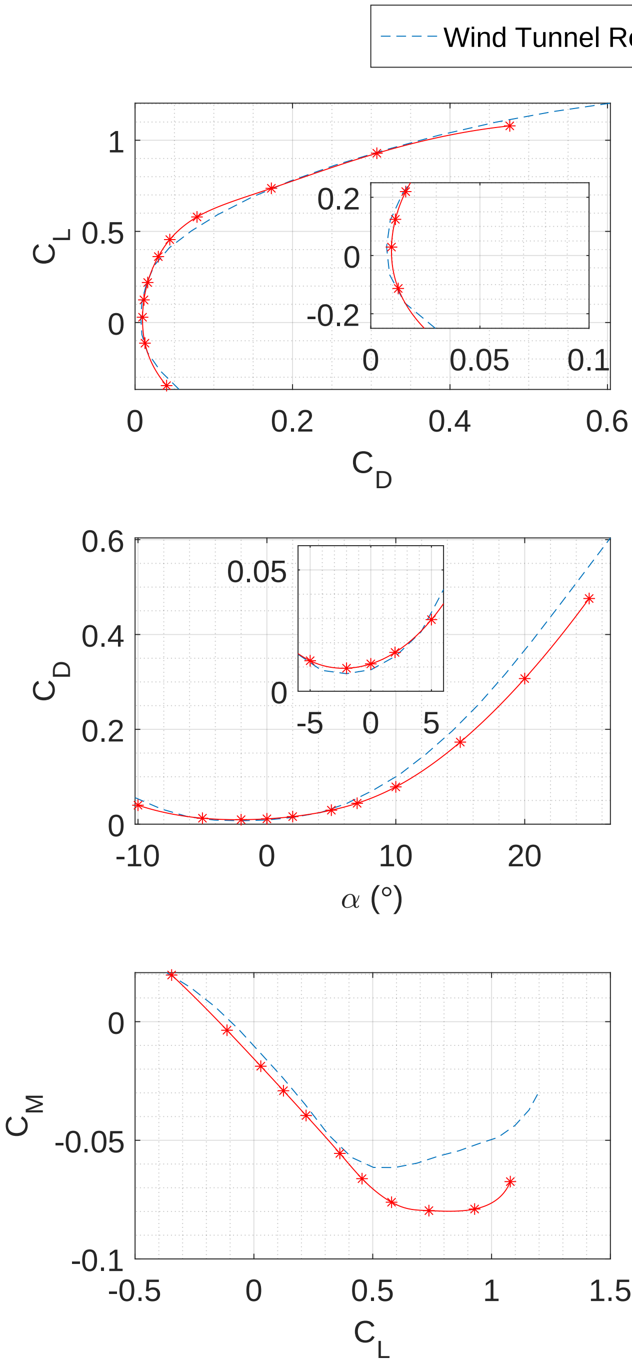

Figure 5.1: CFD vs wind tunnel data for the W15 wing alone

For the full UWS21A with nacelles (for most of the simulations in the following chapters of the thesis, it will be without nacelles to better match with the wind tunnel data) with CFD simulations compared against wind tunnel data is shown in Figure 5.2. The interior of the nacelles were neglected in order to match the wind tunnel corrections where the inside drag of the nacelles were removed from the results. The largest difference between the W15's differences between CFD and wind tunnel results is the larger offset in C_{M0}, where the curvature of the C_M curve is similar to the wind tunnel results, with some deviation after the general deviation point of 15°. The $C_{M\alpha}$ seems to be a bit higher in the low angle of attack region, while the W15 had a far closer slope match over the low angle of attack region. At the high angle of attack, the pitching moment is comparatively less than the wind tunnel results predict, if the C_{M0} offset is removed. There is also a larger difference in C_{D0} compared to the W15 wing.

5.2 UWS21A Configuration Build Up

To determine what particular element causes C_{M0} offset between the W15 and the UWS21A configuration, simulations were run for each intermediary configuration between the W15 and UWS21A configurations, where the order of part addition is starting with the W15 wing, then fuselage, vertical tail surfaces, horizontal tail, canards, and then the addition of the nacelles to reach the final UWS21A configuration presented prior.

5.2.1 Fuselage

For W15 wing and F15 fuselage combination, the comparison between the CFD data and the wind tunnel results is shown in Figure 5.3. The CFD predicted lift is greater than the wind tunnel data, and a slightly greater increase in $C_{M\alpha}$ over the W15 wing alone. However, there is not a significant change in C_{M0} than the W15 wing alone. The high angle angle of attack results remain similar. The fuselage and wing combination's differences between the CFD simulations and wind tunnel data is more consistent with the W15 results than the UWS21A results.

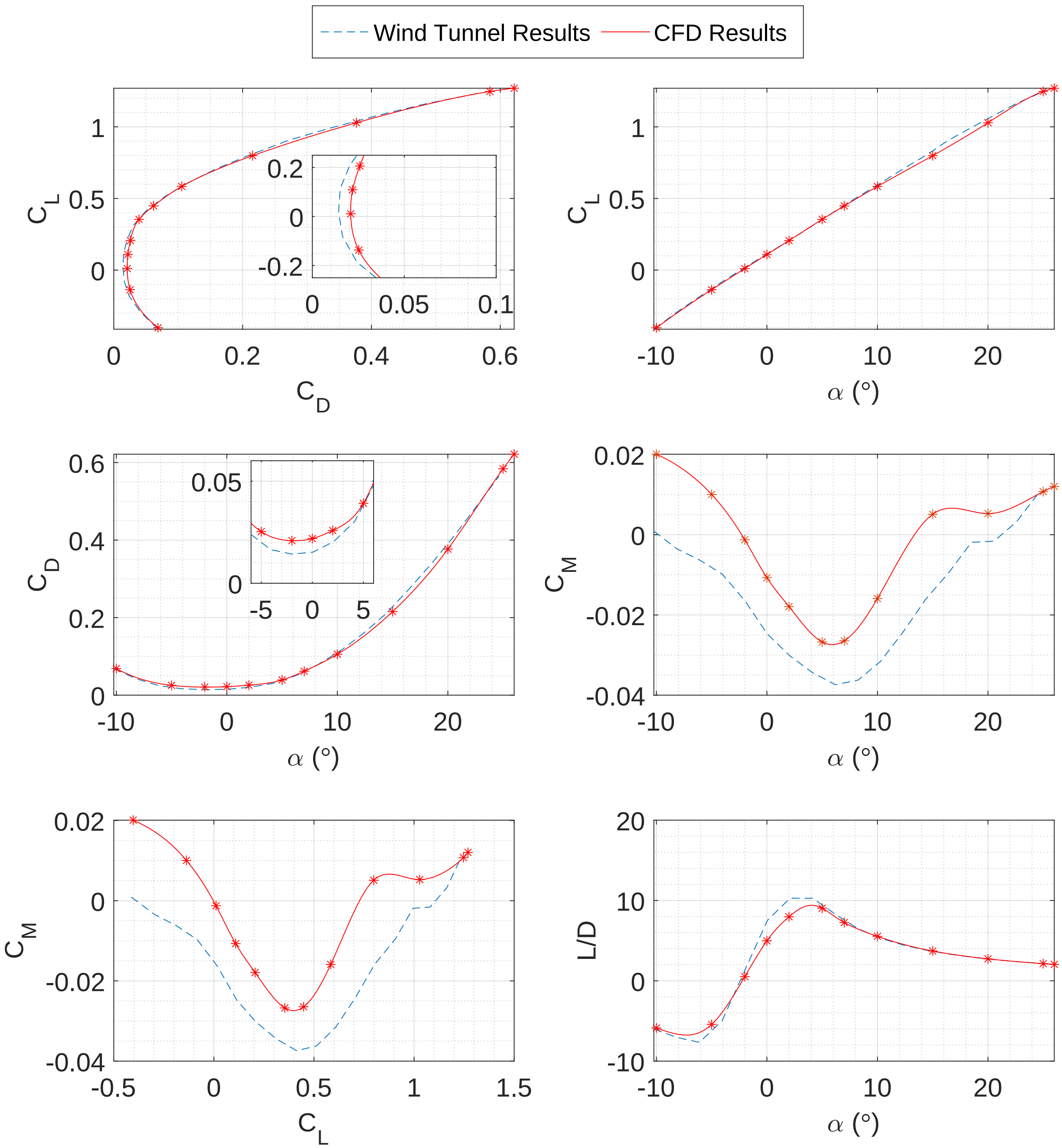

Figure 5.2: CFD vs wind tunnel data for the full UWS21A configuration with nacelles

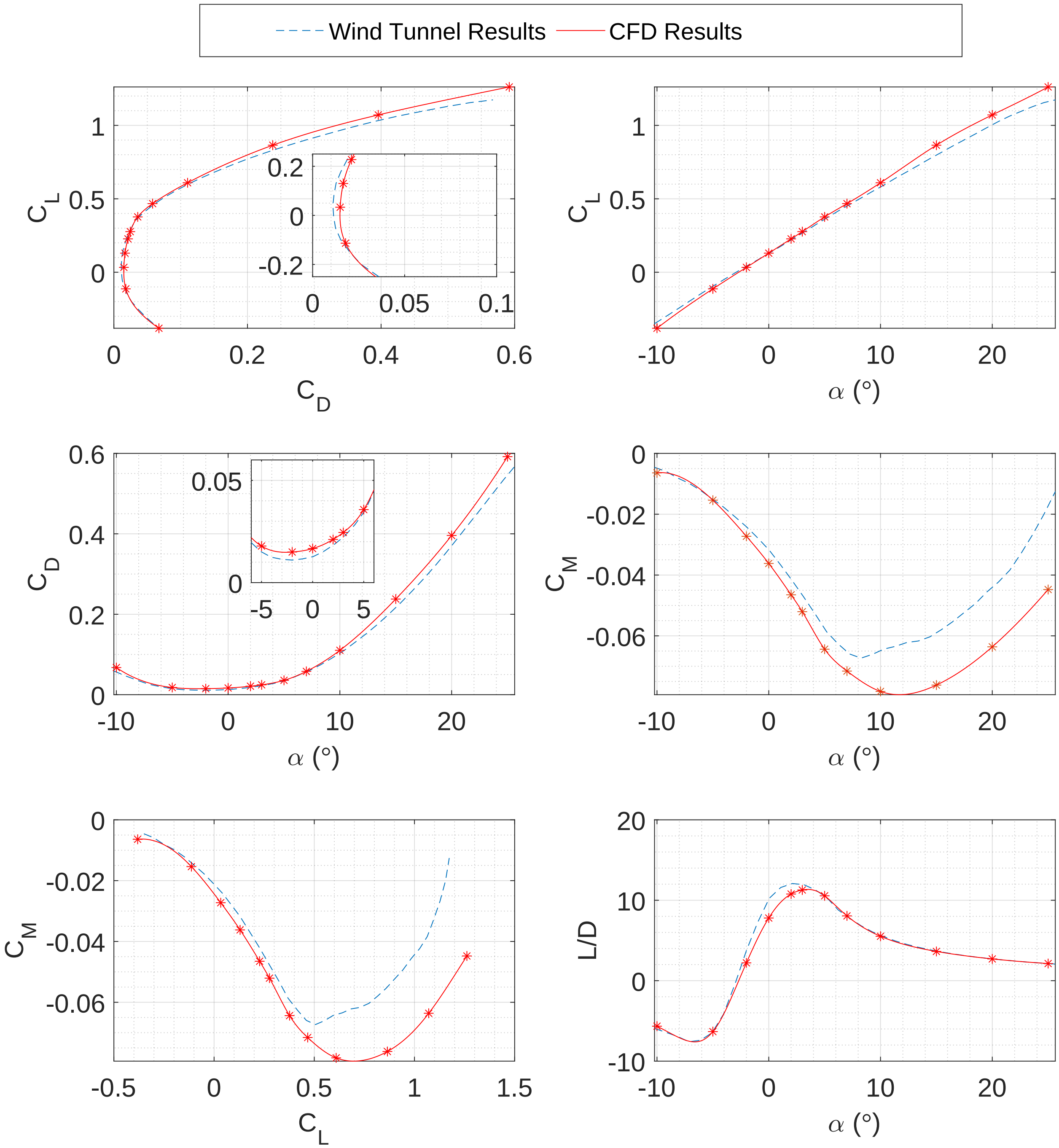

Figure 5.3: CFD vs wind tunnel data for the F15+W15 configuration

5.2.2 Vertical Tail

For the addition of the vertical tail surfaces, the V15 vertical stabilizer, and the VF.1 and DF.1 ventral and dorsal fins respectively were all added to the fuselage. These surfaces were all treated as one component as being run individually was rather rare in the later SCALOS tests and the ventral and dorsal fin by themselves do not add significant effects for a pitch sweep. The comparison between the CFD simulations and wind tunnel data is shown in Figure 5.4. Both Lift and Drag are modeled quite accurately, with the simulations still predicting a slightly greater C_{D0} than the model, but the lift vs drag polar matches closely. For the pitching moment curves, There is the smallest C_{M0} offset out of all of the configurations thus far, but similar to the fuselage addition, the $C_{M\alpha}$ is slightly greater for the CFD simulations. The higher angle of attack variations have some more significant variations, with the pitch break occurring at a higher angle of attack than the Wind Tunnel results, and that once the pitch break is reached, the pitching moment seems to be consistent for $7° < \alpha < 15°$, with a small oscillation. Beyond 15° the pitching moment curve does not fully match with the wind tunnel results.

5.2.3 Horizontal Tail

The low horizontal tail H20.L was then added to the build up with the results shown in Figure 5.5. Both the CFD simulated lift and drag results match closely with the wind tunnel results, with the C_{D0} being slightly greater than the wind tunnel results. The pitching moment curve is where the deviations from the prior trends that were following the W15 results appears, where the the $C_{M\alpha}$ shift from the addition of the fuselage appears, but unlike the vertical tail addition where there was a near zero C_{M0} offset, where here there is a C_{M0} offset of about 0.02, with the new configuration having more of a pitch up tendency than the wind tunnel data. Additionally, the high angle of attach pitching moment data is more variable where the CFD results somewhat match the plateau of the CFD data, but the CFD data presents a greater series of oscillations that would probably require more points to fully resolve whether the changes in pitching moment are physical or oscillations due to the unsteady flow from the high angles of attack.

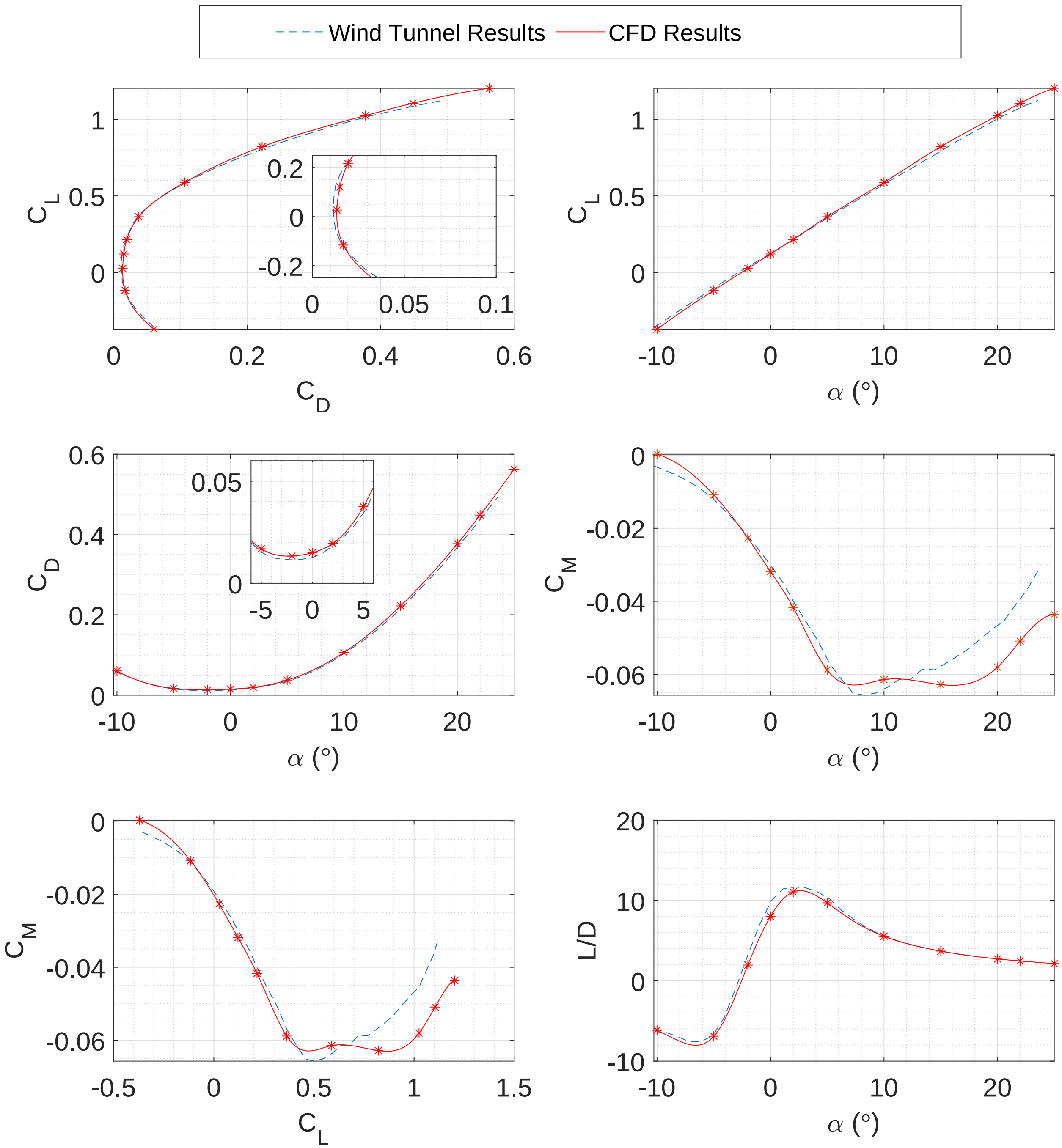

Figure 5.4: CFD vs wind tunnel data for the F15+W15+V15+VF.1+DF.1 configuration

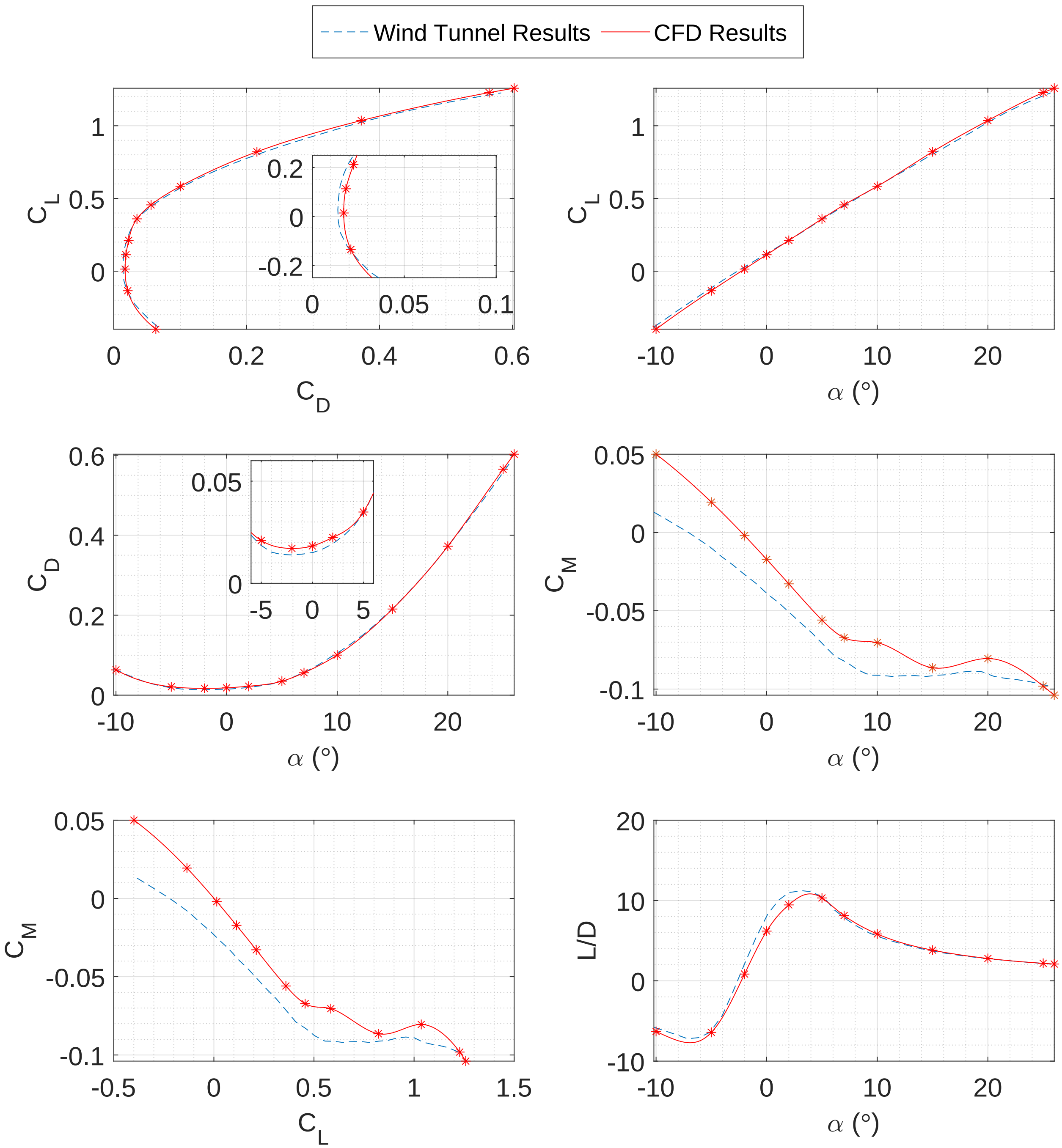

Figure 5.5: CFD vs wind tunnel data for the F15+W15+V15+VF.1+DF.1+H20.L configuration

5.2.4 Canard

Adding the canard to the prior configuration gives the UWS21A configuration without the nacelles or the configuration F15+W15+V15+VF1+DF1+H20.L+C15 configuration. The comparisons of this configuration are shown in Figure 5.6. Notably, the difference between C_{D0} of this configuration is significantly greater than the prior results. However otherwise, the lift and drag both match the wind tunnel results closely. With the addition of the canard, the pitching moment curves still seem to have an offset of $\Delta C_{M0} = 0.02$, with a greater $C_{M\alpha}$ being greater than the wind tunnel results as well. However, unlike the prior vertical stabilizer test, the higher angle of attack data seems to follow the wind tunnel results consistently with a C_{M0} offset. However the CFD data seems to lack many of the more small scale variations that the wind tunnel data has.

5.2.5 Analysis of Zero-Lift Pitching Moment Offset due to the effect of the Horizontal Stabilizer

Synthesizing the results of the model build up with a focus on the pitching moment yields the following figures: Figure 5.7 shows the CFD results on the left and the wind tunnel results on the right, while Figure 5.8 shows the same data plotted on top of each other for a more direct comparison. While the general behavior trends of the CFD results capture the same trends as the wind tunnel results in the AOA range of -10 to +10 degrees, such as the general location of the pitch-up break (notability the F15+W15+V15+VF.1+DF.1+H20.L+C15 seems to miss this by a couple of degrees), the actual values are separated by an offset. The configurations without a horizontal stabilizer have a better match in C_{M0} than configurations with it.

Note that the CM analysis/test curves of the wing-only configuration (in dark blue) match quite well at negative angles of attack, with the mismatch becoming larger as the AOA grows. Beyond 10° AOA, the theory and test curve trends diverge, which is not surprising given the difficulty of capturing stalled flow with strong vortex “action” by RANS CFD. The F15+A15+W15 and the F15+A15+W15+V15+VF1+DF1 configurations also show a reasonable theory/test match at low angles of attack, with increasing offsets as the AOAs grow. The addition of the horizontal tail leads to a significant offset between theory and test over the whole AOA range, including small AOAs.

An illustration of the effect of adding the horizontal stabilizer on the analysis/test results mismatch is shown in Figure 5.9. The configurations in the build-up sequence before adding the H20.L

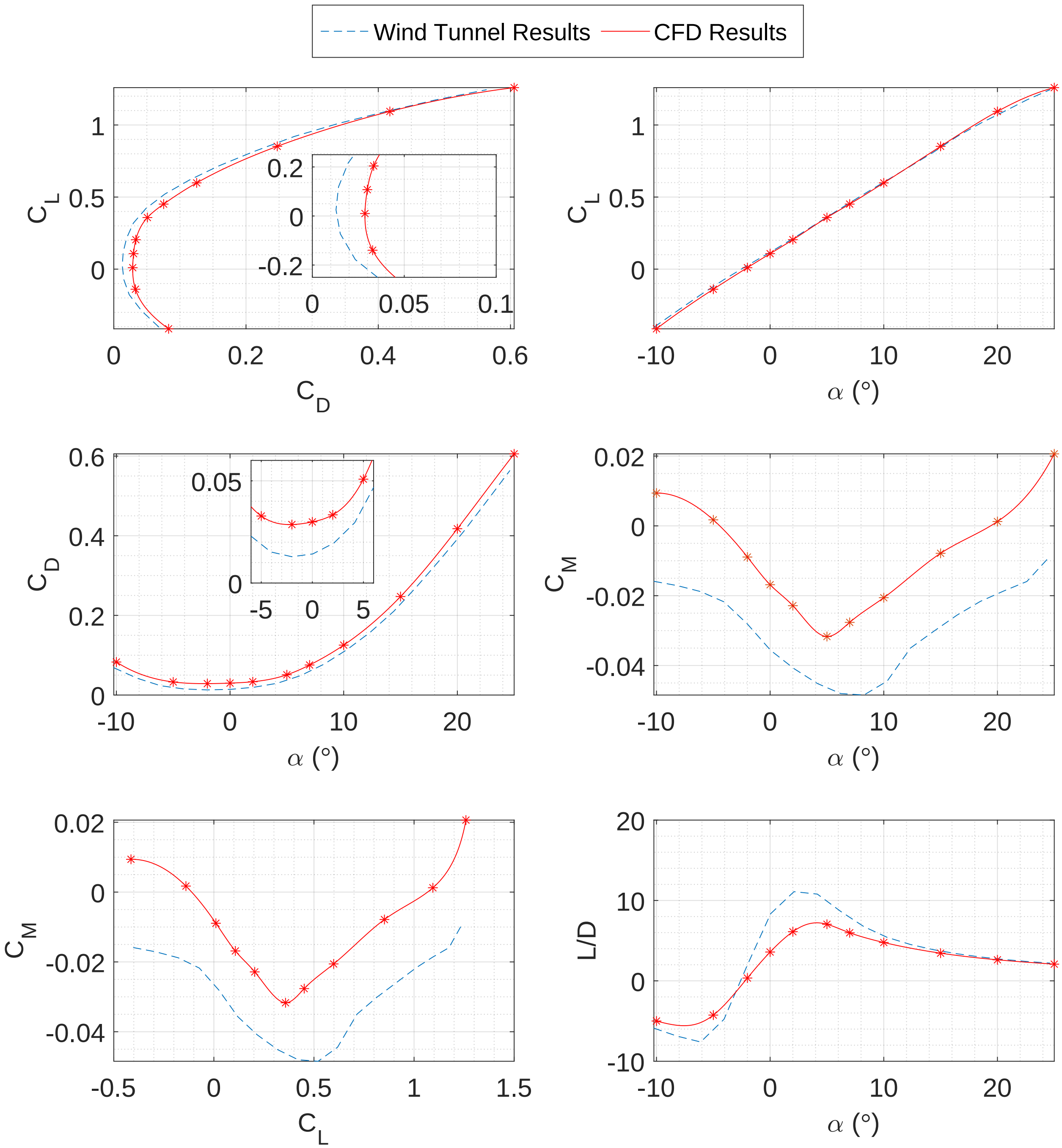

Figure 5.6: CFD vs wind tunnel data for the F15+W15+V15+VF.1+DF.1+H20.L+C15 configuration

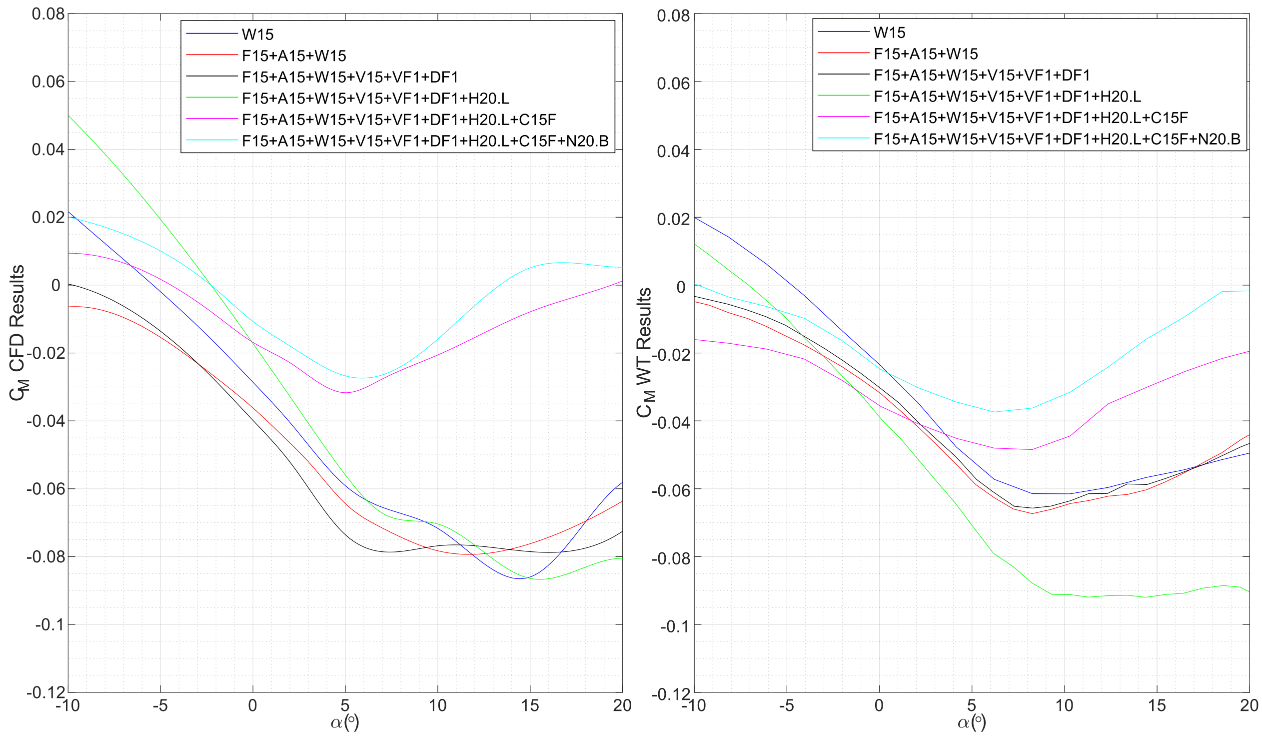

Figure 5.7: Comparison of the C_M vs α behavior for the CFD results (left) and the WT results (right) - free air.

horizontal tail all have small differences in CM results at -10° α and the error seems to increase more or less linearly as the AOA α increases.

This behavior could be explained by the horizontal tail seeing a different angle of attack of flow in the simulations as compared to inside the wind tunnel, as a C_{M0} offset is similar to the effects of rotating the horizontal stabilizer to a different deflection angle. However, with the horizontal stabilizer being mounted in CAD using copies of the same parts used in the wind tunnel, so a mismatch between the CFD geometry and the actual wind tunnel model is unlikely. This means that the downwash angle from the wing interacting with the horizontal stabilizer differently in the free air in comparison to the wind tunnel. This will be discussed in more detail later on in the T&I section where the offset appears again.

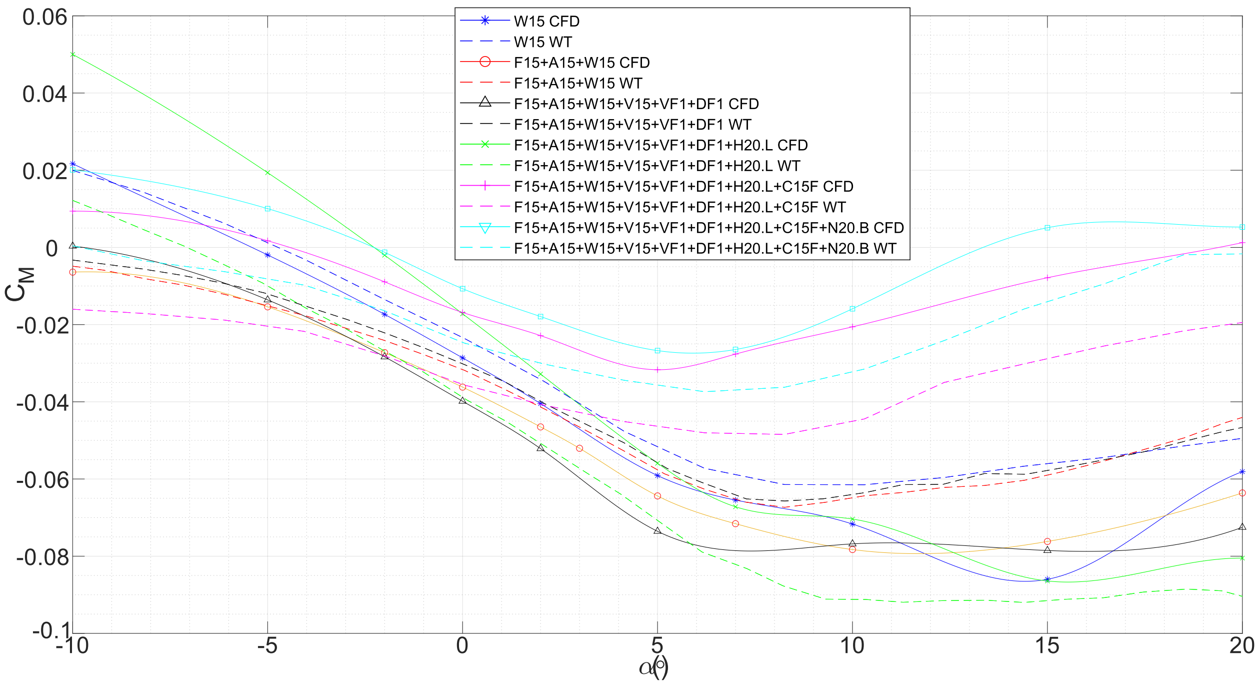

Figure 5.8: Superimposing the two plots of Figure 5.7 for direct comparison

5.3 *Alternative Wing Comparisons*

Alongside the wind tunnel tests that the SCALOS program conducted, there was an effort to design a more refined proposal supersonic transport concept than what was initially used for the wind tunnel model's design. This new design was a derivative from the UWS21A. This more refined design altered the individual cross-sections of both the wing and fuselage, changing the more generic geometries of the UWS21A to a more refined or representative design of supersonic configurations. The new wing geometry called the RW23 was simulated in CFD to create a set of increments to the wind tunnel data to provide more a more accurate predictions of the behavior of the improved supersonic transport concept.

5.3.1 RW23 Context

The RW23 wing has the same planform and angle of incidence as those of the W15 wing. But instead of a geometrically untwisted wing with relatively constant thickness (the W15), the RW23 has a

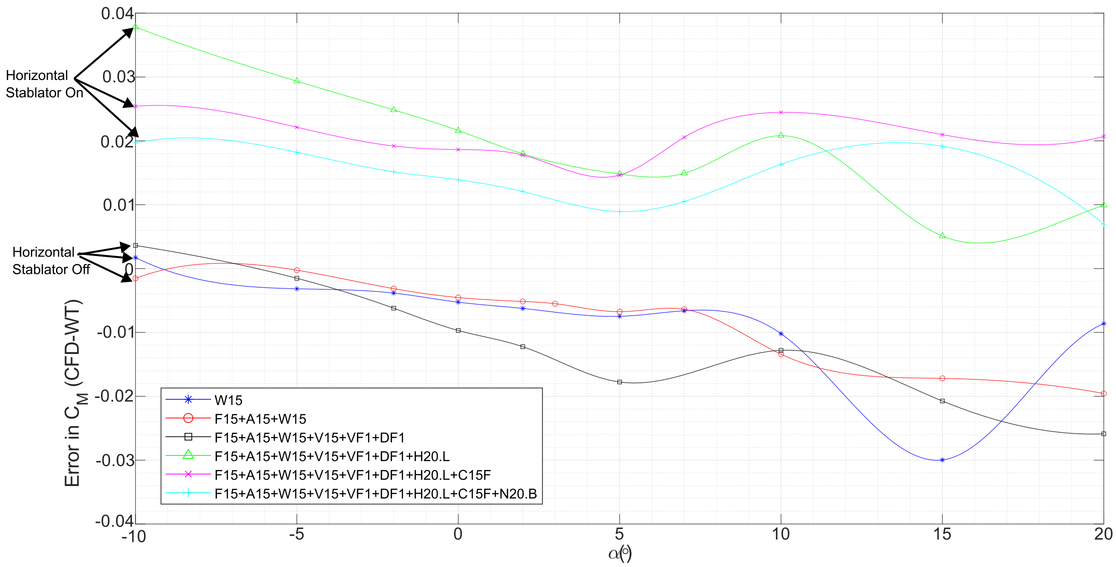

Figure 5.9: The differences between the CFD CM results and the corrected WT CM results

wing with both geometric and aerodynamic twist and thickness distributions more similar to wing designs representing an optimized supersonic cruise shape (e.g. HSCT (Ref. [18]) or N+2 concepts, Ref. [8]). The RW23 wing shares the same planform as the W15 wing, where all of the wing's main dimensions are the same, with the airfoils and wing twist being different. Figure 5.10 shows the new twist distribution for the RW23 wing with the spanwise location being the distance in inches from the centerline of the model for the full scale aircraft. The minimum point at 300 inches is located at the point on the wing where the wing sweep changes. Figure 2.2 shows the airfoils of the W15 wing stretched vertically for better visibility, and Figure 5.11 shows the airfoils of the RW23 with their normalized semi-span locations. The wing shape for RW23 (airfoils, aerodynamic twist) is not optimized, but was chosen to provide a wing loft more representative of cranked supersonic planform optimized using higher-order non-linear CFD tools (full-potential/Euler/RANS) - see Ref. [19]. Both the W15 and RW23 have a 1.5° wing incidence that was retained for their wing alone studies to better match the rest of the full aircraft studies.

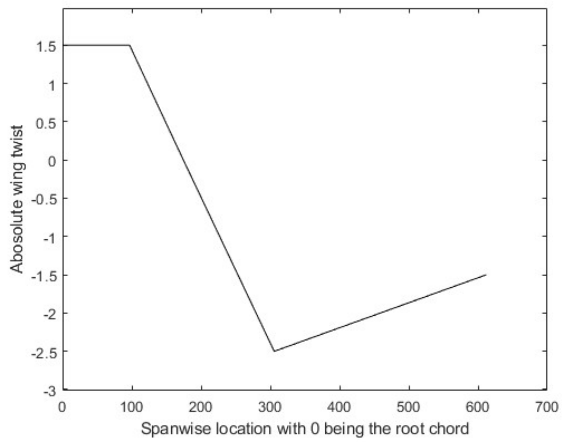

Figure 5.10: Plot of the twist of the RW23 Wing vs Semi-span

5.3.2 Wing Comparison

As the RW23 was not tested in the wind tunnel, the estimation of its characteristics based on the wind tunnel data was necessary for performance calculations. This also serves as an example of how the SCALOS data can be used to fine tune, by increments, estimated CFD-based aerodynamic characteristics of supersonic commercial configurations that are close but not identical to the ones that were tested. Figure 5.12 shows the results of wing-alone simulation results where the W15 CFD results are in good agreement with corrected wind tunnel results over a range of AOAs from -10 to about 8 degrees in CM and up to 25 degrees in lift. The C_{D0} is off a bit but not by much.

For the RW23 case, the new airfoils and twist washout on the wing delay the CFD-predicted pitch break point by 12 degrees, also shifting the C_{M0} value to 0 for minimizing trimming by control surfaces. The C_{D0} values are shifted to be closer to the max L/D location, helping the subsonic cruise speed conditions, even though the wing loft is intended to better represent a representative supersonic twist and camber.

Since both the W15 and RW23 wing were meshed similarly, any increments between corrected experimental and simulation results for the W15 wing can be applied here as well. For a complete configuration we can use CFD/test increments for a configuration that is close to another configuration in development for for better estimation of what corrected WT test results for that

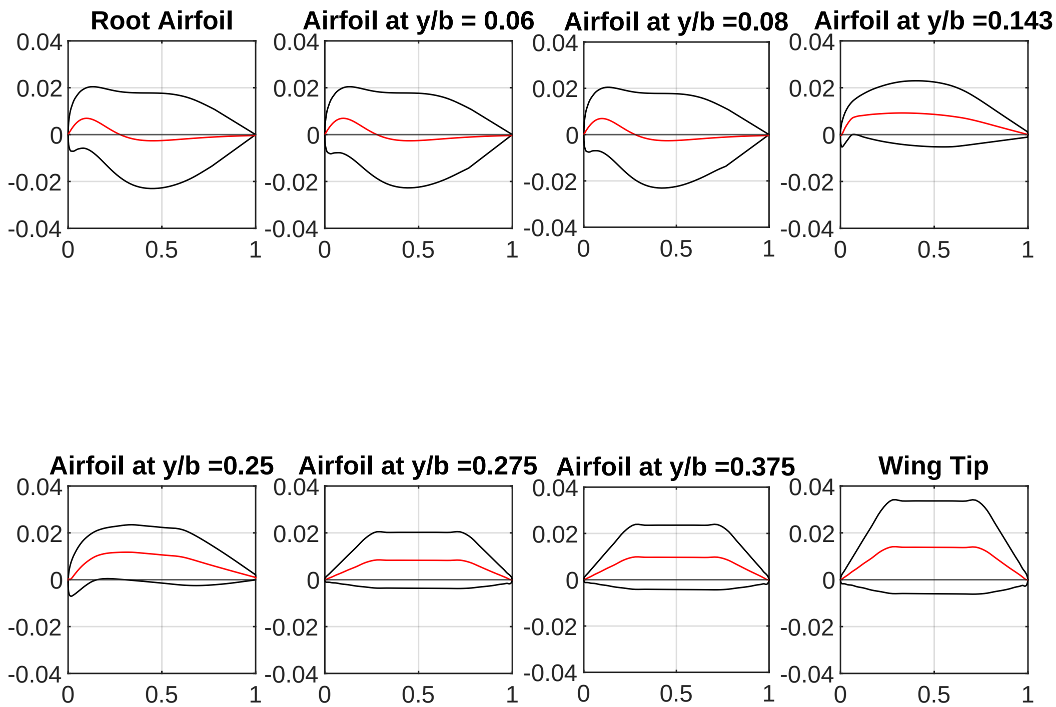

Figure 5.11: Plot of the RW23 airfoils (vertical scale exaggerated for clarity)

configuration would yield.

Analyzing the wing + fuselage configurations where the fuselage is the F15 fuselage and the wings are the W15 and the RW23 wings. Using STAR-CCM+ the F15 fuselage was placed on top of both wings. The simulations produced the results shown in Figure 5.13. The F15+W15 case had 38536200 cells, and the F15+RW23 case had 37574845 cells, with both using the 2500 in diameter spherical far field.

There is a greater difference with the F15+W15 CFD and wind tunnel results, where the AOA of the pitch up tendency is increased for the F15+W15 and the slope of the pitching moment curve is smoothed to a far greater degree. The simulations predict slightly higher lift at higher angles of

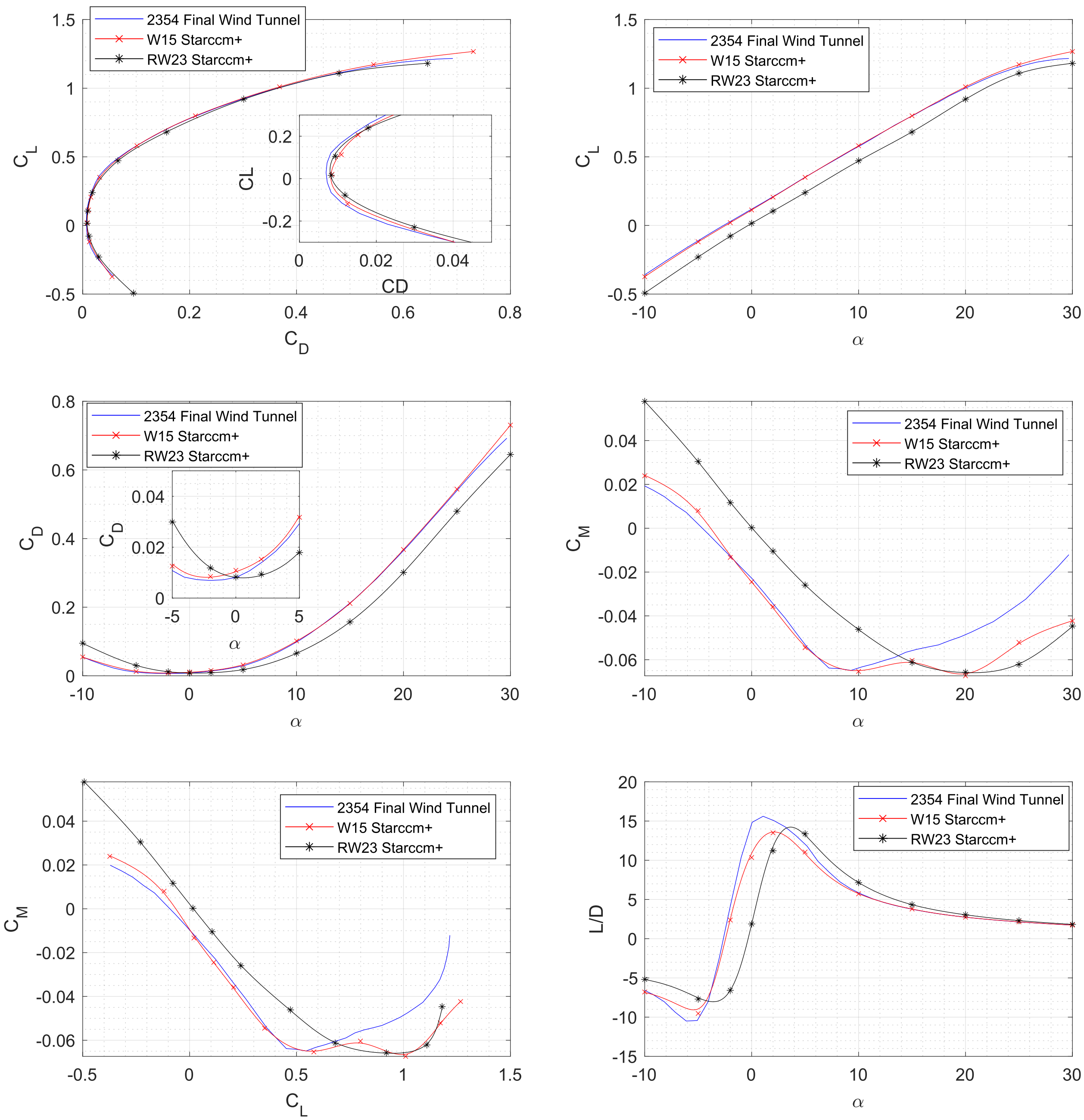

Figure 5.12: Comparison of W15-alone CFD and wind tunnel results with the RW23-alone CFD results

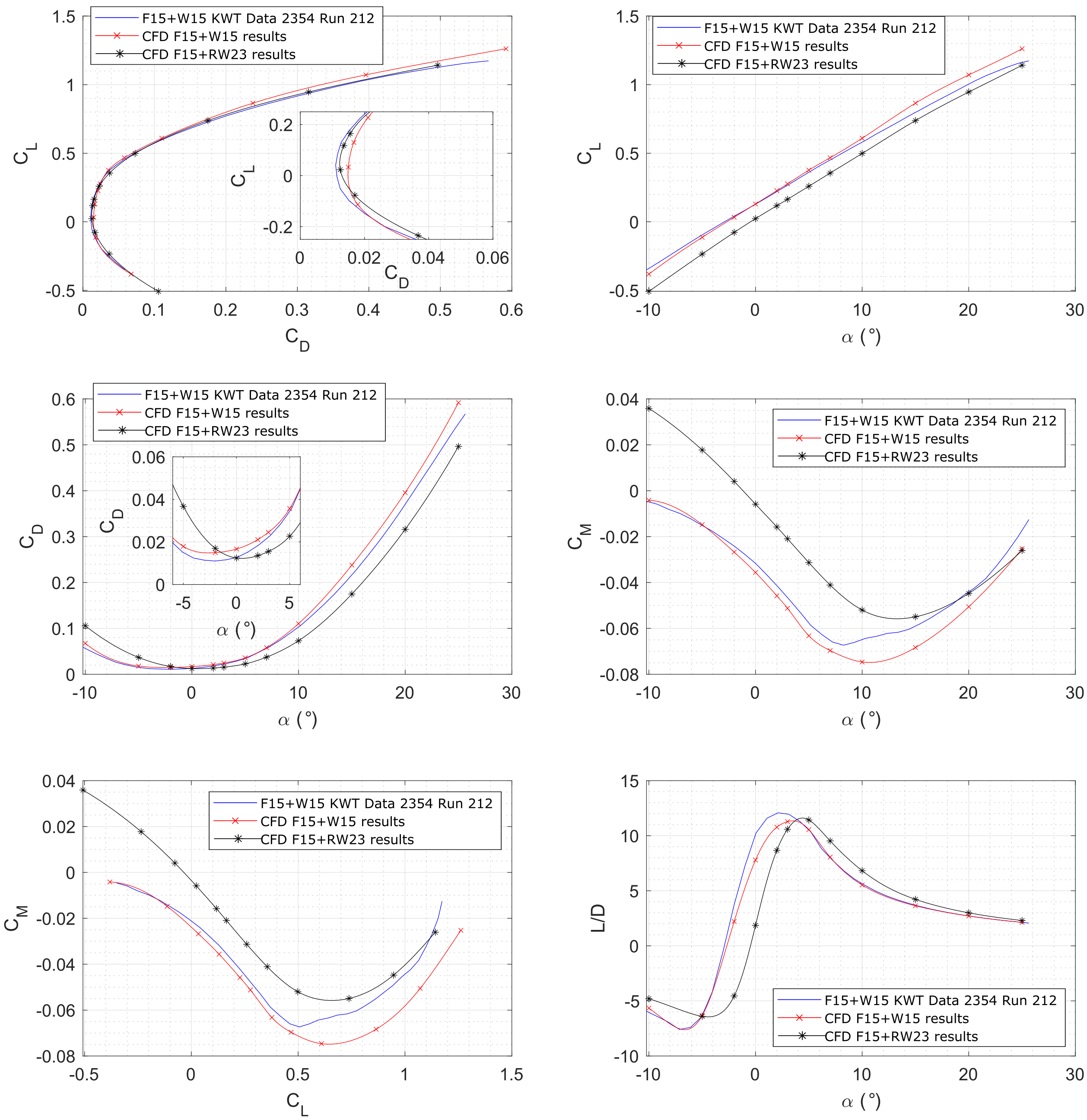

Figure 5.13: Comparison of the W15 CFD and wind tunnel vs RW23 wing with the F15 fuselage.

attack, suggesting that there may be additional vortex lift being generated than originally predicted. The addition of the fuselage shifted the C_{M0} value of the RW23 down to -0.0035, which still requires a bit of stabilator deflection to trim the aircraft at the speeds tested at the wind tunnel. Or that the CG location for the full scale configuration needs to be shifted further aft than the CG location for the SCALOS model. Checking the wing and fuselage combination against the wing alone cases allows for a more direct increment between full configurations, rather than the wing alone case which may introduce some additional behavior due to the geometry of the wing covered by the fuselage, however this could also be replicated by applying the increment of adding the fuselage predicted by the wind tunnel results as well.

Figure 5.14 shows correction increments, CFD-based, between the W15 and RW23 wing-only cases. In a similar way CFD increments between a new configuration of interest and a similar SCALOS configuration for which corrected wind tunnel data is available can be used to obtain estimated corrected wind tunnel data for the new configuration. The utilization of CFD-based increments can be used to remove or add components to configurations of interest by CFD and then applying the increments to the appropriate test data.

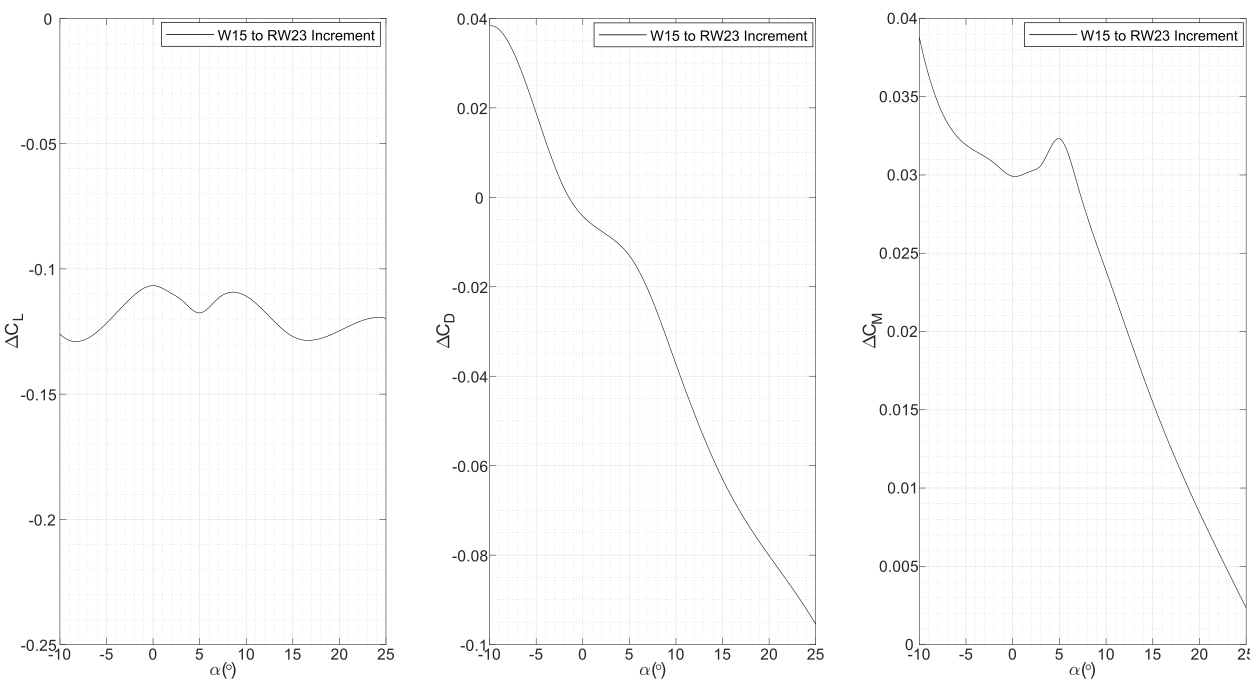

Figure 5.14: Corrections for changing W15 CFD data to RW23 CFD results

This analysis of the new configuration gives an additional example of the interconnected relationship between CFD and wind tunnel testing, where wind tunnel data can provide a baseline set of results for an unrestricted set of angles of attack, to then being able to iterate on a design using CFD for new configurations and to create a set of deltas to translate one configuration to another.

Chapter 6

TARE AND INTERFERENCE CORRECTIONS

The 3-step T&I process discussed in the introduction has been analyzed for 3 different configurations, W15, UWS21A, and the UWS20A. For the T&I process, the three steps are "Step A": the model upright on the MPS, "Step B": the model inverted on the MPS, and "Step C", the model inverted on the MPS with an image MPS above the model. A visualization of the process is shown in Figure 1.1 where the process is shown. To obtain the model in the test section without the MPS, "Step D", "Step A" and "Step B" are summed together and then have "Step C" subtracted from them. For the W15 wing and the UWS21A, the full T&I process is simulated in CFD and compared against the "correct" result "Step D". The UWS20A has a single step CFD fork tare produced for it compared against the correction applied by the wind tunnel data.

For the three different sweeps performed, an AOA sweep for both the W15 and UWS21A configurations, and a side-slip sweep at an α of $0°$, the T&I process was computed using the simulation results for "Step A", "B" and "C" and then compared to the results from a simulation of "Step D". With "Step D" lacking any directly measured wind tunnel results to support it, it exists as the theoretical ideal result from the T&I method with no support system influence on the model or from a generic strut tare on the model. Additionally two other comparisons are made to the results: the original "Step A" results as a comparison to what the T&I process does to the data, and the "Step A" result with only the forces and moments of the wind tunnel model, without the support system. The forces and moments of only the wind tunnel model in "Step A" provide only what the model sees, but the flow field around the model is still disturbed and changed by the presence of the fork, which means that this result deviates a fair amount from the "Step D" result.

Additionally, to see how the results may change, both the SA and SST use used for every configuration to analyze the effects of different turbulence models to determine the differences between the models and to see how much the corrections may vary from case to case. This comparison will seek to establish if one turbulence model is better than the other for the low speed characteristics of supersonic aircraft configurations. For the KWT's data reduction process, the T&I corrections are applied as a set of extra tares which are applied before moment transfers so all simulations presented in this chapter have their moments resolved at the balance moment center.

6.1 W15

6.1.1 Wind Tunnel Data Validation

The results of the CFD simulations of both the SA and SST turbulence models of the W15 wing from $\alpha = -10°$ to $\alpha = 20°$ for the T&I Steps of A, B, and C inside the tunnel are shown in Figure 6.1, 6.2, and 6.3. For "Step A", the SST and SA models generally match quite well, with minor deviations. The zero lift drag from the SST model is predicted to be higher, however this could be tuned with prism layers and mesh settings if higher precision is required. For 15° AOA, the lift is over predicted for the SA case than the SST case, but both show a slight change in slope over the wind tunnel results and a general over prediction. Both the SA and SST results agree with one another for the pitching moment results, but there is slight difference in slope at small AOA, and has the change in pitching moment slope located at a different point, where there is a larger deviation in pitching moment at 15° AOA than the rest of the points. For both "Step B" and "Step C" the results similarly match the trends shown in "Step A", there are cases where the SA and SST turbulence models deviation from one another. The SST model under predicts the lift of the model in "Step B" and C , but for "Step B" the SST model better matches the wind tunnel results, with the SA model over-predicting lift at high angles of attack. However the SA model still has a consistent trend for "Step B". For "Step C", the SA model better matches the wind tunnel results at high angles of attack, while the SST model under-predicts the lift. The SA model predicts less drag than the SST model, where it gives a slightly more accurate zero lift drag for "Step B", but under-predicts for "Step C", where the SST model better matches the wind tunnel results. For pitching moment, the SST model better captures the magnitude of the wind tunnel results, but the SA model keeps a consistent trend that matches a more rotated pitching moment curve. For the W15 wing, either turbulence model will serve for the T&I process analysis as both capture the trends shown in the wind tunnel results equally well.

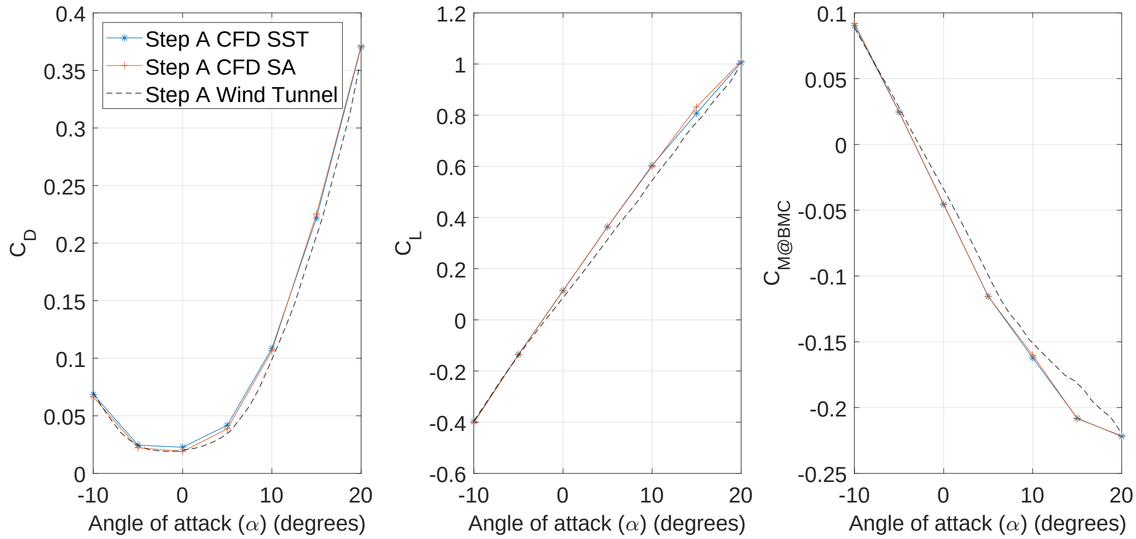

Figure 6.1: Comparison of the SA and KWT turbulence models against Wind Tunnel Data for T&I "Step A" configuration

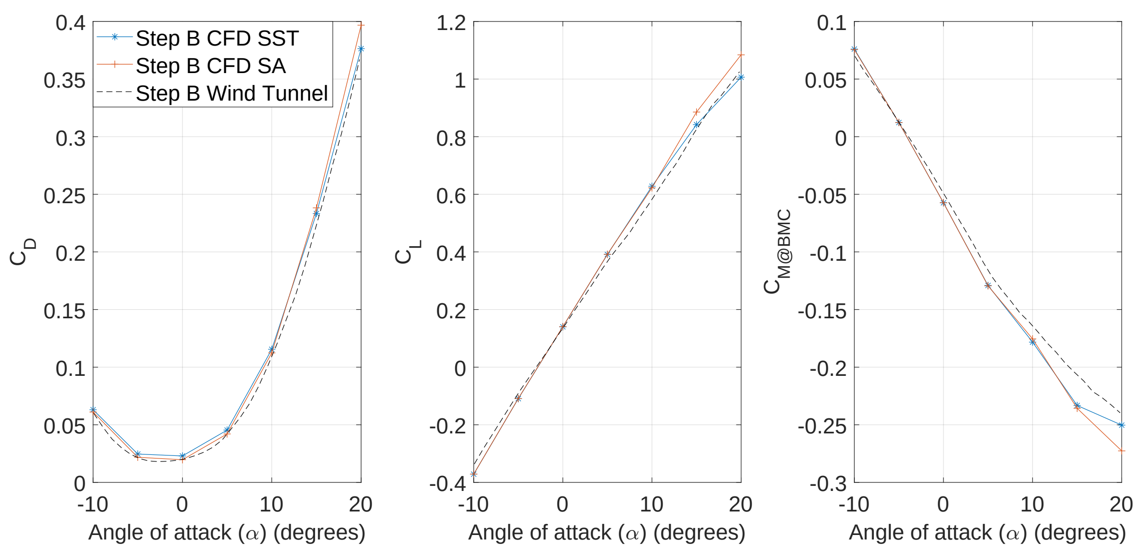

Figure 6.2: Comparison of the SA and KWT turbulence models against Wind Tunnel Data for T&I "Step B" configuration

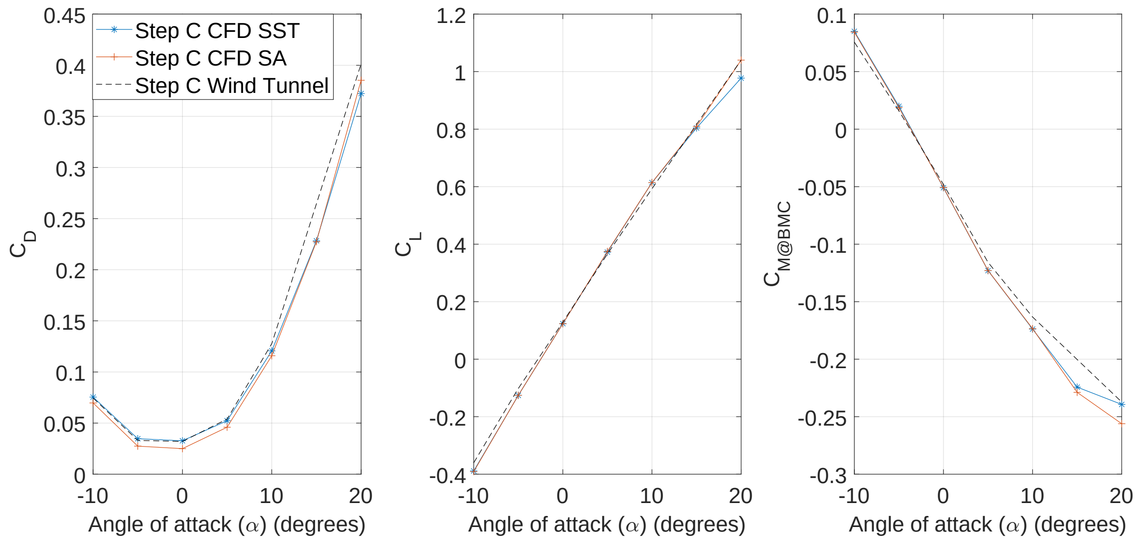

Figure 6.3: Comparison of the SA and KWT turbulence models against Wind Tunnel Data for T&I “Step C” configuration

6.1.2 Comparisons of the Simulated T&I Process and the “Step D”

For the W15 wing on its own, the CFD data matched closer to the wind tunnel results than for the full aircraft configuration, and with more consistent deviations. Given this, a CFD based T&I adjustment should be quite robust for wind tunnel testing, provided that the method accurately captures the aerodynamics around the model. All further discussions in this section for the W15 wing are about the CFD simulations, with all references to the T&I steps being the simulated results. The comparison of the CFD simulations for the “Step A” result, the forces and moments of only “Step A” on the model, and the T&I computed result are compared to the simulation results of “Step D” in Figure 6.4 for the SA turbulence model and in Figure 6.5 for the SST turbulence model. The simulated T&I method is the closest comparison to the “Step D” results, where only it can account for the offset in lift and the translation seen in the pitching moment curve. For an overall all comparison of the accuracy of the results, the SST method ends up to be slightly more accurate than the SA model, as the lift results for the SST turbulence model end up right on top of each other, while at high angles of attack the SA turbulence model deviates in the T&I results. However the SA turbulence model is slightly better in pitch, maintaining T&I accuracy to 15° AOA

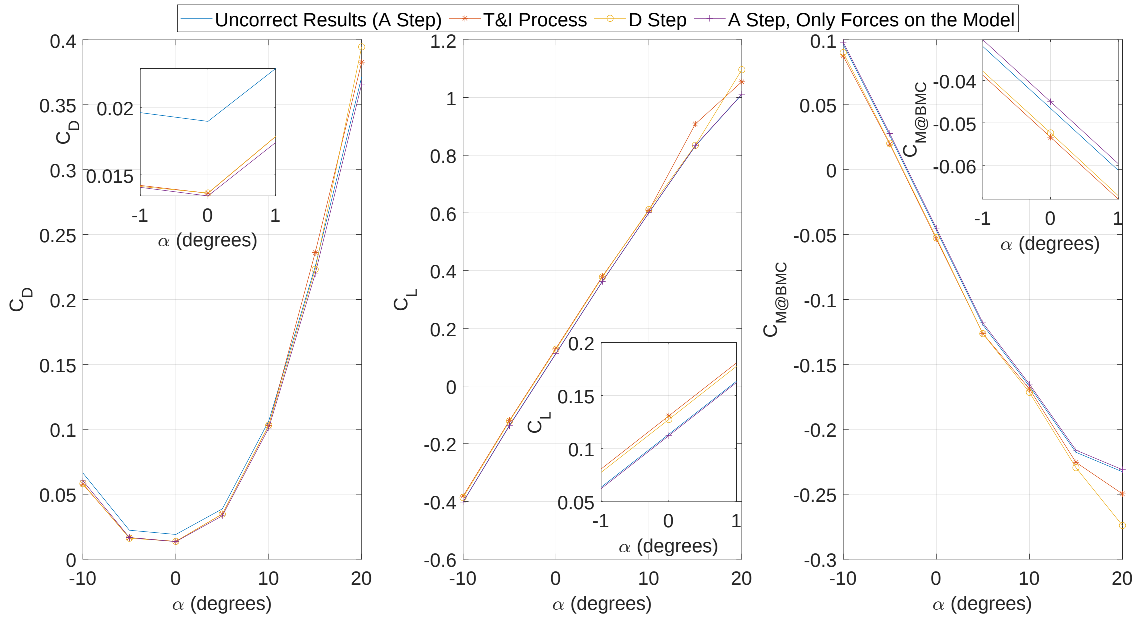

Figure 6.4: Comparison of the T&I process with the SA turbulence model and 2 other results for the W15 wing to "Step D" configuration

before diverging from the "Step D" results. The SST model disagrees at 15° AOA in lift, before having agreement at 20° albeit with a smaller correction magnitude.

Notably, looking at behavior around $\alpha = 0°$, the T&I method matches the lift and pitching moment behavior of "Step D" the closest, and maintains that relationship through all higher angles of attack as well even with the prior deviations discussed prior. The only notable deviations occur at higher angles of attack in pitch, but the T&I case is still the closest out of the three methods at $\alpha = 15°$, with the uncorrected results suggesting a greater pitch up tendency. This is consistent between both turbulence models, with the uncorrected "Step A" and the "Step A" only forces and moments on the model comparison being offset to the T&I results. Notably the "Step A" only the forces and moments of the model that comes close to matching the accuracy of the T&I method to "Step D" a close match in $C_{D_{Min}}$, but once larger contributions of induced drag are added at higher angles of attack, the forces and moment can't account for the increase in lift the model experiences.

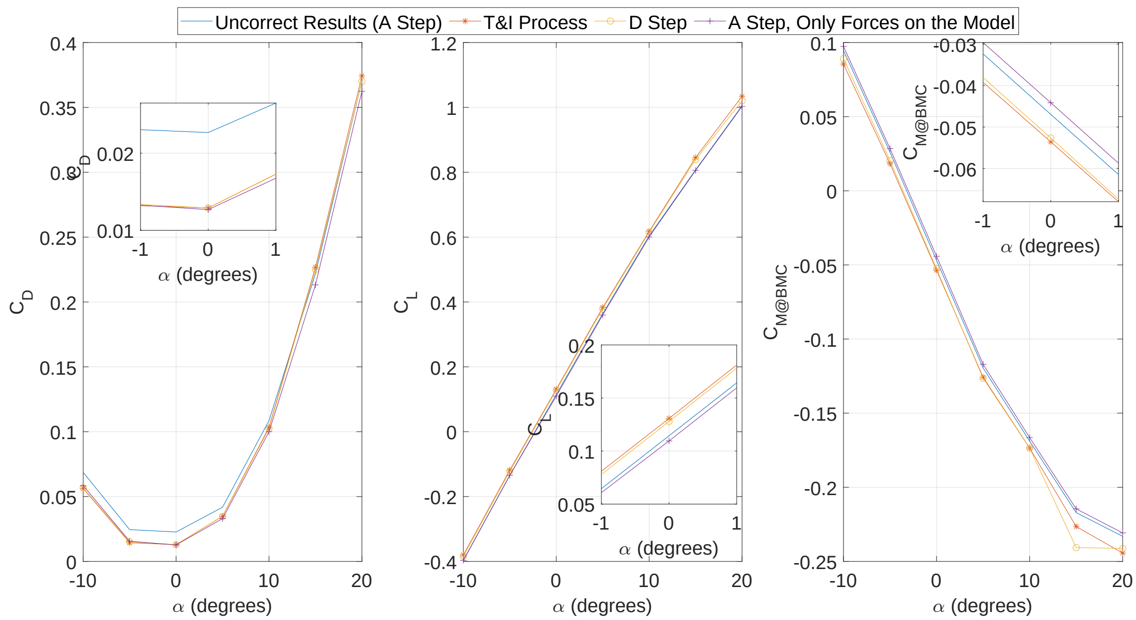

Figure 6.5: Comparison of the T&I process with the SST turbulence model and 2 other results for the W15 wing to "Step D" configuration

6.1.3 Correction Magnitude Comparison

For the W15 wing on its own, the CFD data more closely matched to the wind tunnel results than for the full aircraft configuration, and with more predictable deviations. With this, the T&I adjustment should be quite robust for wind tunnel testing, provided that the method accurately captures the aerodynamics around the model. The comparison of the "Step A" result, the forces and moments of only "Step A" on the model, and the T&I computed result are compared to the simulation results of "Step D" in Figure 6.6 for the SA turbulence model and in Figure 6.7. The T&I method is the closest comparison to the "Step D" results, where only it can account for the offset in lift and the translation seen in the pitching moment curve. For an overall all comparison of the accuracy of the results, the SST method ends up to be slightly more accurate than the SA model, as the lift results for the SST turbulence model end up right on top of each other, while at high angles of attack the SA turbulence model deviates in the T&I results. However SA is slightly better in pitch, maintaining T&I accuracy to 15° AOA before diverging from the "Step D" results.

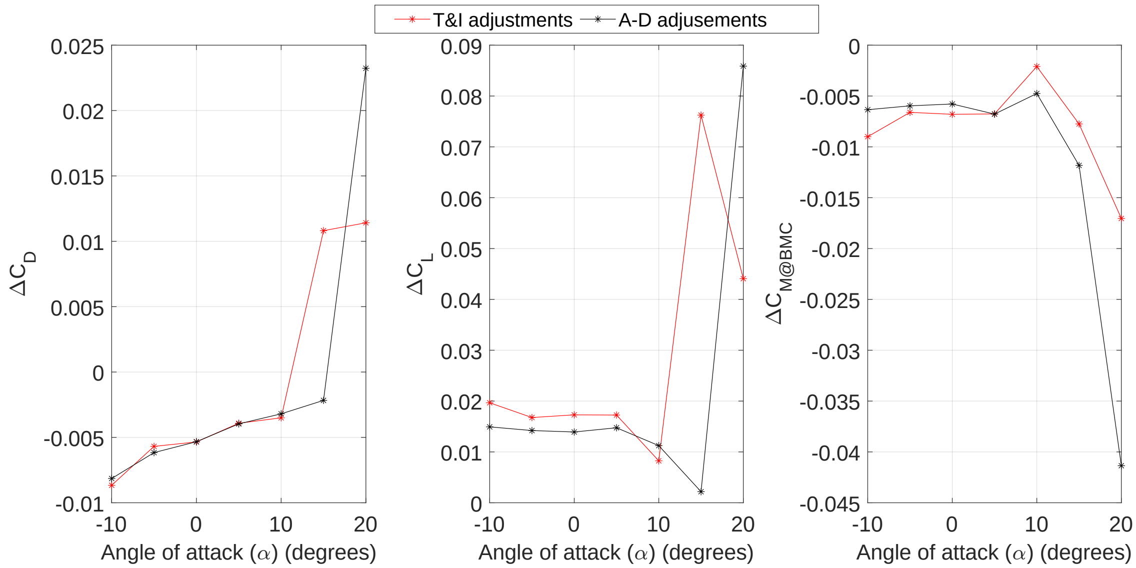

Figure 6.6: Difference in the magnitude of the adjustments for the W15 wing for both the T&I method and directly subtracting the two with the SST model.

The SST model disagrees at 15° AOA before having agreement at 20°.

For a final comparison between the "Step D" CFD results and the wind tunnel data, the wind tunnel results with the T&I process applied are shown in Figure 6.8 and compared with the "Step D" simulation of the W15 wing. Both Lift and Drag match well, with SA matching very closely and SST slightly under-predicting lift and drag compared to the wind tunnel results. Additionally, the pitching moment curve matches quite closely with both the SA and SST turbulence models deviating slightly at 15° and 20°. In all, for the W15 wing, the CFD correction serves just as well as the correction applied through the T&I testing.

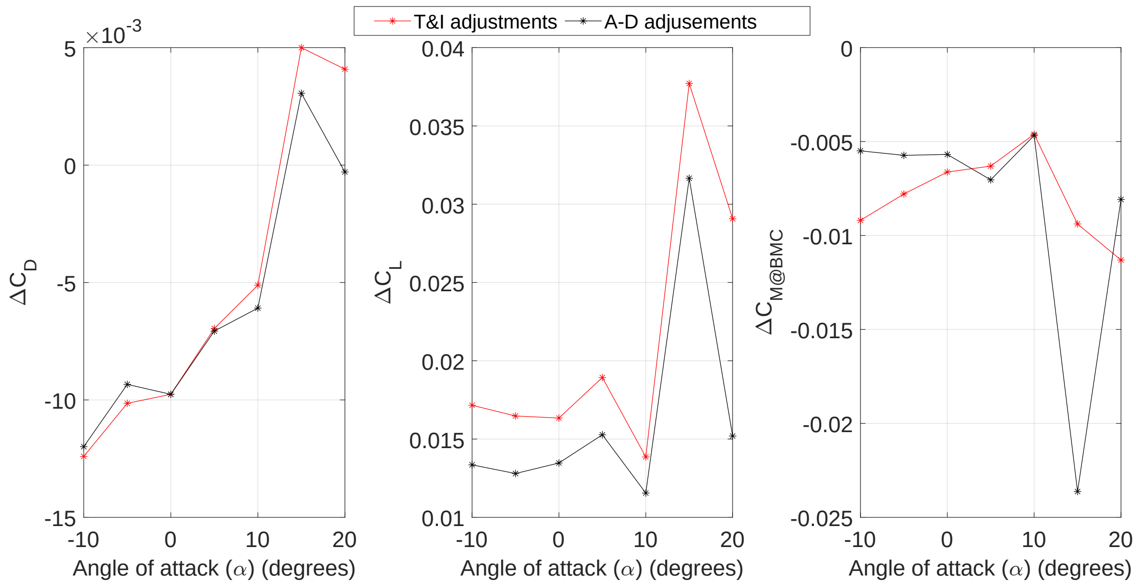

Figure 6.7: Difference in the magnitude of the adjustments for the W15 wing for both the T&I method and directly subtracting the two with the SST model.

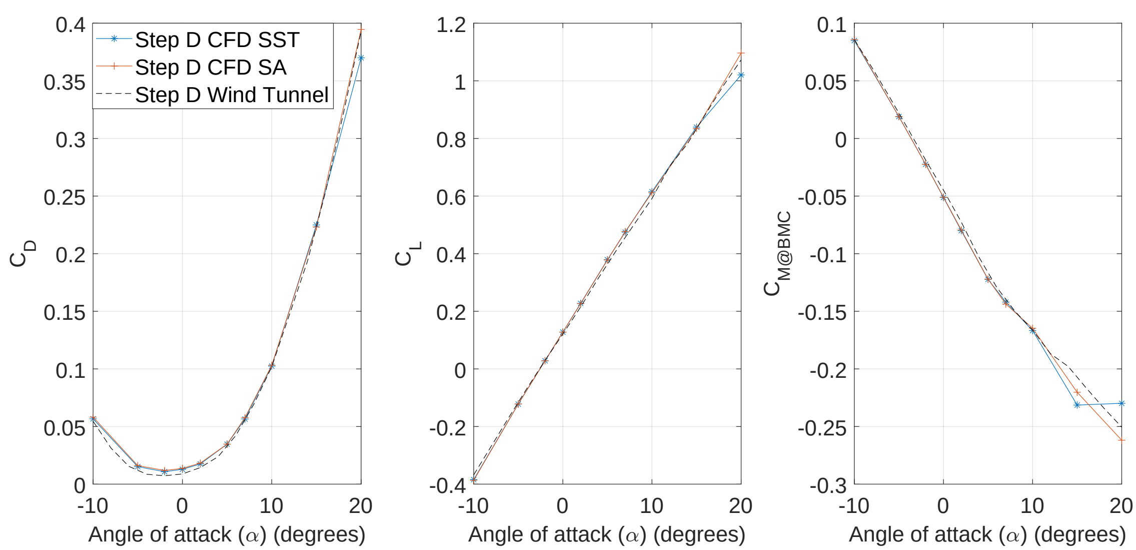

Figure 6.8: Comparison of the wind tunnel data with the effects of the model support system removed and the CFD simulations of the "Step D" configuration of the W15 wing with both SA and SST turbulence models

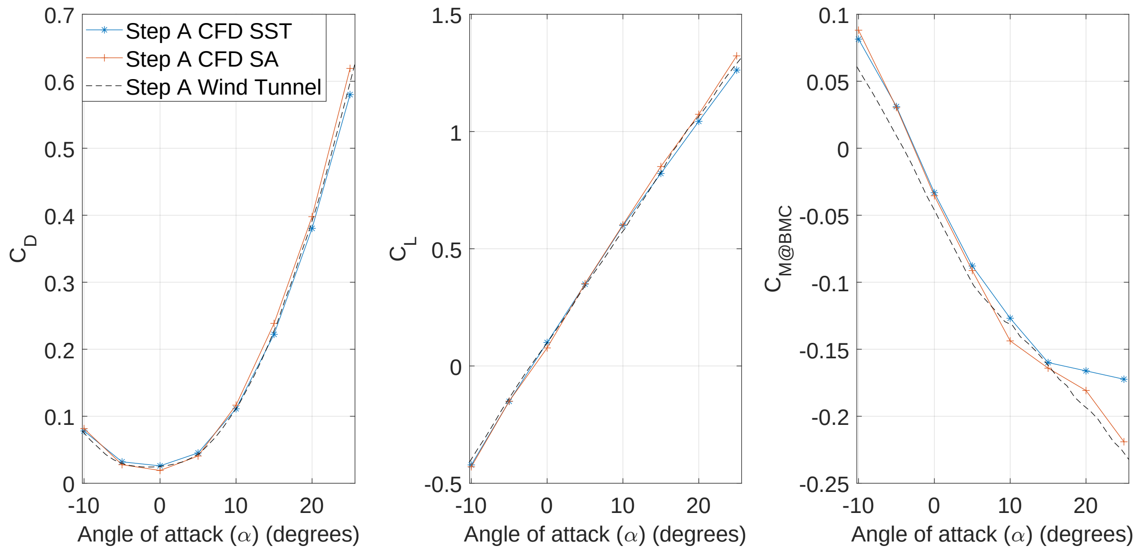

Figure 6.9: Comparison of the CFD results with the SA turbulence model (blue, star), the SST turbulence model (red, plus) and the wind tunnel data (black, dashed) for "Step A" for an α sweep for the UWS21A configuration

6.2 UW21A Longitudinal Sweep

Comparing the CFD simulation using the SA and SST turbulence of the AOA sweep at $\beta = 0°$, to the wind tunnel data for the UWS21A configuration against the 3 steps of the T&I process tested in the wind tunnel is shown in the following three Figs: 6.9, 6.10, and 6.11.

For "Step A", both models capture the drag behavior quite closely, while the SA model over predicts lift at 20° α, while the SST model matches the wind tunnel results quite well. For pitching moment, up to 15° α, both the SA and SST models produce similar results with mostly parallel behavior with an offset in the zero lift pitching moment, however at an α greater than 15°, both have results that change the overall behavior and disagree with the wind tunnel results. The SA model matches slightly better due to not having the change in slope until past 20° α, however the overall behavior at the high angle of attack deviates from the wind tunnel results to a fair degree.

For "Step B" and "Step C", there are some more unique behaviors present for the SST turbulence model. "Step B" has a lower simulated lift for the SA turbulence model at 20° α, while the 25° α

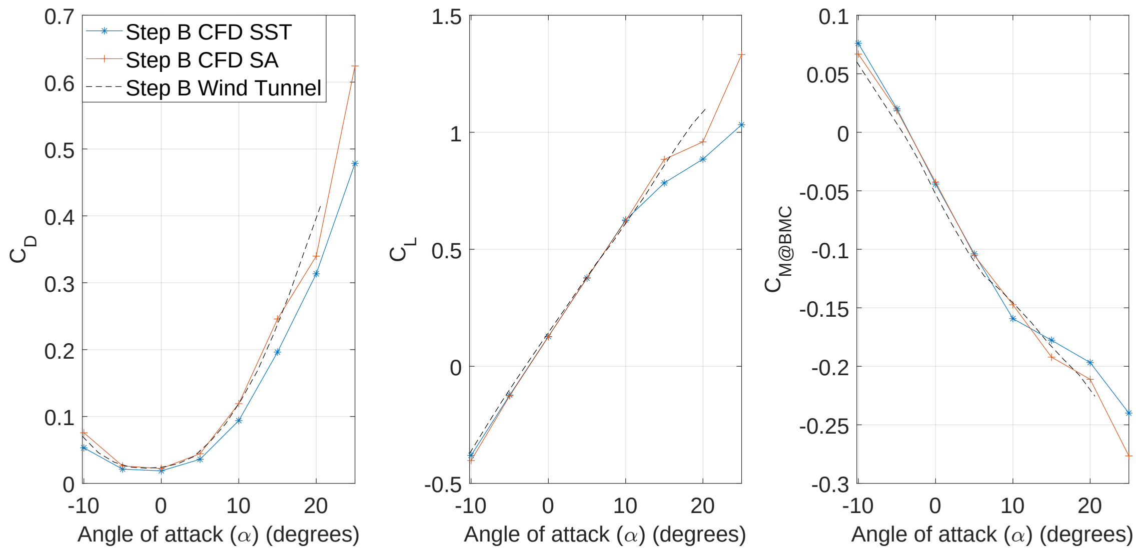

Figure 6.10: Comparison of the CFD results with the SA turbulence model (blue, star), the SST turbulence model (red, plus) and the wind tunnel data (black, dashed) for "Step B" for an α sweep for the UWS21A configuration

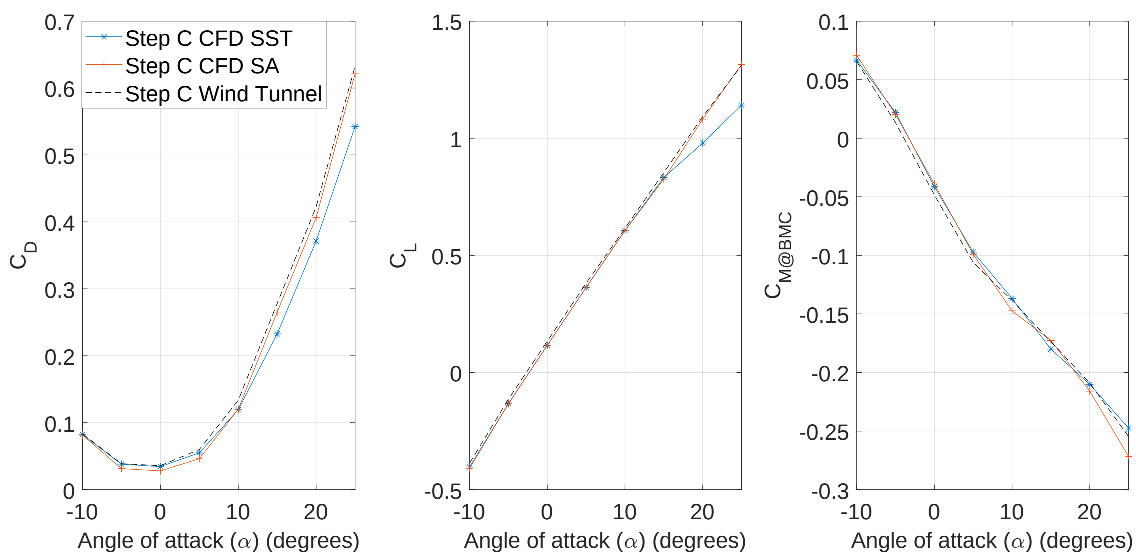

Figure 6.11: Comparison of the CFD results with the SA turbulence model (blue, star), the SST turbulence model (red, plus) and the wind tunnel data (black, dashed) for "Step C" for an α sweep for the UWS21A configuration

is around where the wind tunnel data would extrapolate to. For the SST turbulence model both "Step B" and "Step C", predict lower lift than what the wind tunnel results show This also leads to lower drag at higher angles of attack as well. Notably these results did occur in the mesh density study for "Step A", where the fine model was rejected due to diverging from the wind tunnel results. However "Step B" and C were both meshed with the same settings as "Step A", so the results should be consistent for the SST turbulence model. However, this loss in lift will appear later in the CFD simulation results for "Step D" for the SST turbulence model. For the SA turbulence model, "Step D" has a straight lift slope. For the pitching moment, the results match even closer than "Step A", where for low angles of attack the CFD results match quite accurately, with only deviations occurring at high AOA for "Step B", and an over-prediction for pitching moment for the SA turbulence model. Both results will be shown, as the SA turbulence model is slightly better at matching the wind tunnel results, across all 3 steps, however both models seem to perform better for the "Step B" and "Step C" cases in pitching moment, the hardest out of the three to simulate.

6.2.1 Comparisons of the Simulated T&I Process and the "Step D"

Processing the CFD simulations through the T&I process of A+B-C for the UWS21A and comparing against "Step D" simulation was done for both the AOA sweep and the sideslip sweep. The T&I corrections for the angle of attack sweep is shown in Figure 6.12 for the SA turbulence model and in Figure 6.13 for the SST turbulence model. The simulated T&I process are then compared against "Step D" which is the simulated end result where the model mounting system has been replaced and the forces and moments summed from "Step A" of the wind tunnel model alone (without adding in the forces on the fork which would be collected by the balance).

For the UWS21A model, the SA turbulence model produces slightly better results due to the better agreement between the T&I and "Step D" results at high AOA, with only the odd point from 20° α "Step B" changing the results. The SST model has the T&I method over-predict the lift from "Step D". However for the SST model, there was far better agreement at low angles off attack for lift and pitching moment than the SA turbulence model. Noting that "Step D" simulations in the SST turbulence model show the similar loss in lift that the "Step B" and "Step C" showed in the wind tunnel comparisons above, the T&I method allows for the correction based on the CFD results, that

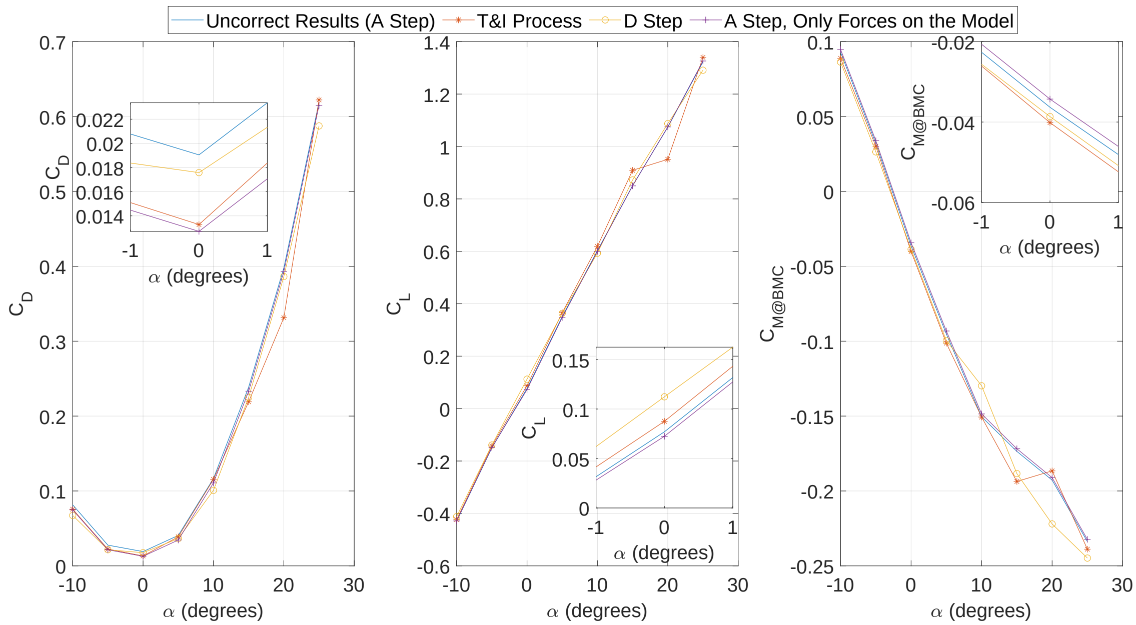

Figure 6.12: Comparison of the 3 different corrections to the uncorrected “Step A” simulation for the UWS21A model all simulated with the SA turbulence model

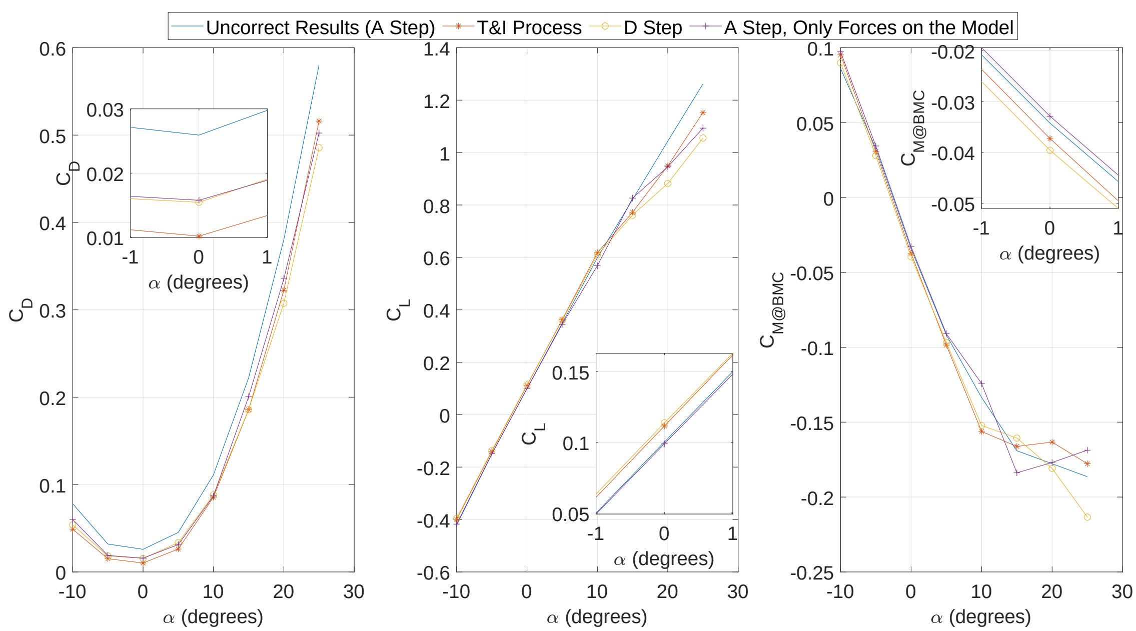

Figure 6.13: Comparison of the 3 different corrections to the uncorrected “Step A” simulation for the UWS21A model all simulated with the SST turbulence model

should be able to be extrapolated to the wind tunnel results where the loss in lift was not present. Additionally for pitching moment, the “Step D” and T&I results with the SST turbulence model disagree while the SA results match far closer. Regardless of turbulence model the T&I method best matches the simulated “Step D” results where the translations for lift and pitching moment are both accounted for. Looking at only the forces and moments applied on the model, while the drag matches at low angles of attack, the influence of the fork still causes the drag to be over-predicted at higher angles of attack, alongside the loss of lift seen in the CFD-simulated result. Additionally the T&I method shows the change in slope that “Step D” see at $10° \leq \alpha \leq 20°$ which would not have been predicted from any of the pitching moment curves from “Step A”, “Step B” or “Step C”. The deviations in the SST turbulence model results at $20° - 25°$ α are probably from the “Step A” deviation where the SST turbulence model predicted a flattening of the pitching moment curve that wasn’t present in the “Step B” and “Step C” conditions. The T&I method better represents the changes that the simulation of the model on the support system, but only simulating the forces on the model, and better matching the “Step D” simulation that had noticeable changes in lift and pitching moment.

6.2.2 Correction Magnitude Comparison

For the UWS21A α sweep with the optimal SA turbulence model the magnitude of the corrections is shown in Figure 6.14, the closeness of the correction is maintained for drag and lift for the range of $-10° \leq \alpha \leq 10°$, and only deviates when higher angles of attack are reached. Additionally pitching moment sees some deviations at $-10°$ and $-5°$ α, but is a close match for the rest of the plot. The sharp changes in trends that the adjustment in pitching moment coefficient shows is matched by both for $10°$ α, but does deviated at higher angles of attack, where the simulations did diverge from the wind tunnel results more substantially. The magnitude of the corrections for the SST turbulence model are shown in Figure 6.15 where the corrections are of a slightly greater magnitude, but for the low angle of attack region, the magnitudes of the T&I adjustments and the A-D adjustments are far closer than the SA turbulence model with more clear trends being present for the corrections. Additionally, the behavior of the pitching moment curve’s adjustment magnitude is consistent with similar ups increases and decreases between the two different correction

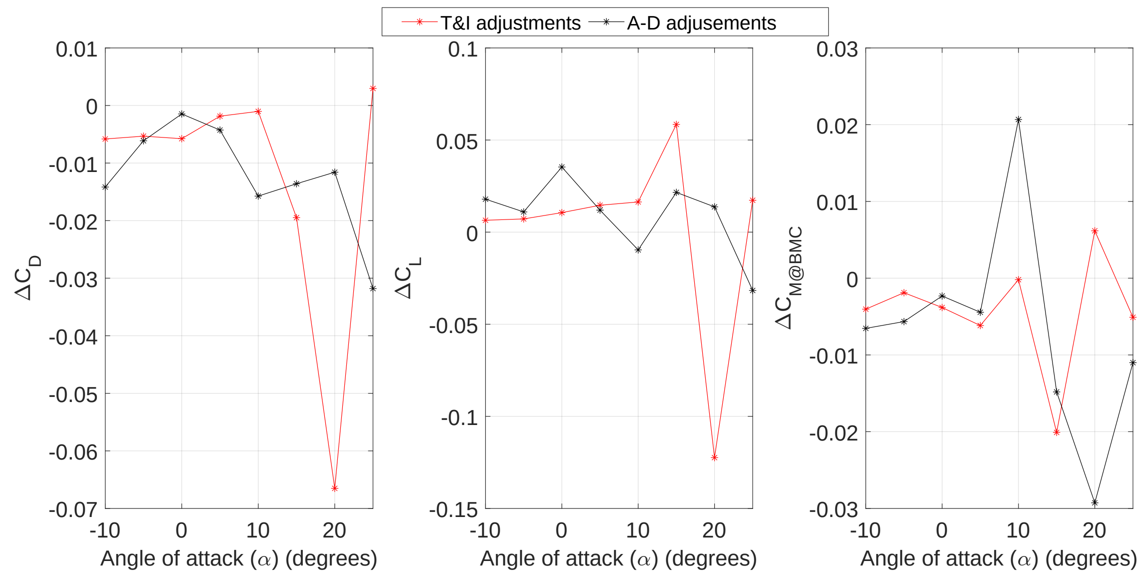

Figure 6.14: Difference in magnitude for the corrections of a UWS21A α sweep for the SA turbulence model.

processes, only differing at high angles of attack. Comparing the two different configurations trends for the same α sweep provided significantly different trends and behavior between the two. This demonstrates quite clearly that every model has a different set of T&I corrections, at least for a wing to a full configuration comparison. This implies that it is unlikely for a generic set of T&I corrections can be used for any model can be made accurately, necessitating either a set of generic tares for specific types of aircraft, or specific T&I testing done for every wind tunnel test.

For a final comparison between the CFD "Step D" results and the wind tunnel data, the wind tunnel results with the T&I process applied are shown in Figure 6.16 and compared with the "Step D" simulation of the W15 wing. In the low angle of attack region $-10 \leq \alpha \leq 10$ both lift and drag match well with the wind tunnel results, however pitching moment curves slope both deviate significantly after 7° α, where the SA turbulence somewhat matches the slope of the wind tunnel results, but the SST turbulence model deviates even further displaying different behavior than the wind tunnel results. Additionally both turbulence models predict slightly less lift than the wind tunnel data at high angles of attack, with the SST model predicting far less than the SA model does. Drag is similarly impacted. For a full configuration, the T&I results hold up well for the low

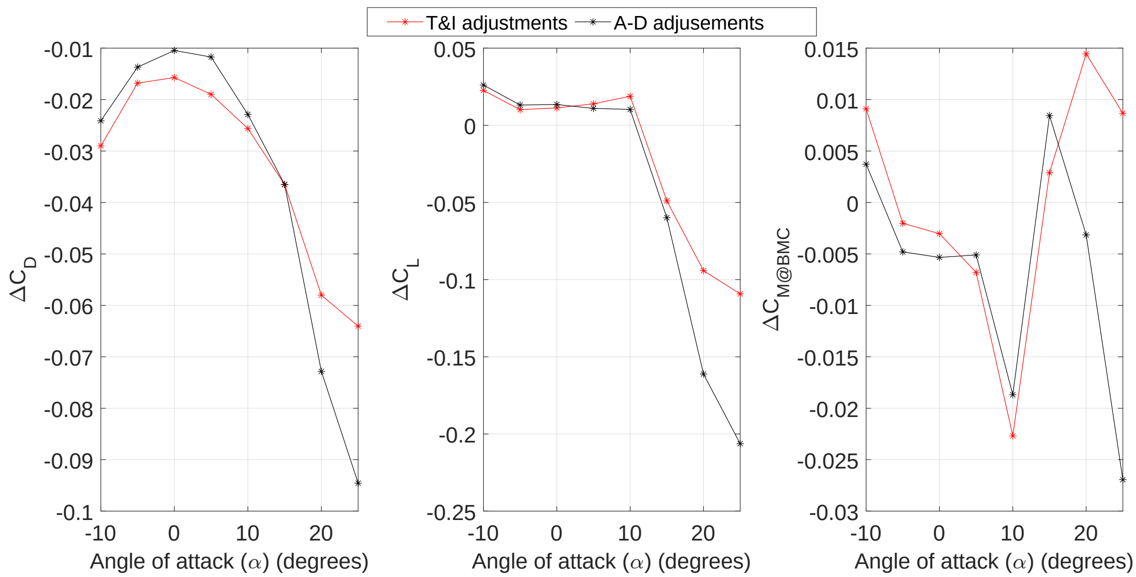

Figure 6.15: Difference in magnitude for the corrections of a UWS21A α sweep for the SST turbulence model.

angle of attack region, but higher grid refinement meshes and closer matching to the results from "Step A" are probably needed for high angle of attack behavior.

6.3 *UWS21A Sideslip Sweep*

6.3.1 *Wind Tunnel Data Validation*

The comparison of the simulation results using the SA and SST turbulence models against the wind tunnel results at a side-slip sweep of the UWS21A configuration at an α of 0° have the results for "Step A", "step B" and "Step C" shown in Figure 6.17, Figure 6.18, and Figure 6.19. Here, the smaller inaccuracies around $\alpha = 0$ are shown in greater detail, where the CFD simulations both under-predict lift and over predict pitching moment, by 0.005 and -0.02 respectively, matching with the results seen from the pitch sweep prior. "Step A" has the SST model match the wind tunnel results very closely with SA turbulence model being an under-prediction. However, both turbulence models suggest that there should be slight increase in drag at 0° side-slip which is not supported in the data. Additionally the change in lift from 0° side-slip to ±12° is under-predicted. For "Step A",

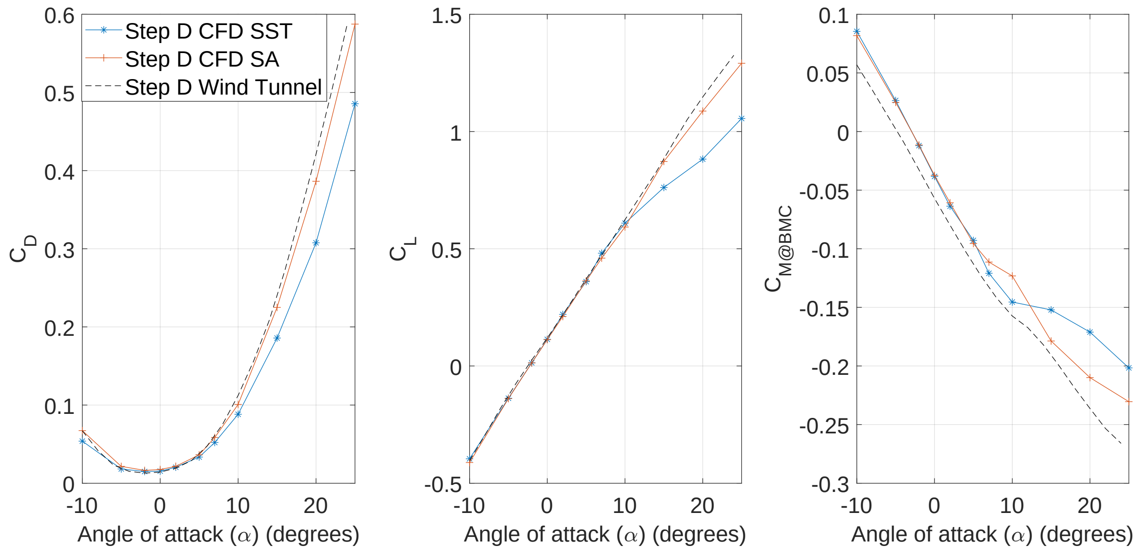

Figure 6.16: Comparison of the wind tunnel data adjusted with the effects of the model support system removed and the CFD simulations of "Step D" of the UWS21A with both SA and SST turbulence models

both yawing and rolling moment are predicted well, but side force simulations produce an s-bend in the results that is not present in the wind tunnel data.

For "Step B" and "Step C", there is similar behavior predicted, where the S-bends in side force both cause large deviations in behavior, while yawing and rolling moment both produce similar results, but simulations for "Step C" did not produce as large of an S-bend as "Step A" and "Step B" did causing a deviation. "Step B" has both turbulence models predict drag nearly matching the wind tunnel results with a slightly flatter curve, while drag was under-predicted for both in "Step C". "Step B"'s wind tunnel results produced unexpected behavior, which is somewhat matched in the simulation results asymmetry. For pitching moment, both "Step B" and "Step C" had similar results to "Step A", with similar offset, but curvature matched somewhat closer. Turbulence models didn't change the results significantly between the simulations, however for the lateral force and moments, the SST model matched slightly better.

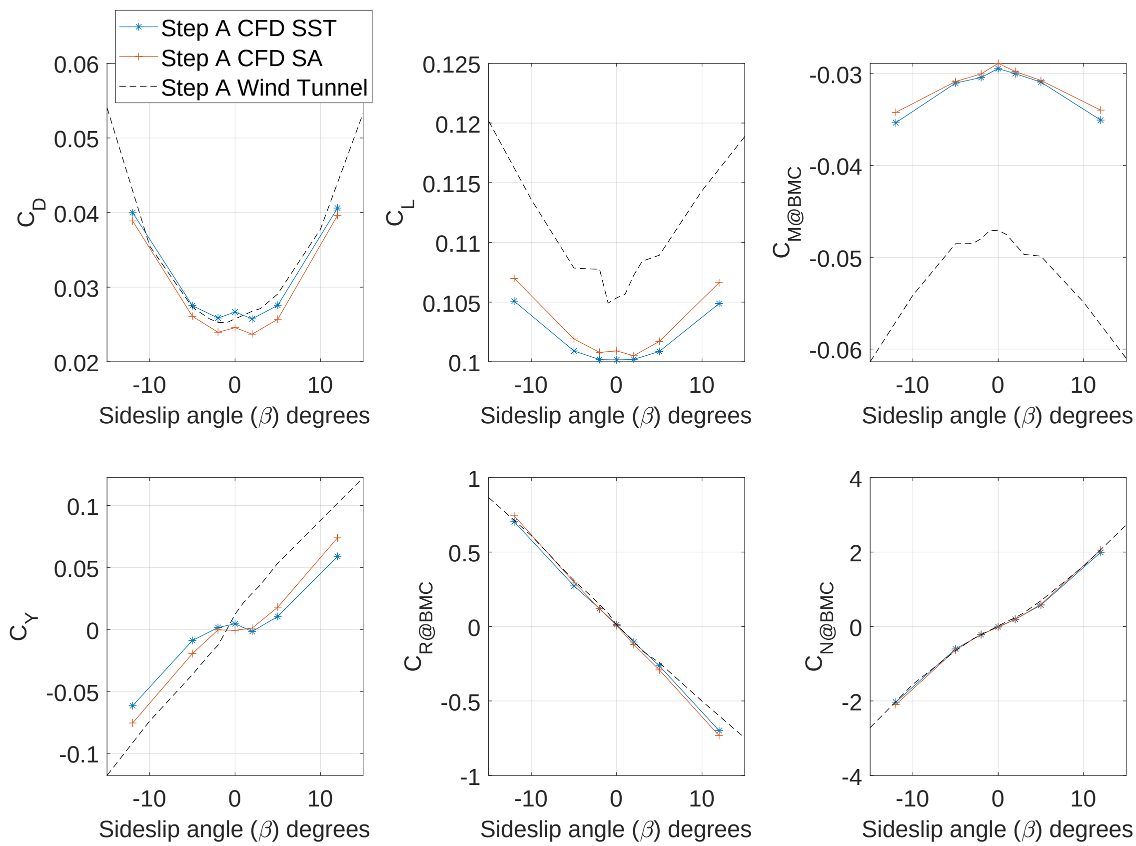

Figure 6.17: Comparison of the CFD results with the SST turbulence model (blue, star), the SA turbulence model (red, plus) and the wind tunnel data (black, dashed) for “Step A” for a β sweep at $\alpha = 0°$ for the UWS21A configuration.

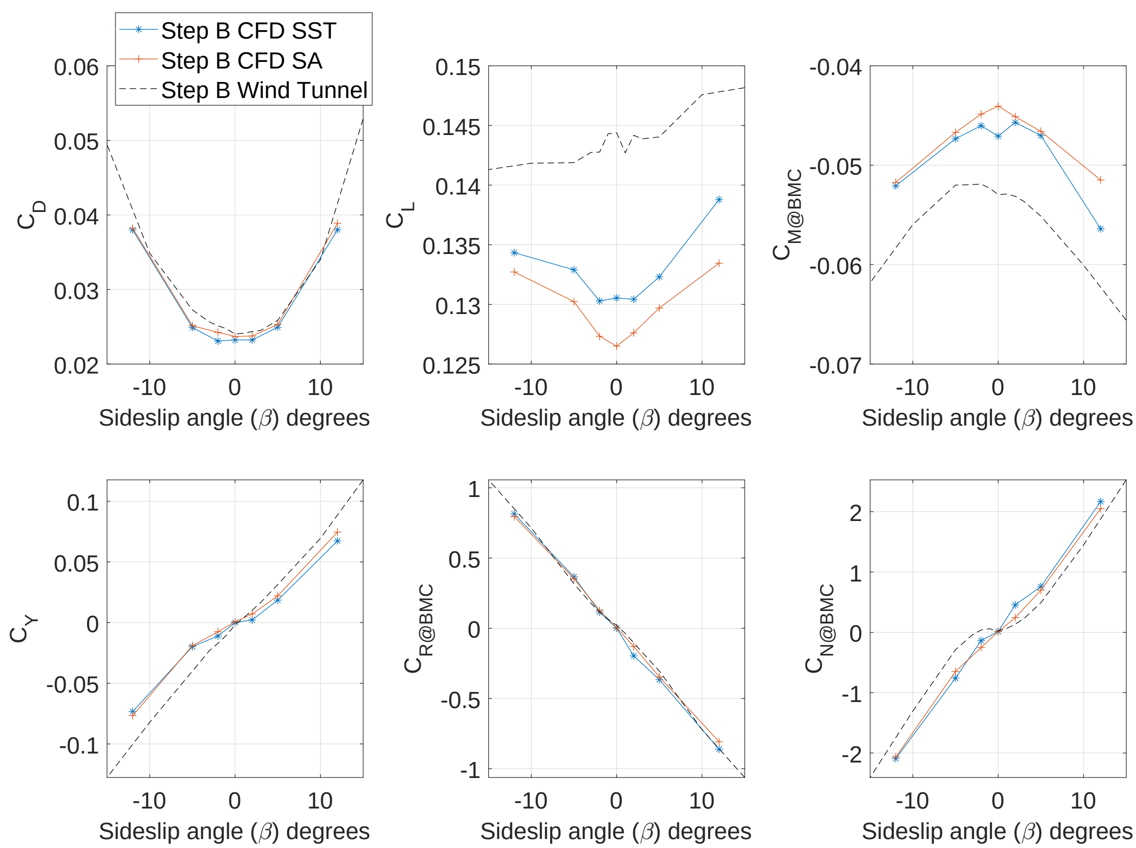

Figure 6.18: Comparison of the CFD results with the SST turbulence model (blue, star), the SA turbulence model (red, plus) and the wind tunnel data (black, dashed) for "Step B" for a β sweep at $\alpha = 0°$ for the UWS21A configuration.

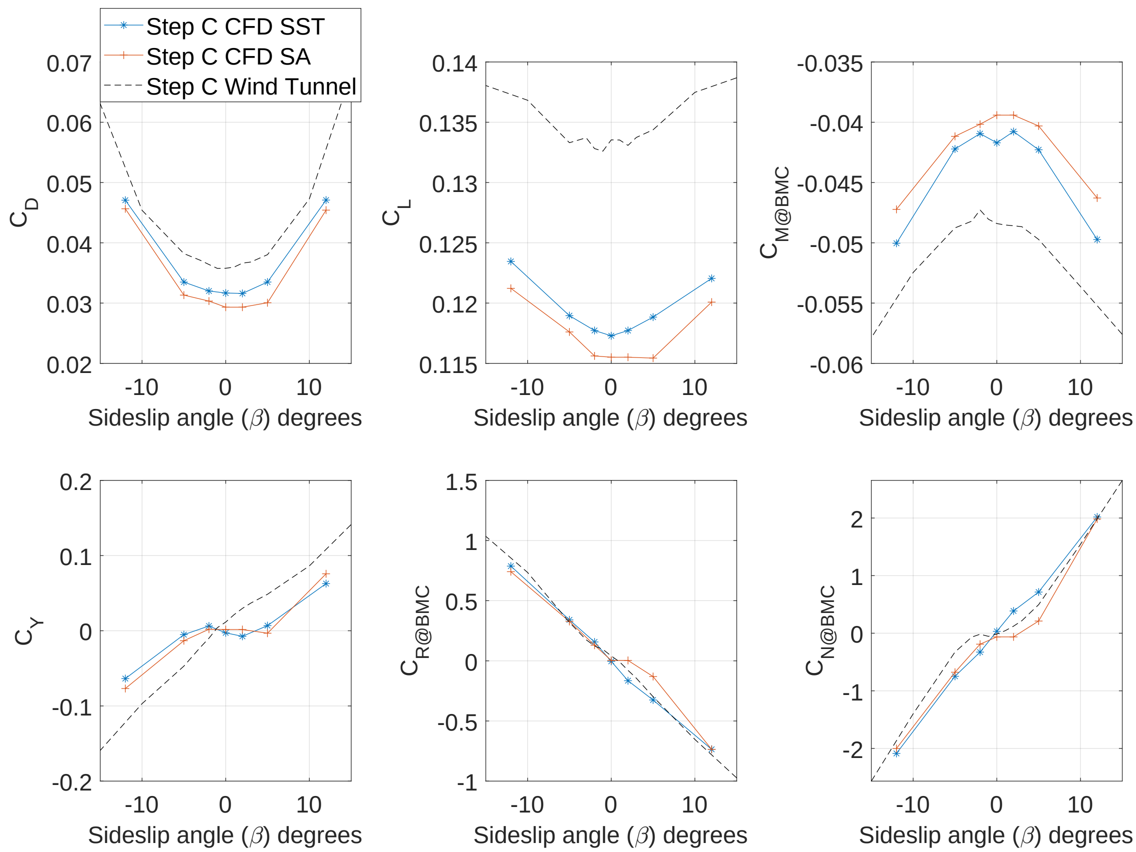

Figure 6.19: Comparison of the CFD results with the SST turbulence model (blue, star), the SA turbulence model (red, plus) and the wind tunnel data (black, dashed) for "Step C" for a β sweep at $\alpha = 0°$ for the UWS21A configuration.

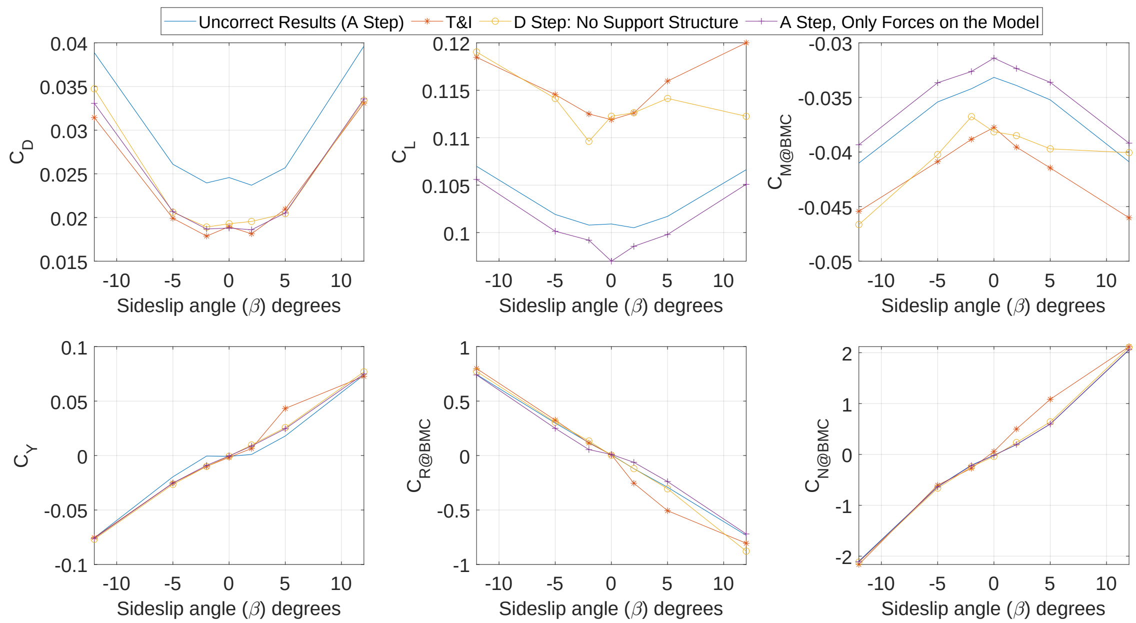

Figure 6.20: Comparison of the 4 different corrections to the uncorrected "Step A" simulation for the UWS21A model using the SA turbulence Model

6.3.2 Comparisons of the Simulated T&I Process and the "Step D"

For the lateral forces and moments, the T&I method does match quite closely, where the s-bend that was presented in the original "Step A" is gone in the T&I process and in "Step D". The results for the SA turbulence model are shown in Figure 6.20 and for the SST turbulence model in Figure 6.21. The forces only on the model respect this as well, but match a bit closer, where at $\pm 2° \ \beta$ there are bit off for the SST model, while the $5° \ \beta$ is off for the SA turbulence model. For negative side slip angles, the SA turbulence T&I method matches the "Step D" results well, but not so for positive side slip angles. Roll and yaw are similarly matched well for negative sideslip for the SA turbulence model, and are smoothed and have the results match closely. For the sideslip case, the SST turbulence model performs a bit better than the SA, but additional sideslip angles at different AOA is required for further validation, especially once presence of the fork's effects become more present at higher angles of attack.

Overall, when the T&I adjustment is compared to "Step D", with the support system removed,

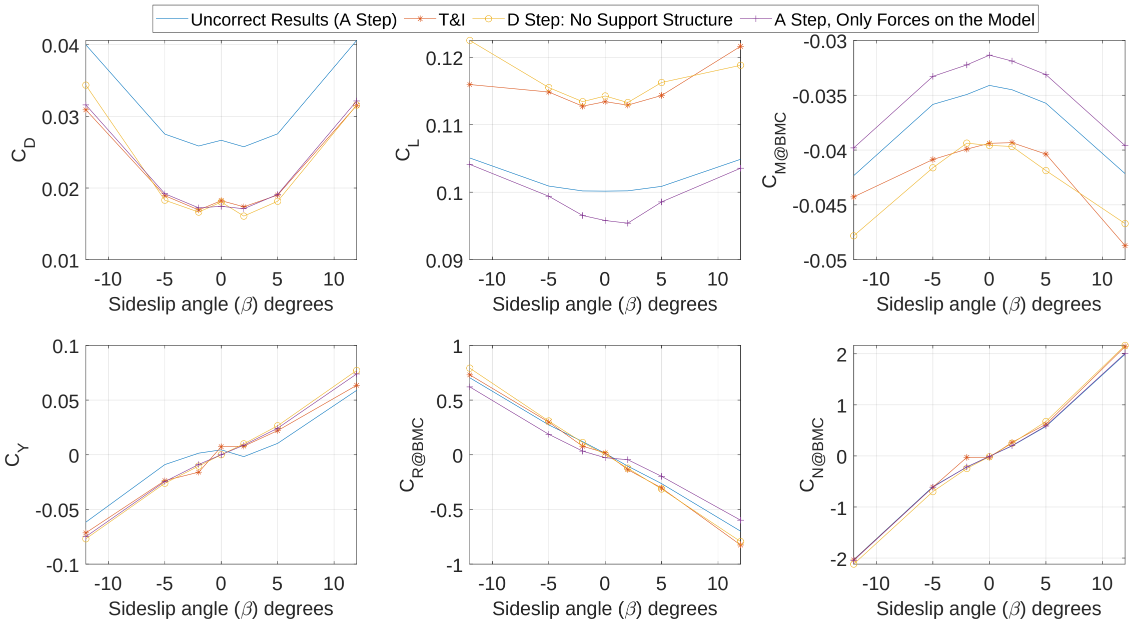

Figure 6.21: Comparison of the 4 different corrections to the uncorrected "Step A" simulation for the UWS21A model using the SST turbulence Model

the T&I method performed the best, especially for the variations in angle of attack. The sideslip sweep produced less accurate results, however, the T&I method would perform better at higher angles of attack, where the larger extremes in pressure gradient have the pressure gradient are impacted more by the presence of the fork.

6.3.3 Correction Magnitude Comparison

For the UWS21A β sweep the tare and interference corrections generated from the SA and SST turbulence models from both the T&I process and the direct A to D tare are presented in Figure 6.22 for the SA turbulence model and in Figure 6.23 for the SST turbulence model. Overall, the adjustments are nominally within the same magnitude, but do not appear as distortions or translations of the other trends for the most part. Additionally, while the adjustments from "Step D" provided greater changes in values for the α sweeps, for the β sweep, the T&I method provided plots with a greater spread and sharper changes for the lateral coefficients. The SST model generally predicts larger corrections than the SA turbulence model, with the SST turbulence model plots being

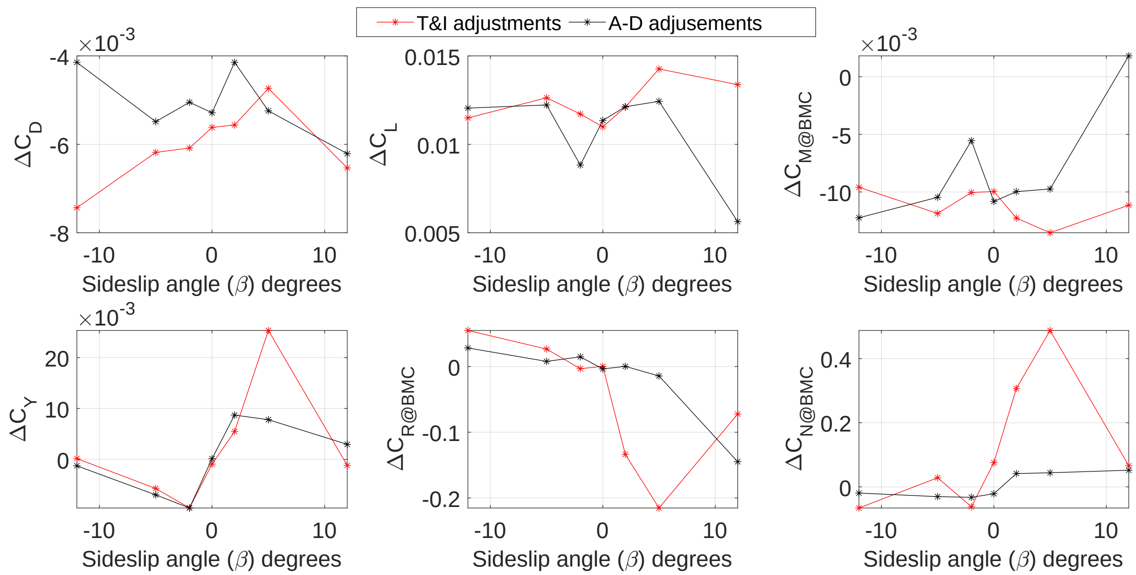

Figure 6.22: Difference in magnitude for the corrections of a UWS21A β sweep with the SA Model

more smooth for the lateral force and moments than the SA turbulence models. For the longitudinal changes were both quite erratic as well. None of the plots are very symmetric, which does match the behavior for the lateral corrections shown in [20] which had a significant amount of asymmetry as well, most likely due to asymmetries in the mounting arms and some flexibility in the support structure due to the large model.

These flexibilities and asymmetric behavior can come from the fork twisting or asymmetric flow detachment and reattachment from the single direction yaw sweeps.

6.4 UWS20A

The full T&I process was not simulated for the UWS20A configuration, where it primarily used as another configuration to compare for the wall corrections process. “Step A” and “Step D” were both simulated so a tare and interference tare can still be applied. These two sets of simulations allow for a comparison of the wind tunnel generated T&I corrections to the corrections generated from a CFD correction generated from the difference between “Step D” and “Step A”.

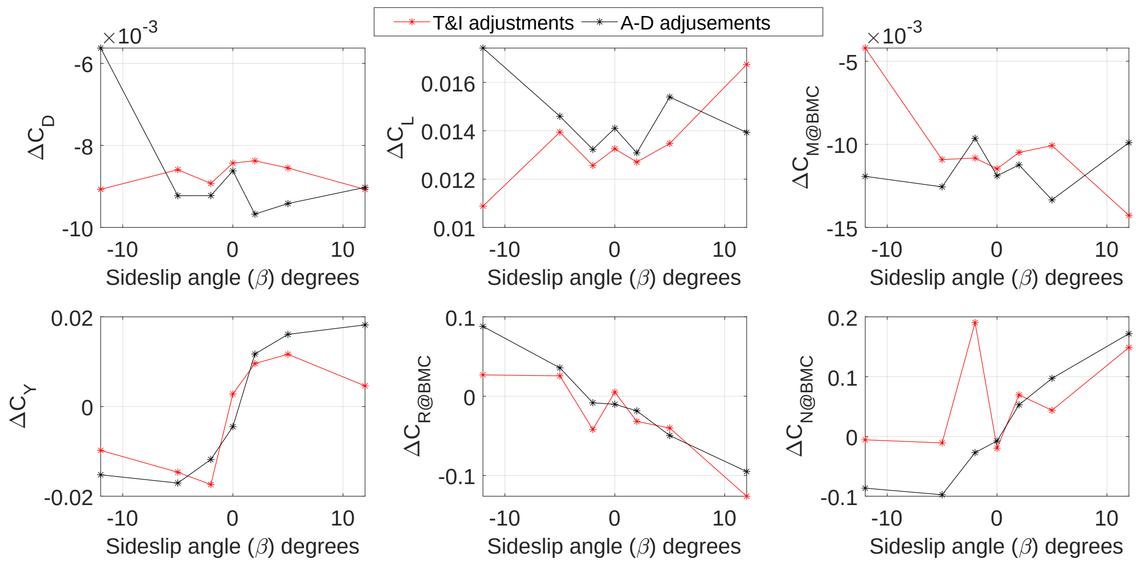

Figure 6.23: Difference in magnitude for the corrections of a UWS21A β sweep with the SST Model.

6.4.1 Wind Tunnel Data Validation

For the A step, the results of simulations with both the SA and SST turbulence models were compared against the wind tunnel results. This comparison is shown in Figure 6.25. Notably the higher angles of attack for the UWS20A are simulated worse than the UWS21A configurations. Specifically noting the large divergence in results between the two turbulence solvers at an $\alpha = 15°$, which is due to the wake of the canards directly intersecting the tails at that angle of attack causing a large variation in behavior between the two different solvers. Interestingly, the SST model which generally predicted less lift than the wind tunnel results in the prior simulations instead over-predicted the lift of the model. However both turbulence models seem to converge to similar results at $\alpha = 20°, 25°$ with a slight offset in C_{M0}. The other largest deviation is a change in $C_{M\alpha}$ where the wind tunnel has smaller $C_{M\alpha}$ than the simulated results.

"Step D" takes many of the differences between the wind tunnel and CFD results of "Step A" and generally amplifies them, as there is a notable change in $C_{L\alpha}$, which corresponds the differences seen in the drag polar. For the pitching moment curve, the differences between the wind tunnel and CFD results still generally apply with a slightly different slope in the linear region, and the

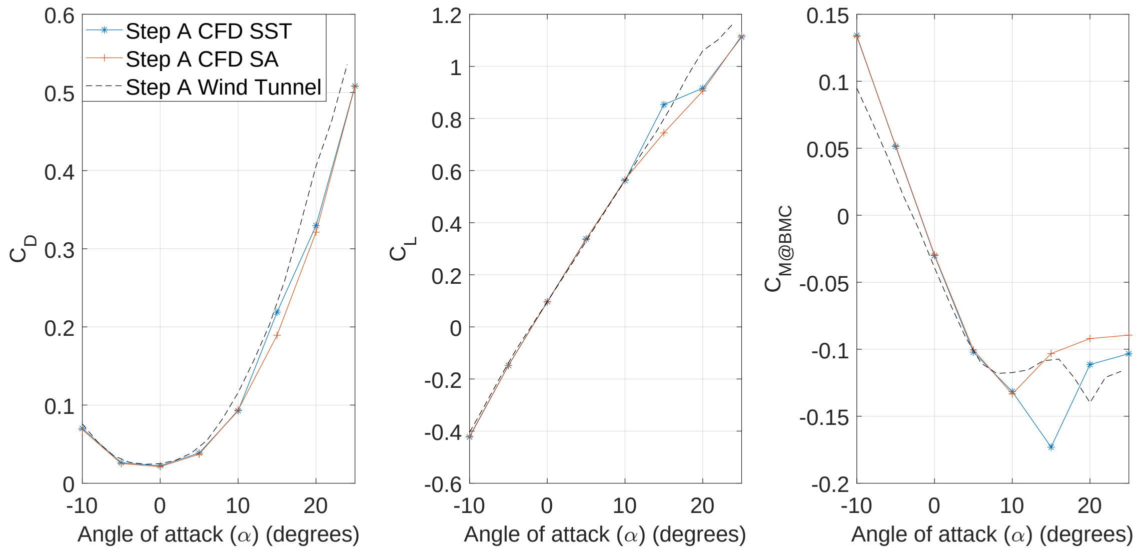

Figure 6.24: Comparison of the CFD results with the SA turbulence model (blue, star), the SST turbulence model (red, plus) and the wind tunnel data (black, dashed) for "Step A" for an α sweep for the UW-S-20A configuration

magnitude of the pitch break agrees well. Additional notes are that there is is a large difference at $\alpha = 15°$ due to the similar canard tail interference noted above. Both of the "Step A" and "Step D" CFD simulation results do behave similarly suggesting that results should be comparable to each other and capable of generating a model support system tare.

6.4.2 Single Step CFD Correction

It is more important to note as above that the T&I corrections applied to the wind tunnel results here are from the UWS21A applied to the UWS20A configuration, where is not necessarily expected that the tare generated from the T&I method would match closely with the specific CFD result generated here. The model support system corrections are shown in Figure 6.26 for the SA turbulence model and in Figure 6.27 for the SST turbulence model for the single step CFD result and the correction applied by the wind tunnel. Noting that above for most of the comparisons, the lift and drag curves were of similar values, except for the pitching moment curve which generally produced a substantially larger difference with a notable slope that's not present in the CFD data. The SA

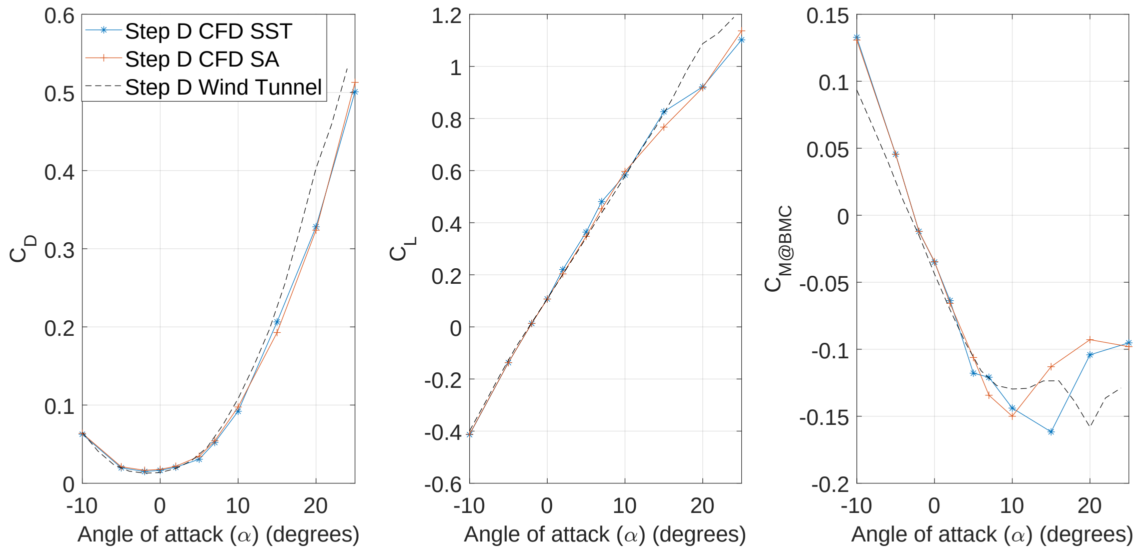

Figure 6.25: Comparison of the CFD results with the SA turbulence model (blue, star), the SST turbulence model (red, plus) and the wind tunnel data (black, dashed) for "Step D" for an α sweep for the UW-S-20A configuration

turbulence model produced slightly more consistent trends, even if the wind tunnel data has similar unusual behavior. Both turbulence models suggest that the actual tare and interference corrections are smaller in magnitude in drag for the UWS20A configuration over the UWS21A configuration, and that the lift changes are more equivalent to a change in C_{L0}, which is supported by the prior results from the behavior of the UWS21A as well. There is relatively close agreement between the two suggesting that the T&I data can be applied to similar general aircraft configurations, but more fine tuned corrections should be generated on configuration by configuration basis rather than just using the differentiators of a wing, wing+aft deck, and a wing/fuselage combination, depending on the required accuracy of the final wind tunnel results.

6.5 Summary

The T&I method produces a set of corrections that match the changes predicted from the model in the test section without the model support system. Taking only the forces and moments on the model in CFD does not fully capture the effects of the model support system, as without the support

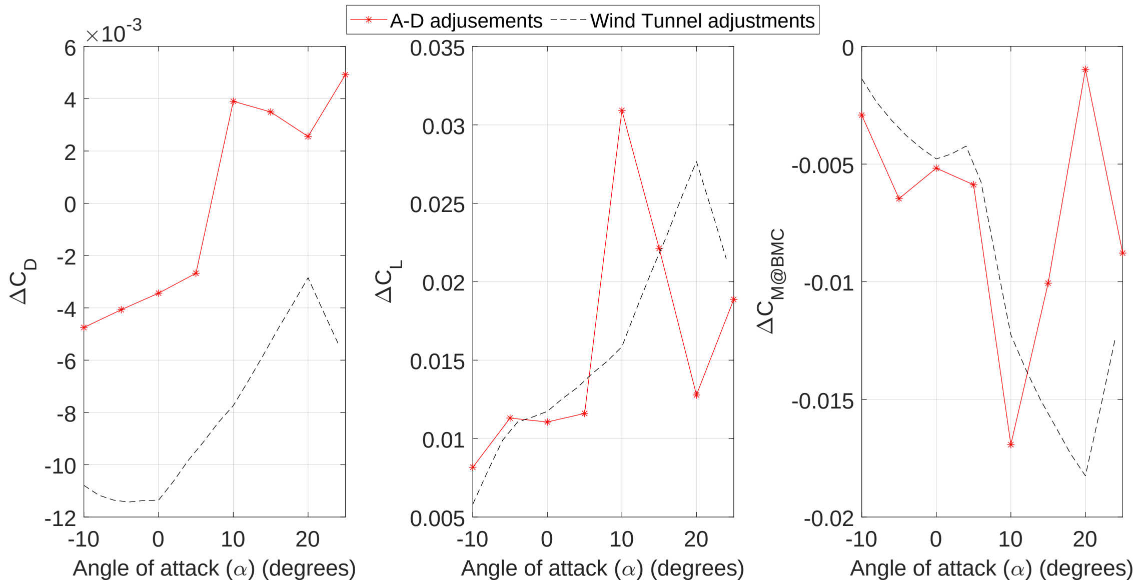

Figure 6.26: Difference of the single step CFD correction with SA turbulence model (red) and the wind tunnel applied correction (dashed black) for the UWS20A configuration

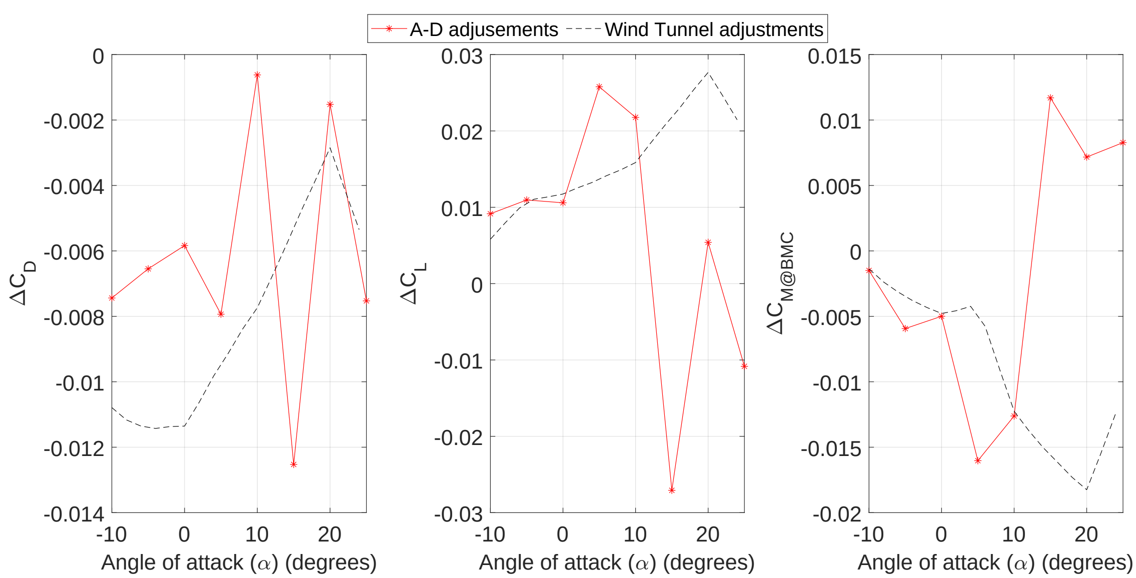

Figure 6.27: Difference of the single step CFD correction with SST turbulence model (red) and the wind tunnel applied correction (dashed black) for the UWS20A configuration

system, the model generally sees an increase in lift, a loss in drag, and an additional pitching moment offset. These effects would not be tracked with a simple fork tare, where the strut is run in the wind tunnel without the model. The model support system requires a more complex correction to remove the effects of the support system on the flow field around the model, which both the T&I correction testing provides, alongside the more inexpensive A-D CFD fork tare, which is recommended in the future for further tests.

There was not a preferred best turbulence model between the two different models, with the W15 favoring the SST model for best results and the UWS21A model favoring the SA turbulence model. However, variations between the two turbulence models are minor and both produce mostly accurate results with the primary variations in the final results being at high angles of attack, where RANS turbulence models generally break down due to large scale vortices.

For future testing, T&I is recommended to be done for a larger variety of configurations, but more CFD simulations can be used to determine what are the key changes to require new T&I configurations, as the UWS20A has a different outboard wing and a different horizontal stabilator height and different vertical tail than the UWS21A. It would be presumed that these errors may be magnified even more for side-slip sweeps as well.

Chapter 7
WALL CORRECTIONS

The wall and blockage corrections represent removing the effects of the walls of the tunnel on the model. For standard wind tunnel corrections, the blockage and wall effects are calculated separately, as the blockage corrections are for the fact that the air moving around the model will see a smaller cross-section inside the wind tunnel causing the velocity of the air to accelerate in the plane of the model, regardless of the changes in velocity around the model itself. The wall effects are a combination of the walls of the tunnel providing different boundary conditions on the flow, changing the overall flow field and the wake of the model being deflected by the presence of the floor/ceiling of the tunnel which changes the forces and moments on the model. For generating CFD based corrections, the wall and blockage effects are combined due to the corrections being generated from taking the difference between "Step D" from the T&I results and the free air simulation results. This section will detail the corrections that the KWT supplied to the wind tunnel model and the results from the CFD corrections are compared with a new set of wall correction constants over the ones theoretically calculated.

7.1 Shindo's Wall and Blockage Correction

For the KWT's data reduction process, the wall and blockage corrections are two separate corrections, with the most commonly used version of the being the one used by Shindo. There is an alterative set of blockage corrections that use a set of geometry calculations to determine the theoretical blockage corrections, while Shindo's blockage corrections use the corrected lift and drag values to determine the blockage effect of the aircraft. The KWT primarily uses Shindo's wall effects due to them using the uncorrected lift and drag data of the model, rather than a set of geometric approximations, which works better for model specific configurations.

7.1.1 Blockage Correction

The KWT implementation of Shindo's blockage correction involves calculating an adjusted dynamic pressure q_C to adjust the q_A that the tunnel measures. The actual dynamic pressure q_A is measured directly from a set of dynamic pressure strips at the start and end of the bellmouth which gets corrected by a q_A/q_I value to account for the area ratio. To compute q_C a blockage correction adjustment ϵ is used. The blockage correction adjustment ϵ is defined in Eq. 7.1, where the correction to q_A to get q_C is written in Eq. 7.2.

$$\epsilon = \frac{S_w}{C_A}\left[C_{D_u} - C_{L_u}^2\left(\frac{1}{\pi AR} - \delta_w \frac{S_w}{C_A}\right)\right] \tag{7.1}$$

$$q_c = q_a(1+\epsilon)^2 \tag{7.2}$$

The coefficients with subscript u are the coefficients calculated using q_a rather than the q_c. S_w is the wing reference area and AR is the aspect ratio of the wing. C_A is the actual test section area 91.4 ft^2 for the KWT. The parameter δ_w is a wall correction constant who's determination is detailed in the NACA report 547, but for all SCALOS configurations, was taken to be around 0.114 ± 0.0005. There are specific calculations detailed in NACA report 547 which are implemented by the KWT, however the actual variation in the parameter is so minor that it doesn't effect the results much. This wall correction constant is generated using an infinite set of image vortices around the walls of the rectangular test section. These image vortices come about to enforce a wall boundary condition at the locations of the walls, which matches the behavior of the flow in the tunnel, where the airfoil around the model is parallel to the walls of the tunnel (for potential flow, the walls are slipping so flow on a wall is parallel to the wall, not 0 for a no-slip wall.)

7.1.2 Wall Correction

For Shindo's wall corrections, the wall corrections get expressed as both an adjustment to the angle of attack, along with an adjustments to C_D and C_M. The adjustment to angle of attack is shown in Eq. 7.3. The variable C is the area of the test section without fillets, which is 96 ft^2.

$$\Delta a_{wc} = 57.3\delta_w \left(\frac{S_w}{C}\right) C_{L_W} \tag{7.3}$$

The KWT uses two different reference runs to apply the wall corrections. A lift set which is used for the C_{L_W} equation, which is a pitch sweep where the tail was removed from the model, isolating the effect of the wing's wake. The other set is a CMS set, which is a set of three different tail deflections where a derivative $\frac{\partial C_M}{\partial \delta_S}$ value can determined, which is used to correct C_M. The correction to C_D is shown in Eq. 7.4.

$$\Delta C_{D_{WC}} = 57.3 \Delta a_{wc} C_{L_W} \tag{7.4}$$

To correct the pitching moment coefficient Eq. 7.5, which is only applied if there is a tail on the model. Otherwise the $\frac{\partial C_M}{\partial \delta_S}$ is zero.

$$\Delta C_{M_{WC}} = -57.3 \delta_{A_S} \frac{\partial C_M}{\partial \delta_S} C_{L_W} \frac{S_W}{C} \tag{7.5}$$

These corrections are then applied with the following Eq. 7.6 which apply the rotations from the adjustments to the angles of attack and the shift to pitching moment curve.

$$\begin{aligned} C_{L_{WA}} &= \cos(\Delta a_{wc}) C_{L_{INI}} + \sin(\Delta a_{wc})(C_{D_{INI}} + \Delta C_{D_{WC}}) \\ C_{D_{WA}} &= \cos(\Delta a_{wc})(C_{D_{INI}} + \Delta C_{D_{WC}}) - \sin(\Delta a_{wc}) C_{L_{INI}} \\ C_{M_{WA}} &= C_{M_{INI}} + \Delta C_{M_{WC}} \end{aligned} \tag{7.6}$$

The parameter δ_{A_s} is the wall correction constant for an offset wing in the test section behind the main wing. It values ranges more than the prior constant δ_w where δ_{A_S}'s value is 0.0820 ± 0.0015. Either way both wake constants are mostly consistent for all of the wind tunnel runs for each configuration, despite being uniquely calculated by the wind tunnel for each angle of attack.

7.2 CFD Results

For each turbulence model, "Step D" and free air simulations were compared against the wind tunnel results, for both a magnitude of the corrections and the differences between the results with and without wall corrections applied. Note that for these simulations the reference point is at the 25% MAC reference point and not the BMC from the T&I section due to the wall corrections being occurring after the moment transfers have been applied.

7.2.1 W15

For the W15 wing on it's own, it has the closest match to the wind tunnel results as a whole, but still with some substantial differences. The wind tunnel and CFD results for the "Step D" and Free Air results (Pre-wall correction application and fully corrected data for the wind tunnel data) are plotted together for comparison in Figure 7.1 for the SA turbulence model and in Figure 7.2 for the SST turbulence model. Noting that the free air simulations for both the SA and SST turbulence models, in the free air configurations there is less lift predicted than the in “Step D” CFD simulation. However, based on the lack of a tail both pitching moment slopes do end up together with little differences. And the slight loss in $C_{L\alpha}$ from the Δa_{wc} matches from the predictions. However, in both cases the “Step D” result after having the moment transfer be applied to them produces some sharp changes that make “Step D” results less predictable. However, the differences between the free air and “Step D” are far larger than what the wind tunnel results predict. Additionally, it’s notable that the change in location of the pitch break location for C_M for the in tunnel cases matches with the wind tunnel results closer than the free air case to 10° AOA for the SST model, before having a point closer to the free air data at 15° AOA, before matching closely with the wind tunnel results at 20° AOA. The SA turbulence model produces CFD simulations somewhat matching the wind tunnel data, but the linear region of the pitching moment curve continues to 7° AOA before the pitch break point occurs at 10° AOA.

7.2.2 UWS21A

For the UWS21A case, the results for the wall correction is far more varied between the two turbulence models. The wind tunnel pre and post wall correction data is compared against the CFD simulated “Step D” and free air simulation in Figure 7.3 for the SA turbulence model and in Figure 7.4 for the SST turbulence model. For the SA turbulence model, there is far less of a variation in slope between “Step D” and the free air case. Both simulations predict less lift at higher angles of attack than the wind tunnel results, and as such distort the curvature of the C_D plot. With the free air case for the SA turbulence model has more lift predicted for the free air case than “Step D”, explaining why the free air drag case has greater drag at higher angles of attack. The most important result out of the lift and drag results is that for small angles of attack, the effects of the wall corrections seem to be minor for both the SA and SST turbulence models.

The largest wall effects on the model comes from the pitching moment curves, where there is a noticeable change in $C_{M\alpha}$, even if the results are a little more varied between the two turbulence models at higher angles of attack. For the SA turbulence model, ignoring an extraneous value for the

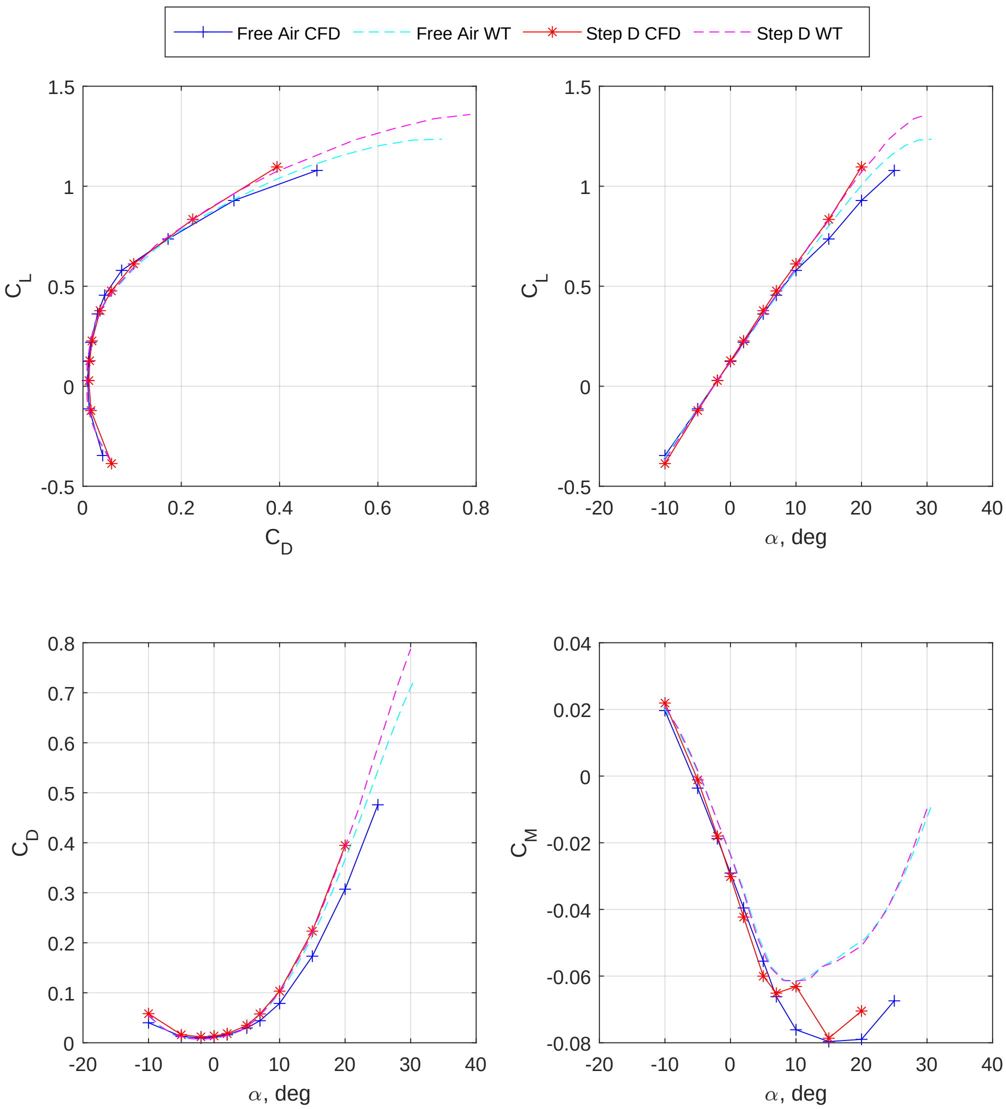

Figure 7.1: Comparison of the pre and post Wall corrections application for both the Wind Tunnel Results and the CFD with the SA turbulence model for the W15 wing

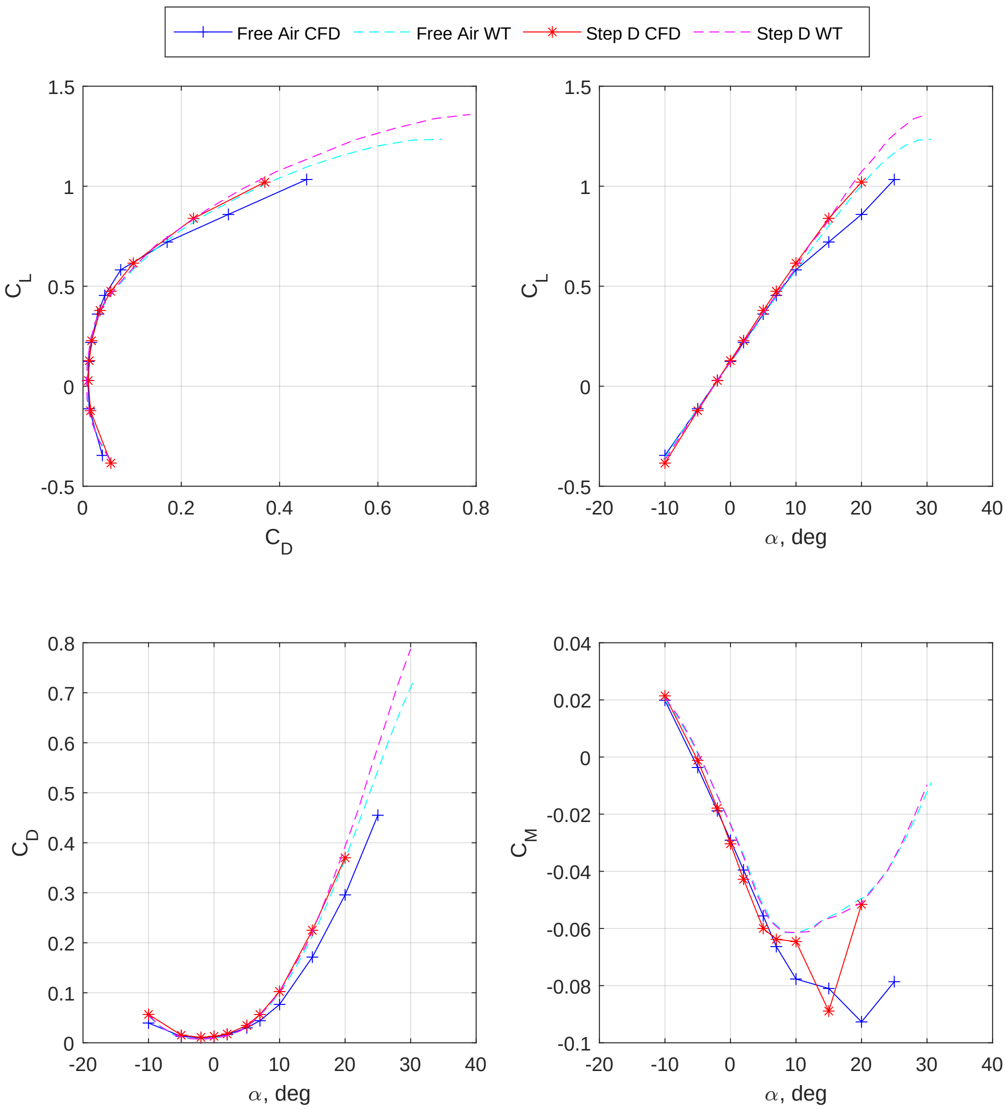

Figure 7.2: Comparison of the pre and post Wall corrections application for both the Wind Tunnel results and the CFD with the SST turbulence model for the W15 wing

wall effects at $\alpha = 10°$, there is a rotation of the C_M curve, consistent with the behavior expected for the wall corrections, however CFD predicts a far greater magnitude than what the wind tunnel results show. For the SST turbulence model, "Step D" predicts a pitch break at a higher angle of attack than the SA turbulence model and has contradictory behavior at higher angles of attack. However if looking at the low angle of attack region of the model, the slopes of the two pitching moment curves do follow the trends suggested by the wall corrections, but with a significantly increased δ_{A_S} variable than what was used by the KWT.

7.2.3 UWS20A

The T-Tail configuration UWS20A was specifically chosen for analyzing the effects of the wall corrections for a T-tail configuration. Comparisons between the CFD and wind tunnel results for the "Step D" and "Free Air" results are shown for the UWS20A model in Figure 7.5 for the SA turbulence model and in Figure 7.6 for the SST turbulence model. Additionally, the UWS20A configuration did not see a large change in C_{M0} as the UWS21A configuration, showing that the C_{M0} offset was due to the interactions of the low tail and the downwash from the wing. For the full configurations at high angles of attack, both turbulence models predict less lift than the wind tunnel results suggest, with SA matching the wind tunnel results a bit closer. Generally the free air simulations predict less than "Step D" , however with the SA turbulence model showing the predicted slope change from Shindo's corrections, even if the high angle of attack variability is still present. The SST turbulence model produced a more noticeable lower lift in comparison to the CFD results for the free air configuration, however for the linear region, the change in $C_{L\alpha}$ is still present and matching expectations for the results. For the UWS20A the SA turbulence model seems to generate more consistent results than the SST turbulence model in lift and drag, and also produced a smoother C_M curve as well.

For the pitching moment curves for both models, the behavior is more mixed, where the SST turbulence model has a large amount of variation for the points in "Step D"'s linear region. The difference in slopes for the linear, low angle of attack region for the pitching moment curve is more than what the wing tunnel results predict, however the greater slope of the CFD results also impacts this value as well. And with the additional vertical offset seen as the pitching moment curves are

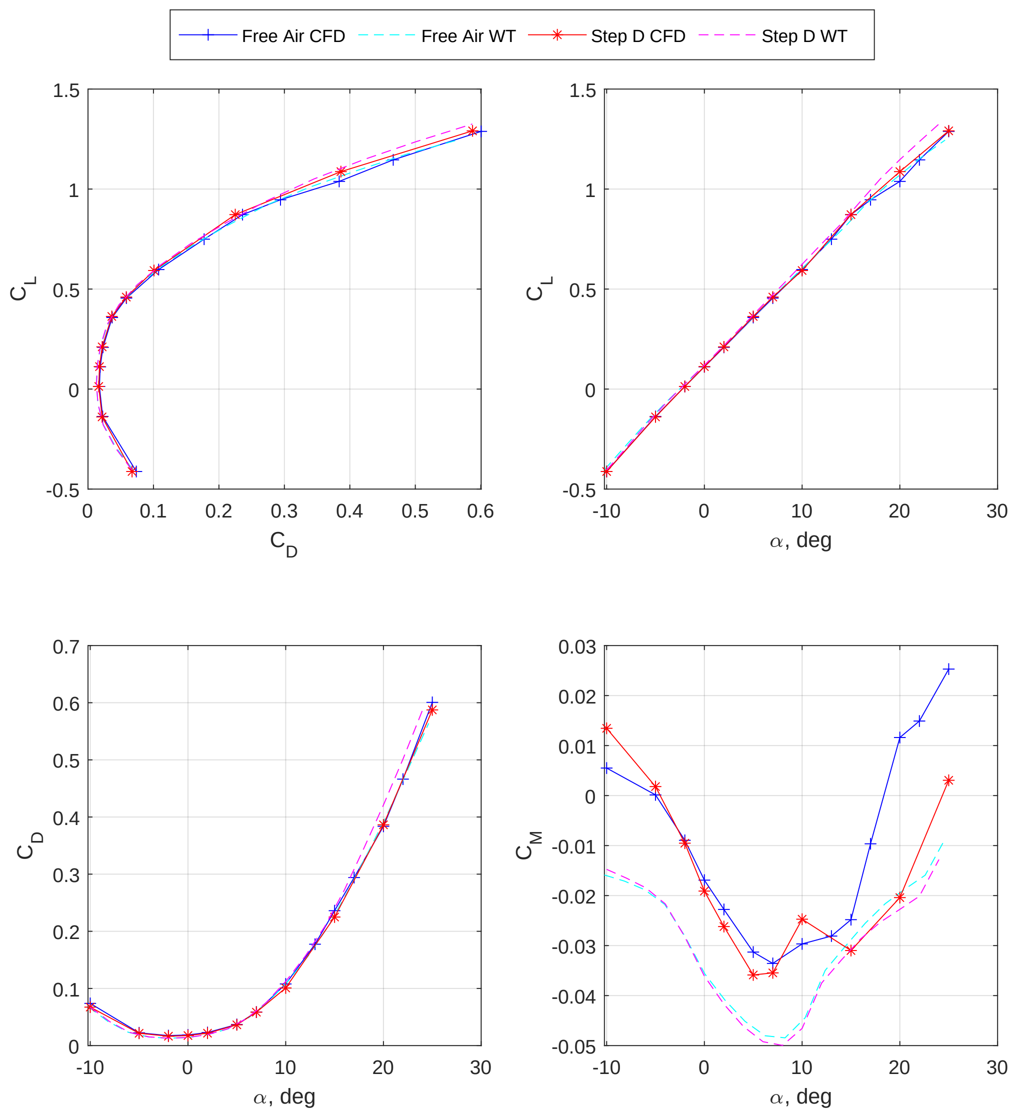

Figure 7.3: Comparison of the pre and post Wall corrections application for both the Wind Tunnel results and the CFD with the SA turbulence model for the UWS21A

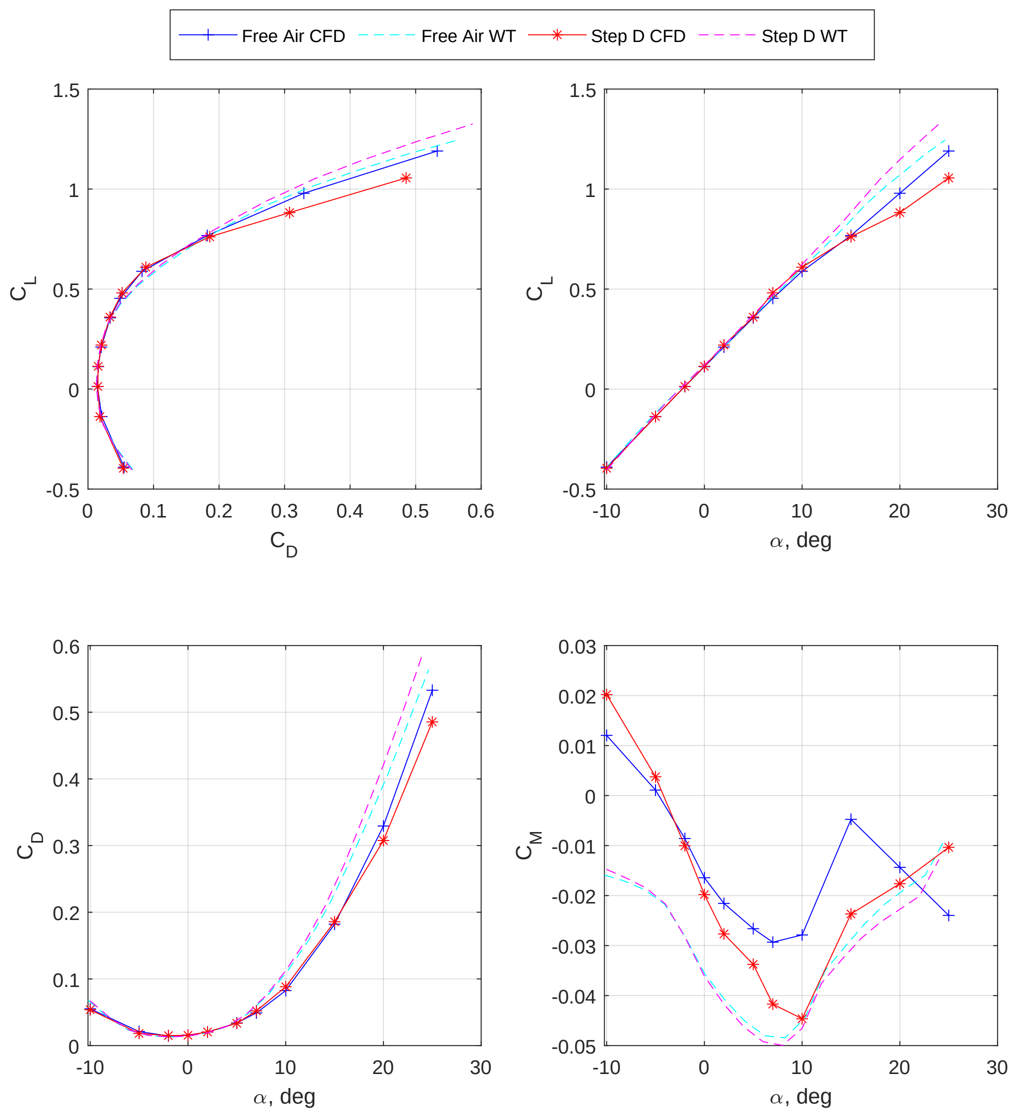

Figure 7.4: Comparison of the pre and post Wall corrections application for both the Wind Tunnel results and the CFD with the SST turbulence model for the UWS21A

slightly rotated as well, so the pitching moment correction for the UWS20A will need to be revised as well.

7.3 Comparison of CFD Wall Corrections to Shindo's Wall Corrections

Noting the large differences between the wind tunnel results and the CFD results, Shindo's correction was applied to "Step D" results to see the difference between the free air case and the corrected "Step D" results. These comparisons enable showing that based on the CFD corrections, the standard potential flow theory based δ_w and δ_{A_S} values may not be fully appropriate for supersonic aircraft configurations.

7.3.1 W15

Noting that for the W15 which is a tail off configuration would not have the effects of the pitching moment correction, and has the driving parameter for this wall correction being δ_w. Applying the value of δ_w used from the wind tunnel results, it generates a correction smaller in magnitude than what the CFD results suggest. The comparison for the SA turbulence model on the W15 wing is shown in Figure 7.7 and the comparison for the SST turbulence model is shown in Figure 7.8. Both turbulence models produce similar results, where applying Shindo's corrections to the in tunnel W15 results causes the change in slope and flattening of the curves due to the addition of the $\Delta\alpha_{wc}$, the changes from Shindo's correction are far smaller in magnitude what corrections are produced from the free air simulation results for both. However, the trends that Shindo's correction implies (slopes decreasing and curves being stretched horizontally) are in the right direction for low angles of attack. For the high angles of attack where there is flow separation and regions where the turbulence models become less reliably, the simulation results are more varied.

Looking specifically at the low angles of attack of the model, the magnitudes of the corrections of the CFD wall and blockage corrections are plotted against Shindo's wall and blockage corrections. The results for the SA turbulence model are shown in Figure 7.9 and for the SST turbulence model in Figure 7.10. Noting that the magnitude of Shindo's corrections are far less than what CFD predicts in the low angle of attack region, but also provide a more monotonic and consistent correction than the CFD based corrections, where the ΔC_M has the greatest differences beyond a simple slope change where the ΔC_M changes direction at 5° AOA where it instead becomes more positive, a

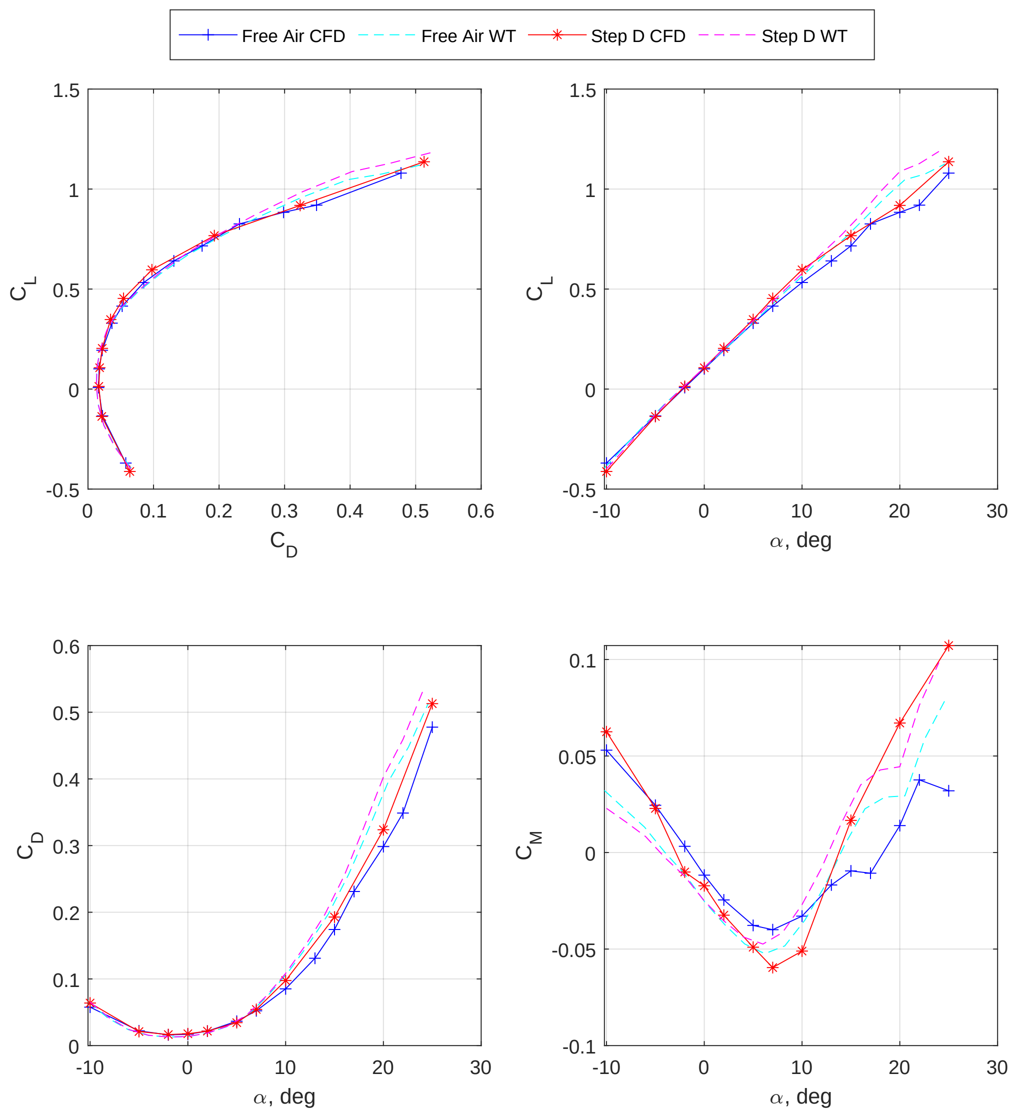

Figure 7.5: Comparison of the pre and post Wall corrections application for both the Wind Tunnel Results and the CFD with the SA turbulence model for the UWS20A

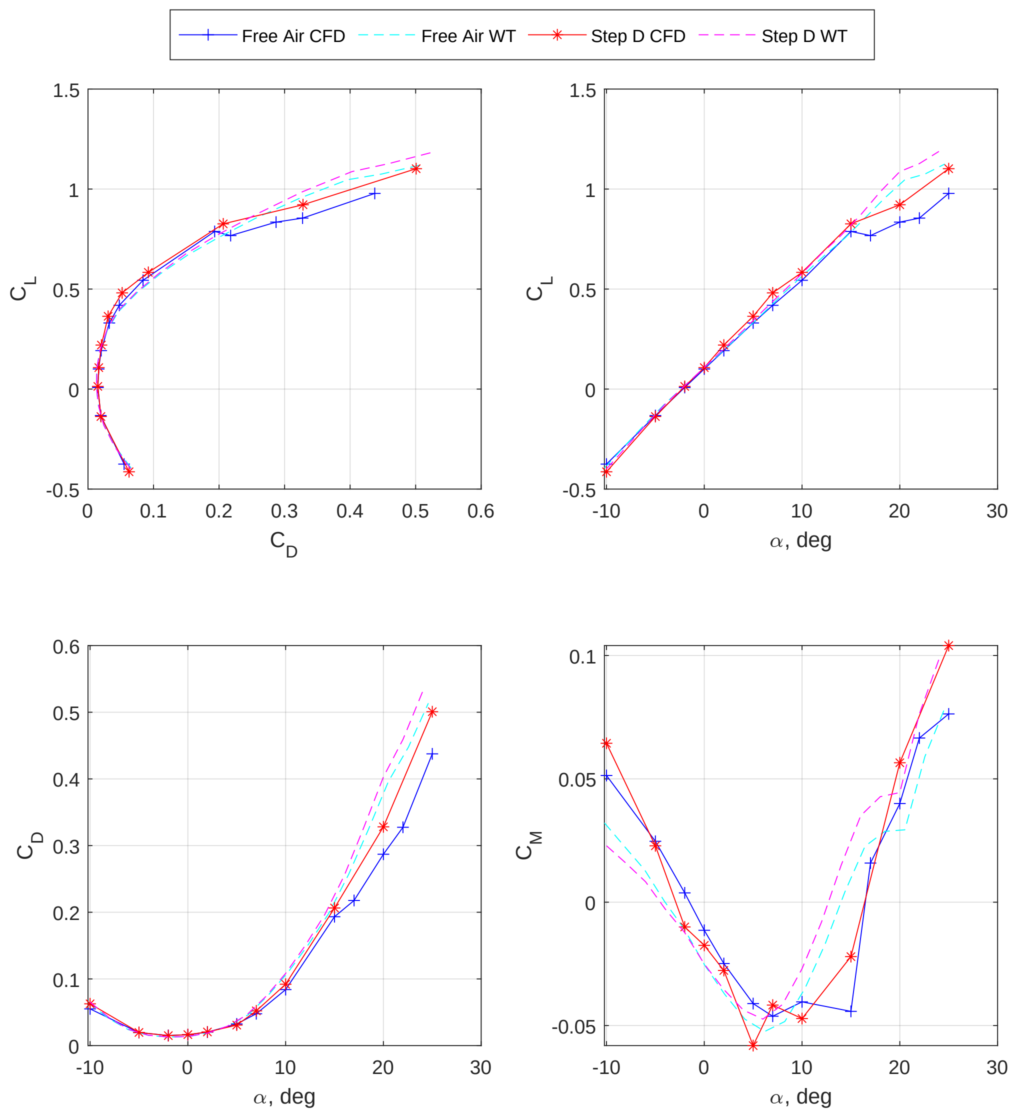

Figure 7.6: Comparison of the pre and post Wall corrections application for both the Wind Tunnel Results and the CFD with the SST turbulence model for the UWS20A

function of the delayed pitch-break that the model experiences, and the kink noted in the "Step D" results from above where the in tunnel case matches the difference in pitch break points for the in tunnel vs free air case for the W15 wing. Additionally, for the low angle of attack range, the SA and SST turbulence models yield near identical results.

7.3.2 UWS21A

For the UWS21A configuration, where a horizontal tail is installed on the model, all of Shindo's wall and blockage corrections are applied, where both δ_W and δ_{A_S} are both used. Unlike the W15 case, for low angles of attack, the differences between "Step D" and the free air simulations are closer to each other for C_L and C_D, and where for the free air simulations end up having more lift than the in tunnel results. The results of Shindo's method with KWT supplied wall correction constants applied to the in tunnel CFD results compared against the free air CFD results are shown in Figure 7.11 for the SA turbulence model, and in Figure 7.12 for the SST turbulence model. Here, Shindo's wall corrections are similar to the simulated results generated from the SA and SST turbulence models for lift, noting that the lift slope for the SA turbulence model is about the same for "Step D" and the free air simulation. Disregarding the differences in high angle of attack behavior due to break down with the turbulence models in regions of flow separation, the slopes of the pitching moment curves both need to be adjusted more for both turbulence models. In both cases drag is under-predicted by Shindo's corrections more than what the free air simulations show.

For the magnitude of Shindo's wall corrections compared to the magnitude of the CFD predicted wall corrections, the comparisons for the SA turbulence model are shown in Figure 7.11 for the SA turbulence model, and in Figure 7.12 for the SST turbulence model. Notably, for the SST turbulence model, the SST CFD wall corrections for lift are around the same as the Shindo's predictions, but slightly less overall. For the corrections for the SA turbulence model, the CFD wall corrections are far smaller than Shindo's wall corrections would predict, suggesting the CFD corrections have a lower value of δ_w. For both, the pitching moment corrections are far larger for CFD than for Shindo's method with the KWT applied value of δ_{A_S}. For the drag corrections, the SST CFD correction matches Shindo's correction for angles of attack greater than 0°, however it does deviate at lower angles of attack. For the SA turbulence model, the C_{D0} is overestimated by the SA turbulence

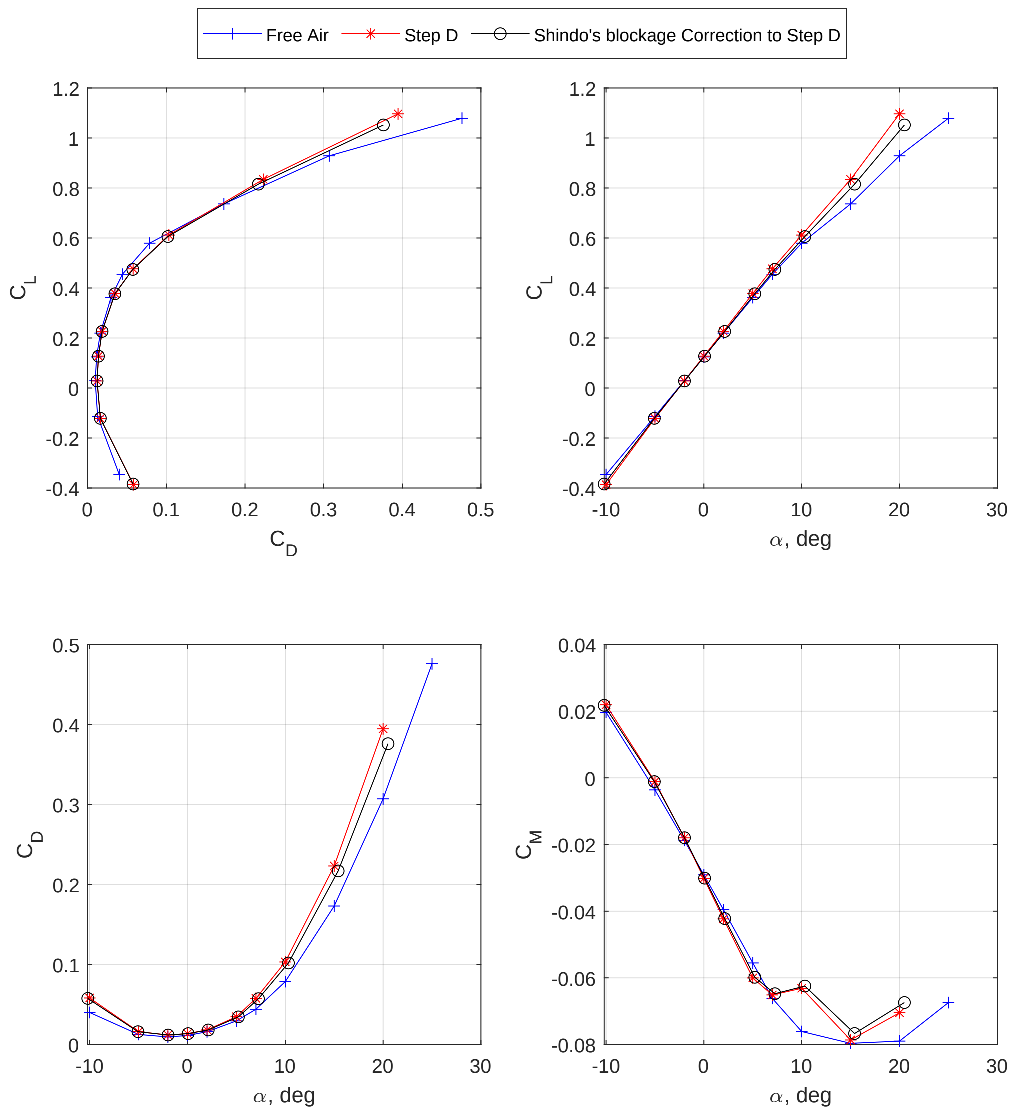

Figure 7.7: Comparison of the "Step D" simulation, Shindo's correction applied to the "Step D" simulation and the Free air simulation with the SA turbulence model for the W15A wing.

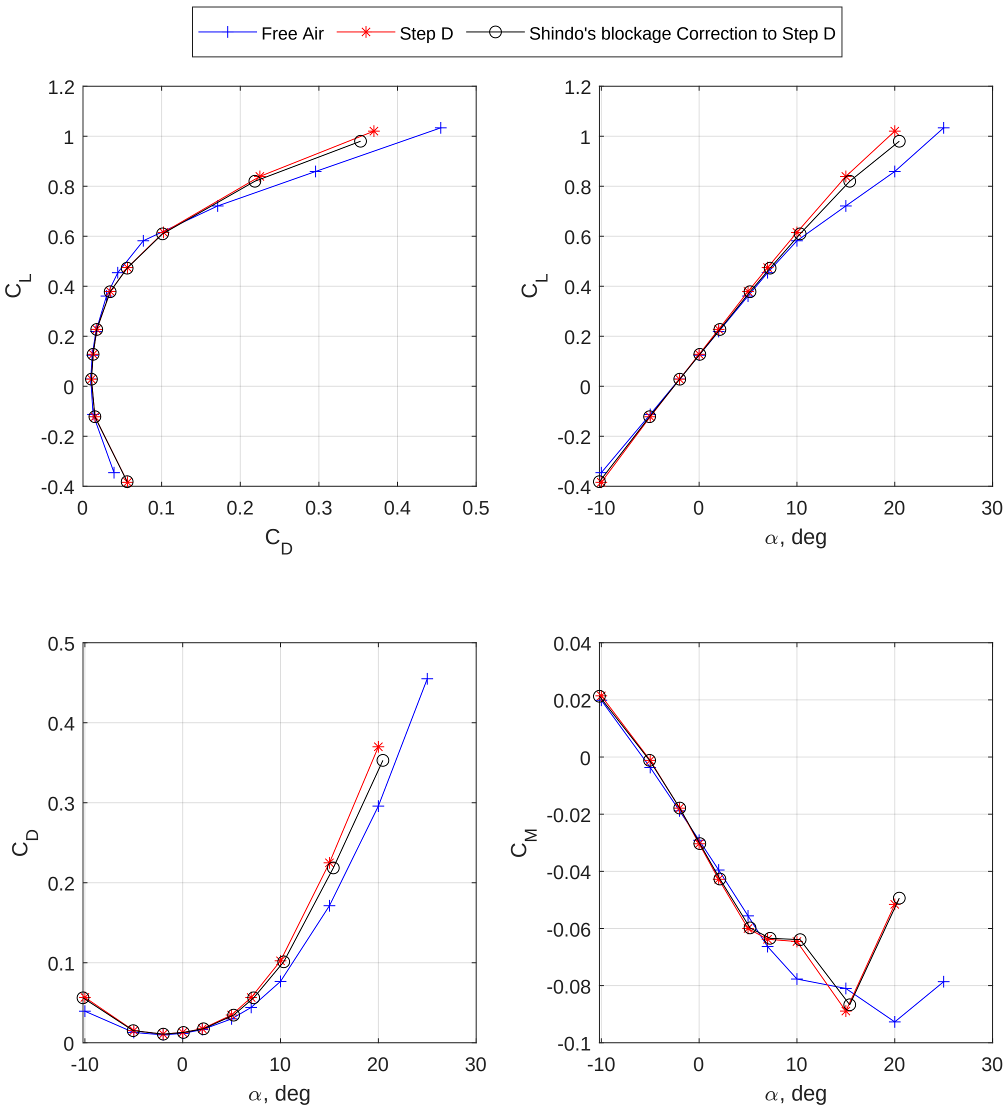

Figure 7.8: Comparison of the “Step D” simulation, Shindo’s correction applied to the “Step D” simulation and the Free air simulation with the SST turbulence model for the W15 wing.

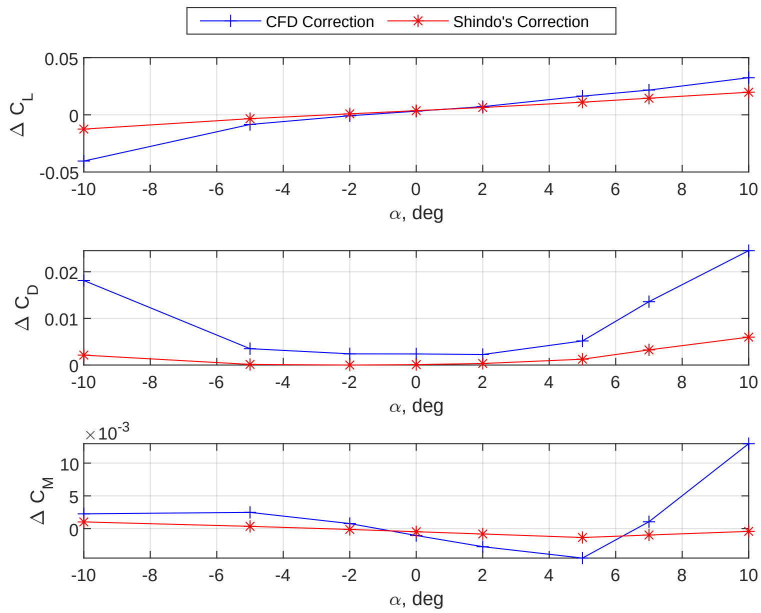

Figure 7.9: Comparison of the difference in Shindo's Wall corrections and the CFD wall corrections for the SA turbulence model for the W15 wing.

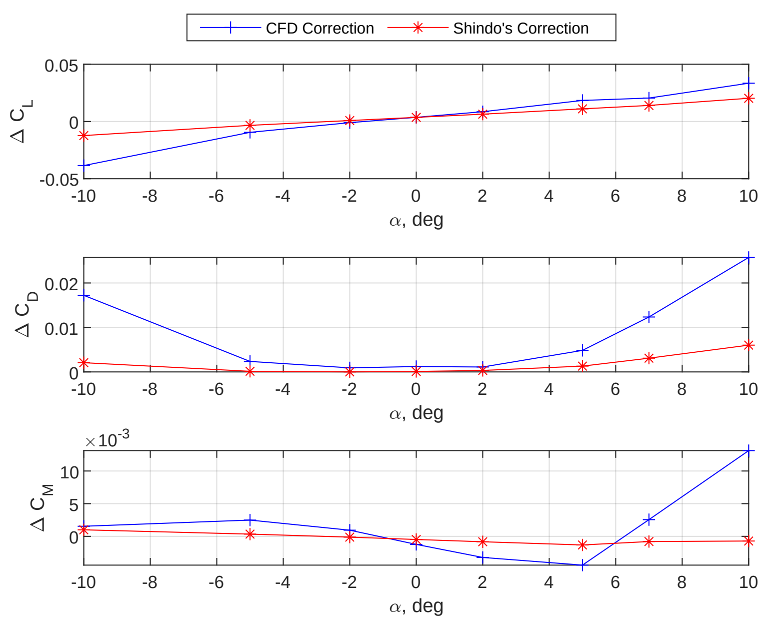

Figure 7.10: Comparison of the difference in Shindo's Wall corrections and the CFD wall corrections for the SST turbulence model for the W15 wing.

model, causing the reverse of the expected behavior for the model.

7.3.3 UWS20A

For the UWS20A configuration, the comparison between Shindo's corrections applied to "Step D" with the standard KWT values of δ_w and δ_{A_S} and the CFD free air configuration is shown in Figure 7.15 for the SA turbulence model and in Figure 7.16 for the SST turbulence model. For both turbulence models, the results have a greater amount of noise with non-consistent curves, and dramatic changes in behavior at high angles of attack. This configuration in particular suggests that to capture the full range of values for the wall corrections δ_w and δ_{A_S} need to change significantly across the entire AOA range. While for high angles of attack, Shindo's correction seems to match the changes between "Step D" and the free air case, however for lower angles of attack, a larger correction is needed, mostly shown in the C_L vs C_D plot. The pitching moment curves exhibit changes at high angles of attack for the SA model, but are instead mostly consistent for the SST turbulence model, but the pitching moment curve in the SST turbulence model has far more outlier points on it which break the generally expected smooth behavior of pitching moment curves. In either case for both, a far larger correction to the pitching moment slope is required, with the supplied δ_{A_S} value from the KWT being insufficient to adjust for the changes. The drag correction is surprisingly accurate for both at high angles of attack, similarly for lift as well.

Looking at the magnitude of the CFD wall corrections and the ones determined with Shindo's and the standard wall corrections produce Figure 7.17 for the SA turbulence model and Figure 7.18 for the SST turbulence model. For both cases, the value of δ_w needs to be increased to match the CFD corrections, where there needs to be large change in the slope of the lift and drag curves than what Shindo's correction predicts. Additionally, these also for that for both turbulence models, the pitching moment curve needs to be flattened more to match the free air simulations. For the pitching moment simulated in the SST turbulence model, the results are a bit more varied in value, but if a line of best fit were to be passed through, the slope generated from Shindo's corrections will need to be increased significantly to match the corrections from the free air simulation.

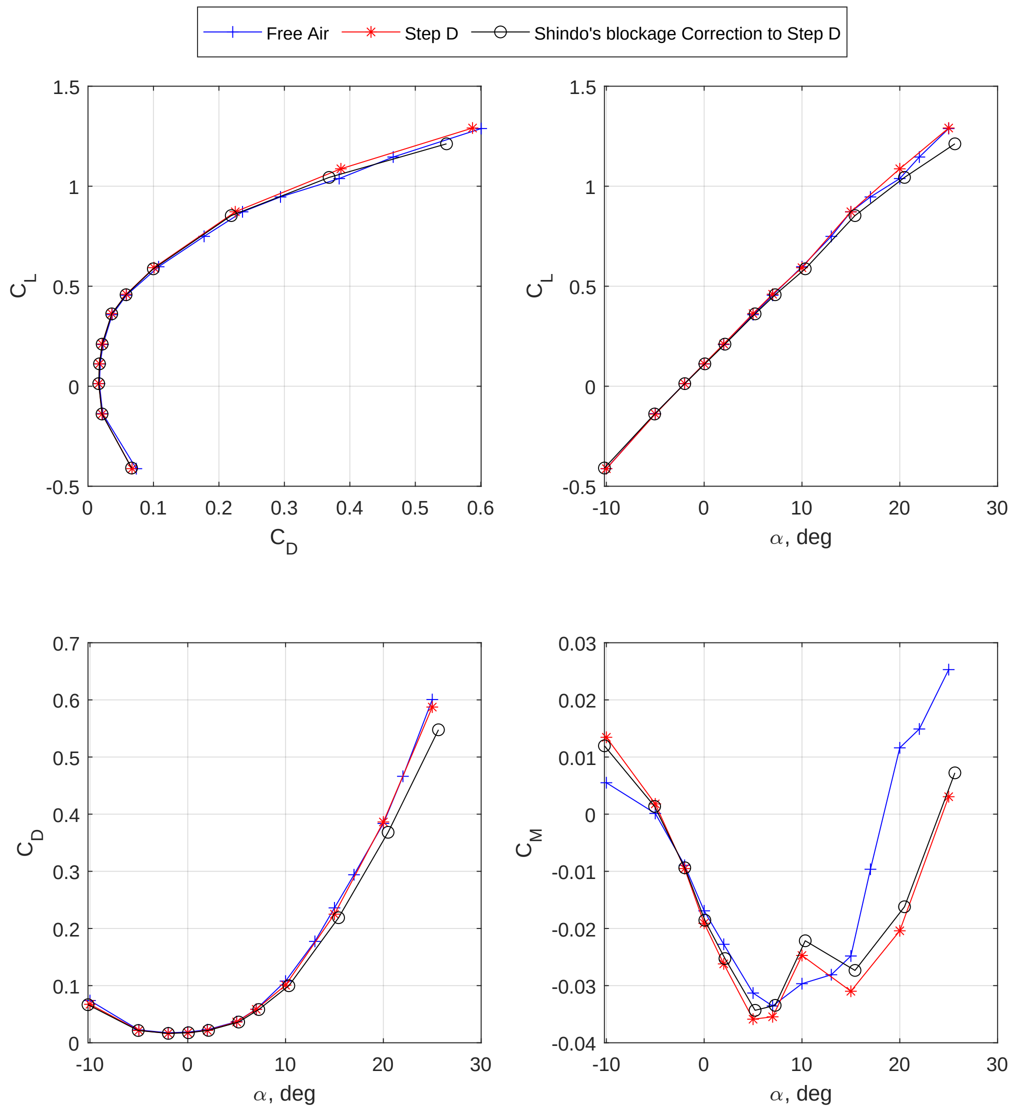

Figure 7.11: Comparison of the "Step D" simulation, Shindo's correction applied to the "Step D" simulation and the Free air simulation with the SA turbulence model for the UWS21A configuration.

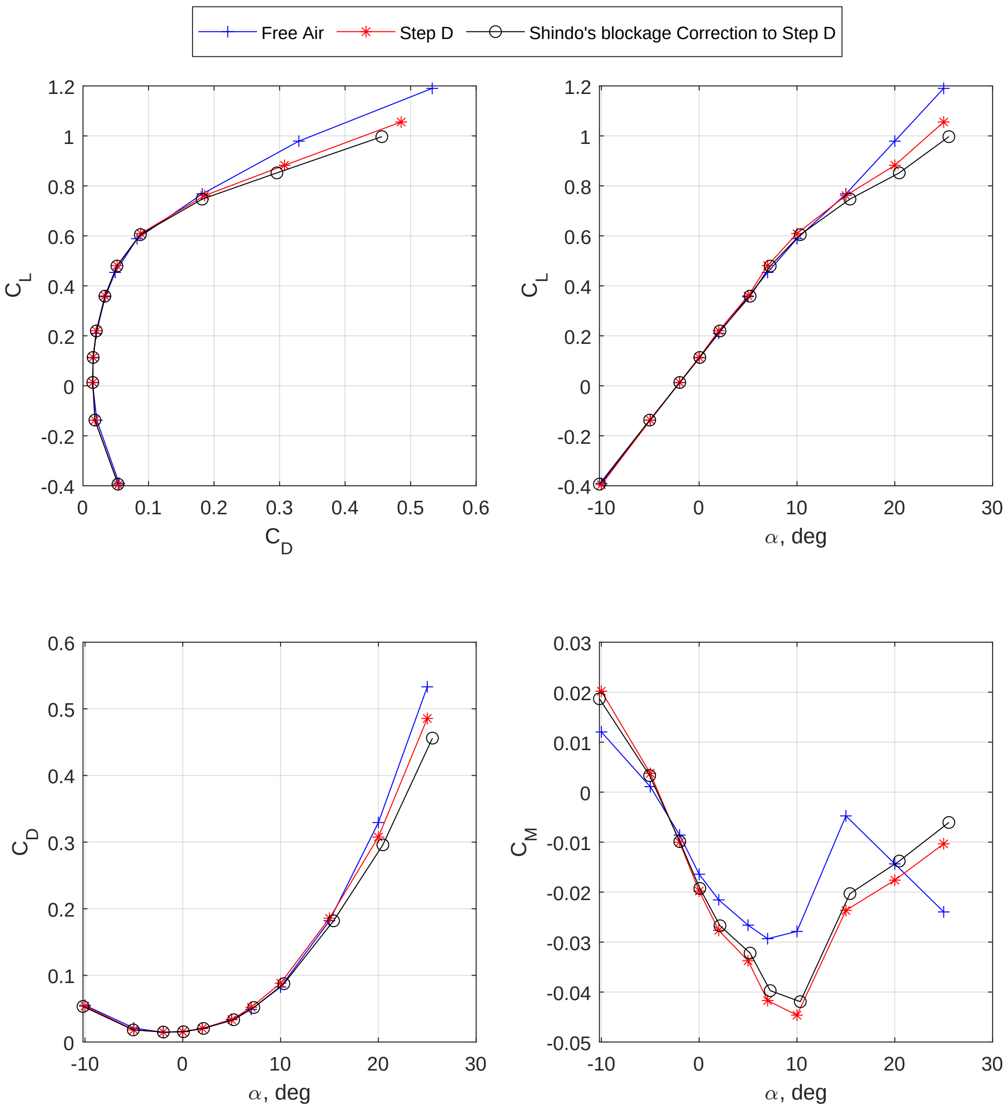

Figure 7.12: Comparison of the “Step D” simulation, Shindo’s correction applied to the “Step D” simulation and the Free air simulation with the SST turbulence model for the UWS21A configuration.

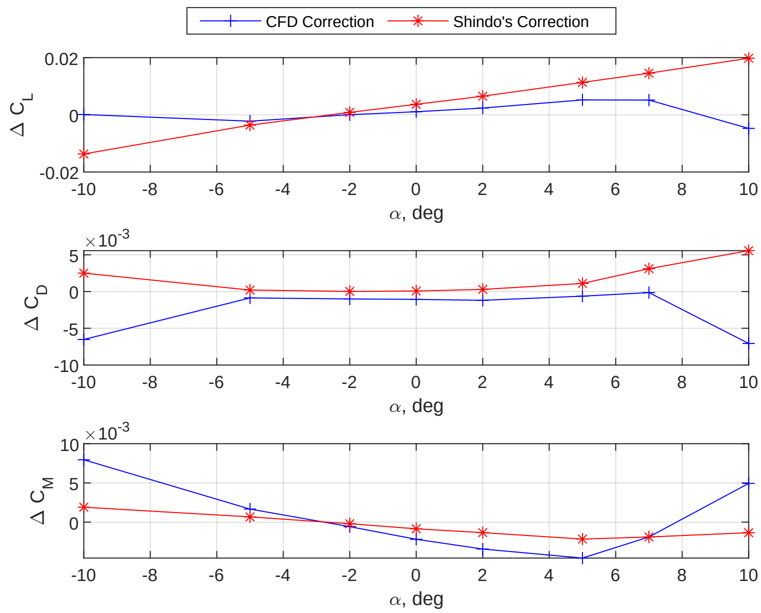

Figure 7.13: Comparison of the difference in Shindo's Wall corrections and the CFD wall corrections for the SA turbulence model for the UWS21A configuration.

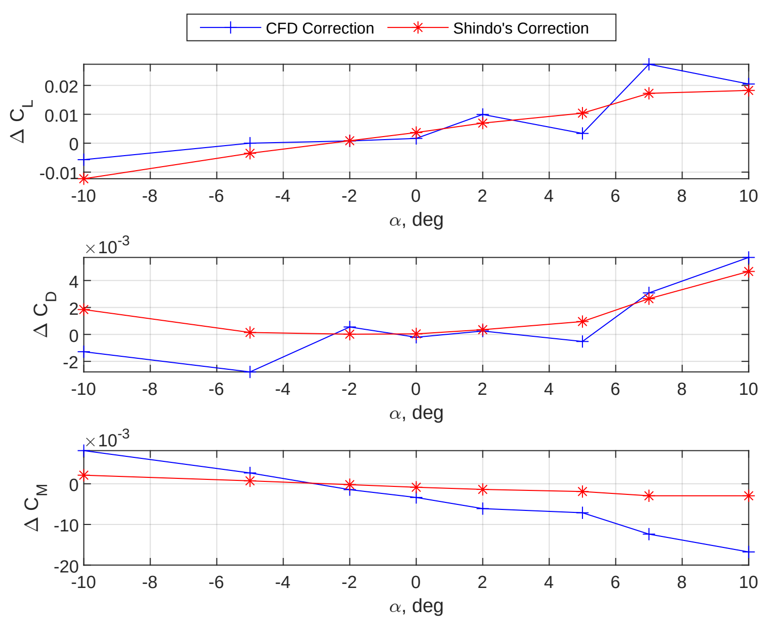

Figure 7.14: Comparison of the difference in Shindo's Wall corrections and the CFD wall corrections for the SST turbulence model for the UWS21A configuration.

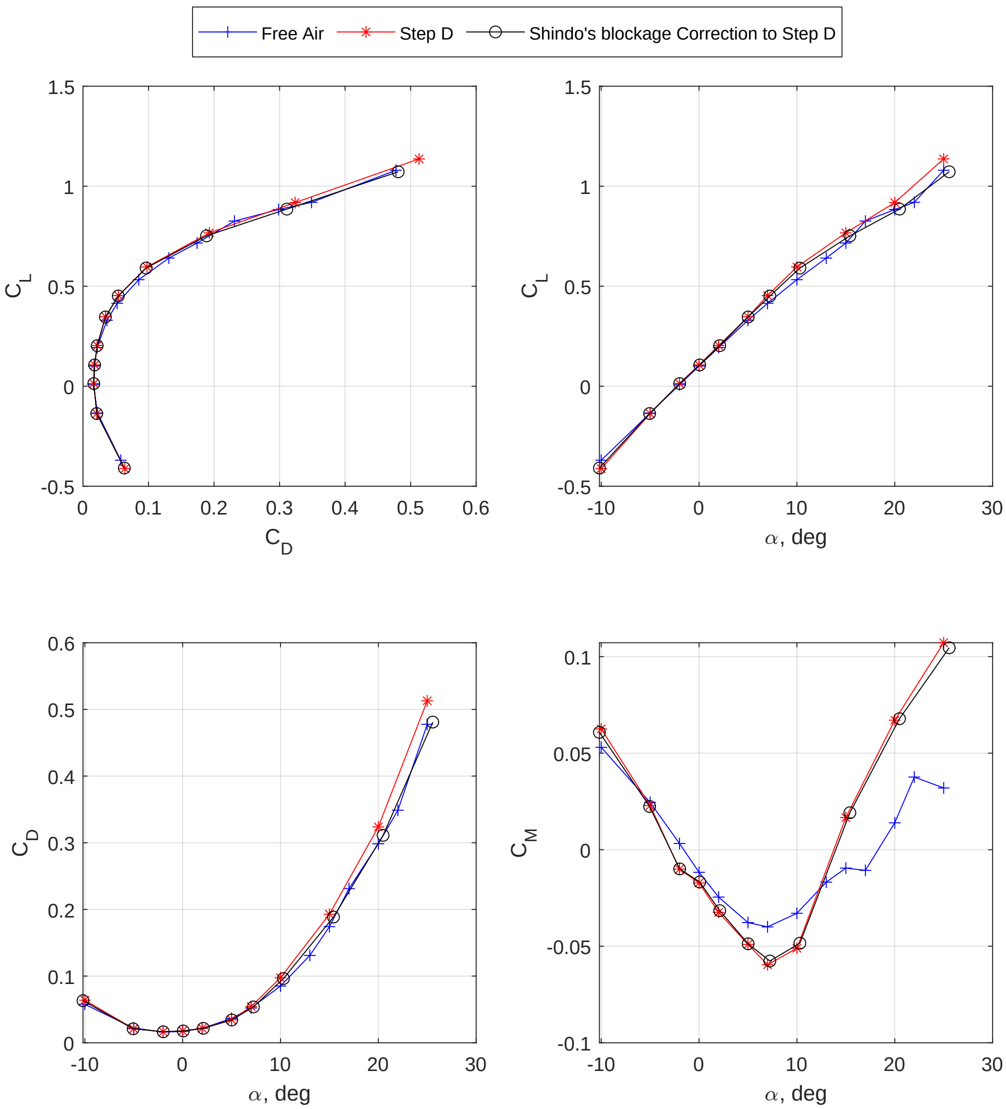

Figure 7.15: Comparison of the “Step D” simulation, Shindo’s correction applied to the “Step D” simulation and the Free air simulation with the SA turbulence model for the UWS20A configuration.

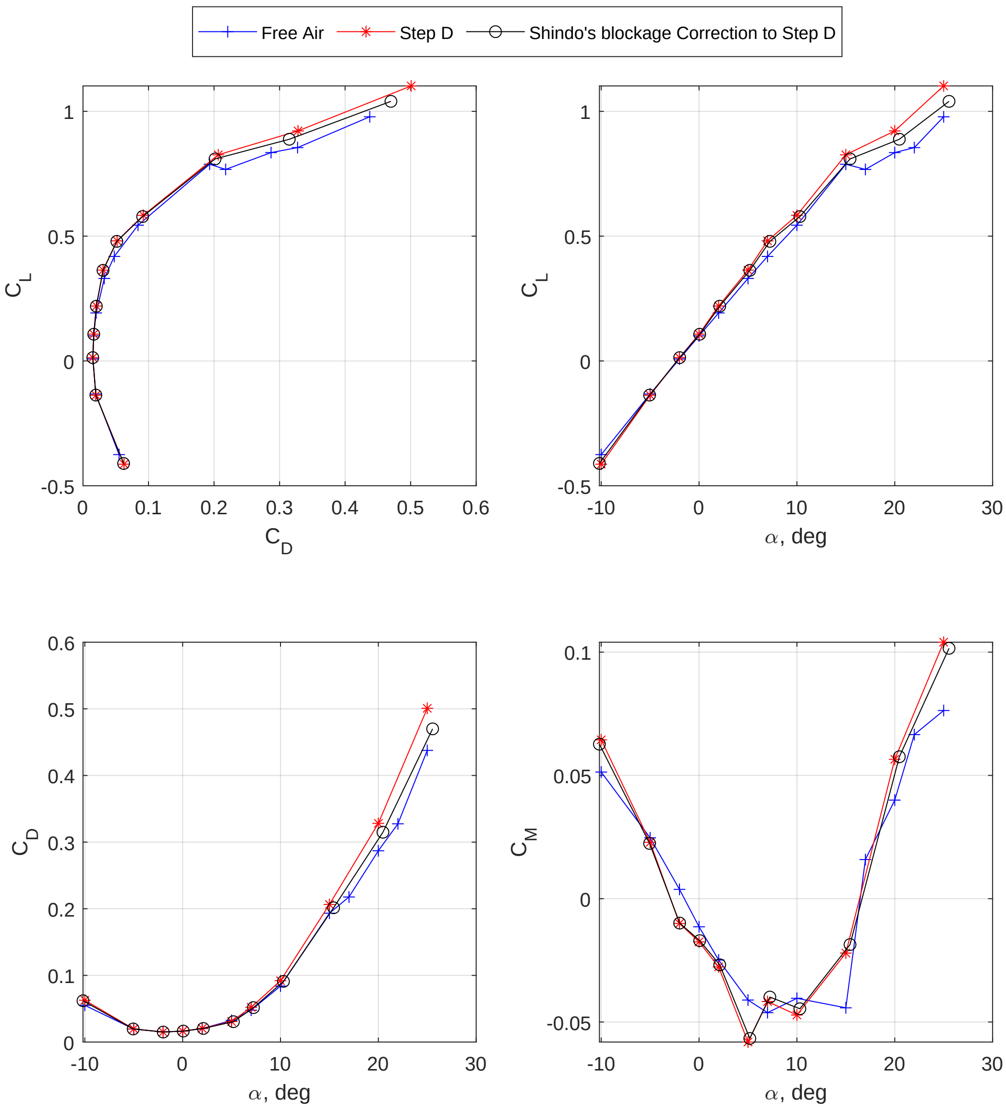

Figure 7.16: Comparison of the “Step D” simulation, Shindo’s correction applied to the “Step D” simulation and the Free air simulation with the SST turbulence model for the UWS20A configuration.

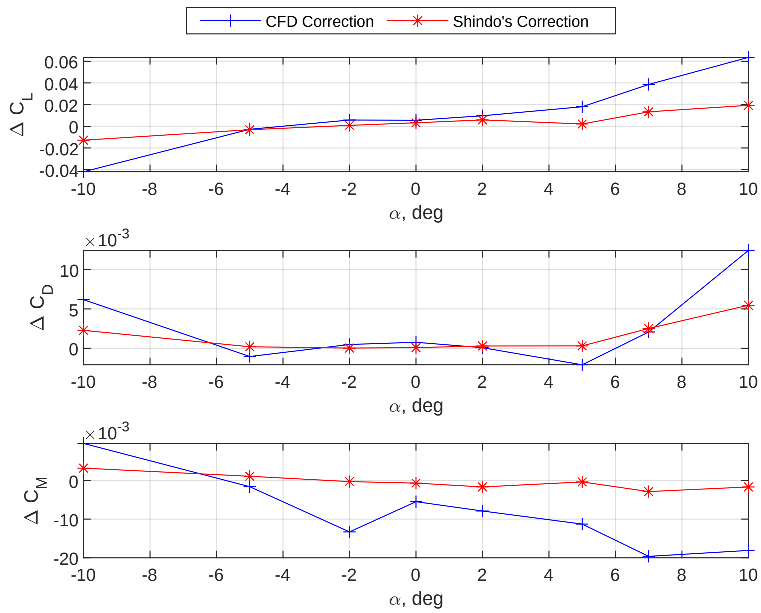

Figure 7.17: Comparison of the difference in Shindo's Wall corrections and the CFD wall corrections for the SA turbulence model for the UWS20A configuration.

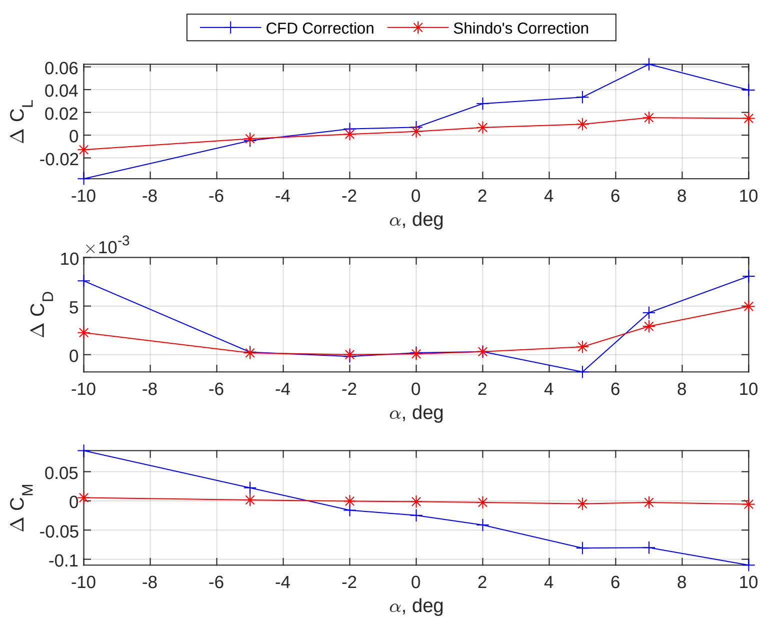

Figure 7.18: Comparison of the difference in Shindo's Wall corrections and the CFD wall corrections for the SST turbulence model for the UWS20A configuration.

7.4 CFD Generated New Wall Corrections Constants

To calculate a new set of δ_w and δ_{A_S} values for each of the supersonic configuration, a slope matching optimization tool was used. Analyzing the near-linear regions of behavior of the models at the low angles of attack $-10° \leq \alpha \leq 10°$, a linear fit was applied to the slope of both "Step D" corrected with Shindo's and the free air results for lift and pitch. The difference in slopes was then used to adjust the value δ_w to increase or decrease the slope of the "Step D" corrected by Shindo's method. This continued until the slopes matched within 0.1%. Once the new δ_w value was obtained, then the linear region of the pitching moment curve ($-10° \leq \alpha \leq 7°$) was similarly fit with the new δ_{A_S} value to match the slopes at that location. Comparisons of the magnitudes of the new corrections are plotted below alongside the new wall correction constants generated for the adjusted Shindo's correction.

7.5 W15A

For the W15, there is no need to calculate the value of δ_{A_S} where the is no pitching moment correction due to the lack of a tail. The new values for δ_w are shown in Table 7.1 where there agreement between the two turbulence models with a difference of 0.0014 between them. This new δ_w is 2.51 times greater than the ones determined from NACA report 547. The results of the new correction magnitudes for the new wall correction constants are shown in Figure 7.19 for the SA turbulence model and in Figure 7.20 for the SST turbulence model. Notably for both, the drag corrected with Shindo's method is still underestimated in comparison to the CFD predicted delta. However, both lift and pitch are brought more into alignment with the curves mostly overlapping, expect once the pitch break is hit. Either way, these corrections still suggest for cranked delta wings without fuselages that Shindo's corrections don't fully capture the wall effects as expected for drag, and require different values for the parameter, δ_w at different angles of attack.

7.6 UWS21A

For the UWS21A configuration that has a horizontal stabilizer, both δ_w and δ_{A_S} can be assessed. Noting that the SA and SST turbulence models had some different behaviors, notably with the fact that for the UWS21A SA simulations, the SA turbulence model had the CFD corrections be

Table 7.1: New values of δ_W based on CFD results for W15A

Turbulence Model	δ_W
SA	0.2865
SST	0.2851

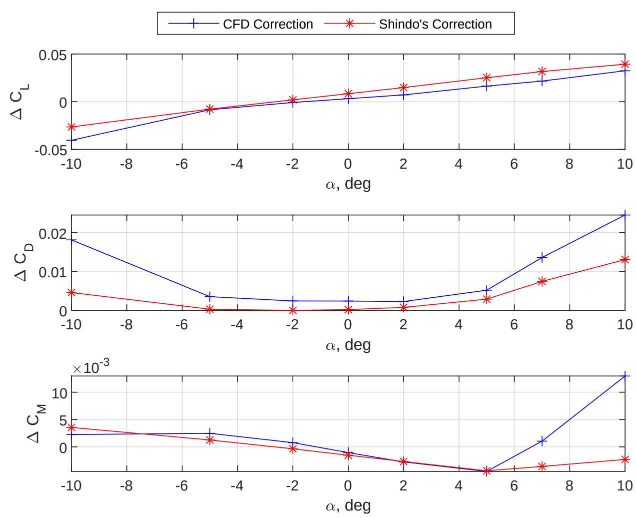

Figure 7.19: The new wall correction constants applied with Shindo's wall correction for the W15 wing with the SA turbulence model.

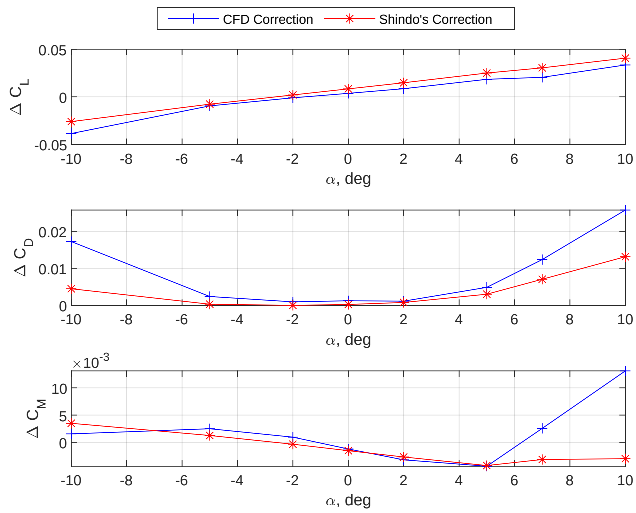

Figure 7.20: The new wall correction constants applied with Shindo's wall correction for the W15 wing with the SST turbulence model.

Table 7.2: New values of δ_W and δ_{A_S} based on CFD results for UWS21A

Turbulence Model	δ_W	δ_{A_S}
SA	0.0083	-0.3156
SST	0.1047	-0.3897

smaller in magnitude for lift than Shindo's corrections were. However, the slope of the pitching moment CFD corrections were greatly increased in comparison to the ones predicted by Shindo's corrections. The new wall correction constants are specified in Table 7.2, where there are some differences in the values between the two turbulence models. These differences are not unexpected with the prior trends of the CFD to the KWT applied wall and blockage corrections, where the differences between the corrections were reversed. Notably, the SST turbulence model indicates that δ_w should only decrease by about 10%, while SA suggests that δ_w should not be applied at all. For the δ_{A_S} constant, there is a difference between the two methods of 0.0741, which is nearly the magnitude of the KWT determined value for δ_{A_S} where the new values are 3.73 and 4.61 times greater than the normally calculated value. The corrections to lift, drag, and pitch are shown in

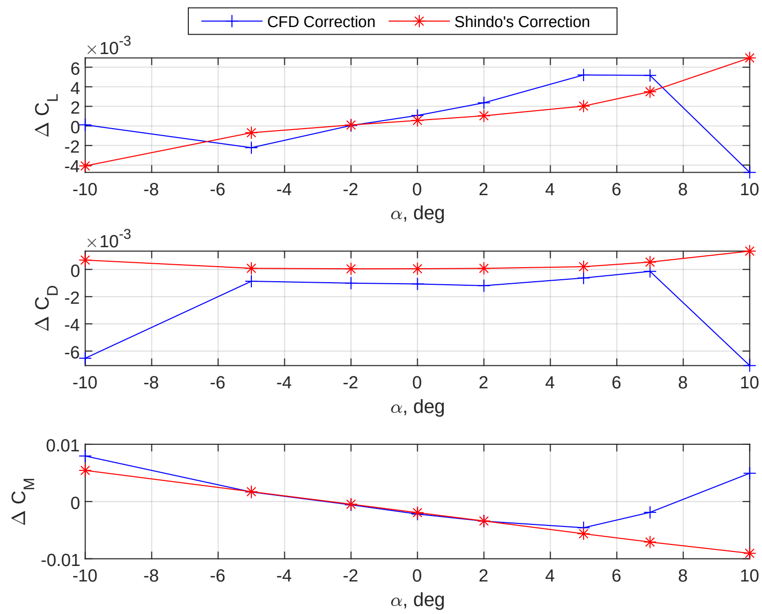

Figure 7.21: The new wall correction constants applied with Shindo's wall correction for the UWS21A configuration with the SA turbulence model.

Figure 7.13 for the SA turbulence model and Figure 7.14 for the SST turbulence model. Unlike the W15 wing, the lift slopes are more matching the same fitted line through the points rather than an exact fit due to the larger differences between "Step D" and free air results. The SST turbulence model provides slightly better results than the SA turbulence model, where the CFD results more oscillate around Shindo's method with the new correction. For the pitching moment curve, the size of the magnitudes of the corrections is very similar for $-5° \leq \alpha \leq 5°$, with the SST model's accuracy carrying to 7° and $-10°$ AOA before large deviations are seen, while for the SA turbulence model the CFD corrections are more positive than what Shindo's would predict. That is the region where the slope of the pitching moment curve starts to change for the SA turbulence model so it's more expected.

7.7 UWS20A

For the UWS20A T-Tail configuration, the value of δ_{A_S} should be expected to be different than the UWS21A, as the location of the tail is different in the tunnel and closer to the ceiling of the tunnel

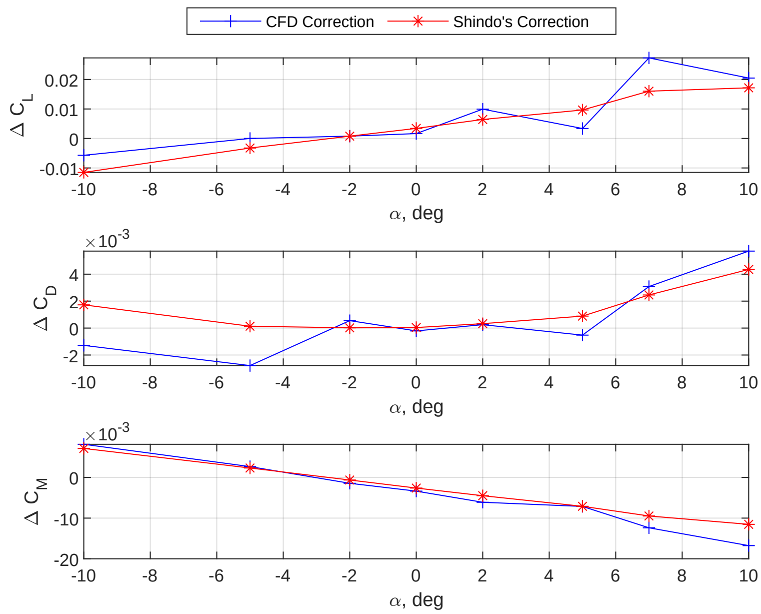

Figure 7.22: The new wall correction constants applied with Shindo's wall correction for the UWS21A configuration wing with the SST turbulence model.

that than the UWS21A configuration. For the CFD based updated values for δ_w and δ_{A_S} are the largest out of the three cases, as shown in Table 7.3. There is significant variation between the two turbulence models, as for δ_w has a difference of 0.0575 between the SA and SST turbulence values, and there is a 0.1336 difference between the CFD generated values for δ_{A_S}, which is nearly double the KWT calculated value for δ_{A_S}. The comparison of Shindo's correction with these new CFD generated wall correction constants is shown in Figure 7.23 for the SA turbulence model and in Figure 7.24. For both, the magnitude of the lift corrections fit quite well, and the drag corrections perform similarly, where large deviations in drag only occurs at $\alpha = 5°$, before the CFD results suggest a smaller correction to C_D than Shindo's method with the new wall correction constants. For pitching moment, there is a slight vertical offset in C_M between the corrections, however the slopes of both corrections are mostly matched, with the CFD generated correction at $\alpha = -2°$ is more than likely a simulation deviation rather than an aerodynamic behavior. So while the wall correction constants changes are far larger, these do match with the expected results from the CFD wall and blockage corrections.

Table 7.3: New values of δ_W and δ_{A_S} based on CFD results for UWS20A

Turbulence Model	δ_W	δ_{A_S}
SA	0.4478	-0.5146
SST	0.5053	-0.3810

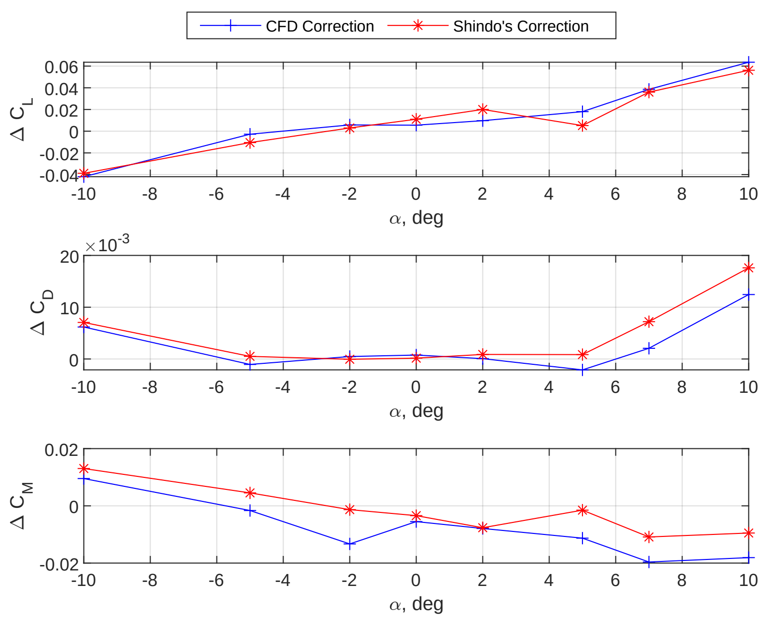

Figure 7.23: The new wall correction constants applied with Shindo's wall correction for the UWS20A configuration with the SA turbulence model.

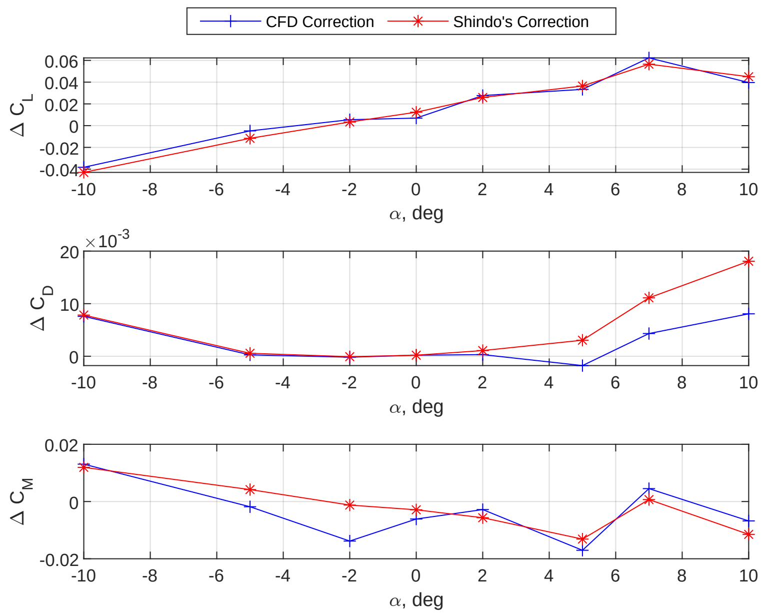

Figure 7.24: The new wall correction constants applied with Shindo's wall correction for the UWS20A configuration wing with the SST turbulence model.

7.8 Summary

For long-slender delta wing configurations, Shindo's process itself can capture the changes in slope for lift and pitching moment, however the standard wall correction constants that are generated from NACA report 547 [5] are insufficient to capture the true value of the corrections based on the CFD results. This leads to the conclusion that a larger study in the future is needed for wall correction constants for delta wings in particular with a more parametric and systematic approach with a larger dataset and ability to match the setup presented in NACA report 547 before moving onto wings with greater sweep.

Chapter 8
CONCLUSION

For wind tunnel data to be as useful to the customer as possible, a series of corrections needs to be applied to the data in order to remove the effects of the tunnel on the model. Computational Fluid Dynamics requires the modeling of certain aerodynamic behaviors in order to be efficiently used for most modern aerospace applications, with RANS solvers still being the primarily CFD option used for exterior aerospace flows. Neither wind tunnel testing or CFD produces data that perfectly represents the behavior of the model that is being tested/simulated as an aircraft in free flight. The knowledge of their weakness are necessary, but both can be combined and compared together to get a better understanding of the aerodynamics of a test vehicle.

Traditional wind tunnel testing relies on a set of corrections that were often originally developed over 50 years ago with a set of assumptions that may be more accurate for certain configurations than others. For model specific corrections, such as the 3-step Tare and Interference correction are time intensive to complete and offer little in the way of new aerodynamic data for the test, they only serve to bring the data closer to how the final vehicle will perform. This is important, however for expensive wind tunnel time, the time would be better spent testing more configurations. This was especially true for SCALOS where the T&I testing consumed 2 weeks out of a 4 week test, leaving the rest of the test short on time to test other configurations. Additionally for the wide range of tests that SCALOS performed, many more T&I processes should've been completed in order to get a set of more accurate corrections for a larger range of model configurations. This process could've been sped up or negated with a comprehensive set of CFD based corrections.

In this thesis, the wind tunnel corrections for the low speed analysis of a supersonic aircraft configuration were studied using RANS CFD run on STAR-CCM+ to compare against the standard corrections. An analysis of the process of removing the effects of the model mounting system using the 3-step T&I process was produced. Finally, a set of CFD based wall corrections were generated and a new set wake correction constants for Shindo's method were developed for the supersonic configurations. Additionally the SA and SST turbulence models were compared in order to study their effectiveness at modeling supersonic configurations at low speeds.

A build of the baseline configuration of the SCALOS project, the UWS21A was simulated in STAR-CCM+ and compared against CFD results to analyze which components of the wind tunnel model caused the largest differences between the CFD and wind tunnel results. It was found that the horizontal tail caused the largest difference between the CFD and wind tunnel results, producing a C_{M0} offset that was consistent for most of the rest of the studies. Additionally a wing with a new set of airfoils and a realistic twist distribution was implemented in order to generate a set of CFD conversions between data of the W15 and the data of the RW23 wing. This delta was then applied by University of Washington capstone students for their proposed supersonic airliner concept.

The 3-step T&I was interrogated with CFD for 2 different configurations, with the W15 having only a pitch sweep to analyze it's behavior and the UWS21A having both a pitch sweep at 0 slide-slip and a yaw sweep at 0 angle of attack. For these methods it was found that the T&I method performed the best to correct for the changes that came with the simulations of the aircraft in the tunnel without the MSS. A single step CFD correction was applied to the UWS20A model and it was found that the T&I correction applied to the UWS20A, which was derived from the UWS21A was not entirely accurate, and that ideally, more T&I combinations should've been performed had additional time and budget been available.

For an analysis of Shindo's wall corrections on long slender delta wing configurations, it was found that the wall correction constants δ_w and δ_{A_S} were not entirely accurate based on a CFD comparison of the free air configuration to the model in the test section. New wall correction constants were generated based on the low angle of attack region of the flow. It is recommended for future supersonic transport work that a CFD wall corrections analysis should be performed in order to generate more accurate values of the wall correction constants.

Additionally, both the Spalart-Allmaras and Menter Shear Stress Turbulence models were both applied for the T&I process and the Wall Corrections process. Neither turbulence model was found to be vastly superior or to the other in all cases, and both had issues reliably matching the wind tunnel data at high angles of attack for lift, drag and pitch. For low angles of attack, ranging from $-10^\circ \leq \alpha \leq 10^\circ$ both turbulence models generally agreed with each other and produced similar results in most cases and matched well with wind tunnel in lift and drag. Notably, both obtaining the zero lift drag of the model and the zero lift pitching moment of the model was difficult, but producing the general behavior of the model in CFD was attainable. The common weak points of RANS CFD were as expected with heavily vortex dominated flows and separated flow regions were where both turbulence models struggled. The final recommendation is that when analyzing a problem with CFD, multiple turbulence models should be checked to build confidence in a solution and to determine the best model by being the one that matches the closest to experimental results. For meshing of supersonic configurations where flow separation is import to be fully modeled, that the first cell height of the prism layer needs to be around $y^+ < 1$, and that additional mesh density should be generated for the wakes that interact with other components of the model, as those conditions are partially where the CFD solutions generated outlier results.

8.1 Future Work

In general, a greater variation of CFD meshing parameters is recommended by looking at the variations of the SA and SST turbulence models and seeing if any performed better than the general models. The results shown here are rather specific to a narrow set of supersonic configurations as well. The results shown here are not conclusive enough to make general statements about how the T&I process or Shindo's method works for all aircraft configurations, or even all supersonic configurations. The following are proposed future explorations of the concept.

- Perform the T&I analysis on more of the SCALOS designs beyond the UWS21A and the W15. The UWS20A was partially done, but a full analysis would help support the CFD correction generated. Specific configurations would be the analysis of any configurations with the aft deck compared against the W15 aft deck combination tested.

- Expand the T&I analysis to other types of aircraft configurations as well, such as modern transonic transport aircraft (Boeing or Airbus generic airliners) or smaller light sport aircraft with high wings. While the process working for an edge case like Supersonic configurations

- Do a far more detailed analysis of Shindo's wall corrections than what was presented here. A CFD study of a standard high aspect ratio wing alone in a test section and see if CFD supports the same wall correction constants that are derived using the methods from NACA report 547.

- Work on generating a more generic CAD definition of a supersonic configuration to compare and produce a more refined regression surface for wall correction constants for these configurations. The results presented here are quite narrow and most likely are not even extrapolatable to all SCALOS configurations, let alone a company specific design.

- Perform more specific analysis incorporating specific flow qualities of the KWT such as the variations in flow inside the test section and the actual turbulence intensity of the tunnel. These can be applied via settings in STAR-CCM+ and by setting up the inlet of the test section to match the velocity distribution present in the tunnel.

BIBLIOGRAPHY

[1] Livne, E., Nelson, C. P., Soltani, R. M., Ting, K.-Y., Mavriplis, N., Wiersema, K., Cesnik, a. K. I., Carlos E. S., Martins, J. R. R. A., Guimaraes, T. A. M., Cunis, T., Barbosa, G. C., Bertolin, R., Seraj, S., Monteiro, B. B., Alonso, J. J., Kroo, I., Shanbhag, a. S. Y., Tejal K., Magee, T. E., Hayes, P. J., Dorgan, A. J., and Khodadoust, A., "Compilation of Supersonic Configurations at Low Speeds (SCALOS) Final Report and Appendices A – F," Tech. Rep. 20250006613, NASA, 2025. URL `https://ntrs.nasa.gov/citations/20250006613`.

[2] Rodriguez, S., *Applied Computational Fluid Dynamics and Turbulence Modeling*, Springer, 2019.

[3] Barlow, J., Rae, J. W. H., and Pope, A., *Low Speed Wind Tunnel Testing - 3rd edition*, John Wiley & Sons, Inc., 1999. Pages 278 and 281, Figures 730 and 734, ISBN 0-471-55774-9.

[4] Shindo, S., "Simplified Tunnel Correction Method," *Journal of Aircraft. Vol. 32. No. 1*, 1994. https://doi.org/https://doi.org/10.2514/3.46705.

[5] Silverstein, A., and White, A., J., "Report: No. 547 Wind-Tunnel Interference with Particular Reference to Off-Center Positions of the Winf and to the Downwash at the Tail," Tech. rep., NACA, 1935.

[6] Wiersema, K., Ting, K.-Y., Nelson, C. P., and Livne, E., "Supersonic Configurations at Low Speeds(SCALOS): Correlation of CFD / Wind Tunnel Test Results," *AIAA SciTech 2025 Forum*, AIAA Paper, 2025.

[7] Wiersema, K., Ting, K.-Y., Nelson, C. P., and Livne, E., "Wind Tunnel Low-Speed Tare and Interference Corrections: CFD vs Test Results - The Supersonic Configurations (SCALOS) Cases," *AIAA SciTech 2026 Forum*, AIAA Paper, 2026.

[8] Welge, H., Bonet, J., Magree, T., Chen, D., Hollowell, S., Kutzmann, A., Mortlock, A., Stengle, J., Nelson., C., Adamson, E., Baughcum, S., Britt, R., Miller, G., and Tai, J., "N+2 Supersonic Concept Development and Systems Integration," Tech. Rep. CR-2010-216842, NASA, 2010.

[9] Magee, T. E., Hayes, P. J., Dorgan, A. J., and Khodadoust, A., "Dynamic Stability Characteristics for Commercial Supersonic Configurations at Low-Speed Flight Conditions," *AIAA SciTech 2022 Forum*, AIAA Paper 2022-1802, 2022. https://doi.org/10.2514/6.2022-1802.

[10] Magee, T. E., Hayes, P. J., Dorgan, A. J., and Khodadoust, A., "Dynamic Stability Characteristics for Commercial Supersonic Configurations at Low-Speed Flight Conditions – Part II," *AIAA SciTech 2024 Forum*, 2024. https://doi.org/10.2514/6.2024-0900.

[11] Magee, T. E., Hayes, P. J., and Khodadoust, A., "Dynamic Stability Characteristics for Commercial Supersonic Configurations at Low-Speed Flight Conditions – Part III," *AIAA SciTech 2025 Forum*, 2025.

[12] "The University of Washington's Kirsten Wind Tunnel," , 1936-present. URL https://www.uwal.uw.edu/facilities-capabilities/, accessed: May 23rd, 2026.

[13] Rogowski, K. S., K., and Michna, J., "DNS Dataset of a Thick Symmetric Airfoil at Low Reynolds Number: NACA 0018 with LES Comparison," *Journal of Applied Fluid Mechanics*, Vol. 19 No 2., 2026. https://doi.org/https://doi.org/10.47176/jafm.19.2.3738.

[14] Spalart, R., P., and Allmaras, R., S., "A One-Equation Turbulence Model for Aerodynamic Flows," Tech. rep., AIAA-92-0439, 1992.

[15] Menter, K. M., F. R., and R, L., "Ten Years of Industrial Experience with the SST Turbulence Model," *Turbulence, Heat and Mass Transfer*, 2003.

[16] Wilcox, D., *Basic Fluid Mehanics Fifth Edition*, DCW Industries, 2012.

[17] Mavriplis, N., "RANS-CFD Based Assessment of Corrections Applied to the Measured Characteristics of Supersonic Configurations in a Low Speed Wind Tunnel," Master's thesis, University of Washington, 2022. URL http://hdl.handle.net/1773/49591.

[18] Antani, D., and Morgenstern, J., "HSCT High-lift Aerodynamic Technology Requirements," *AIAA Paper 1992-4228*, 1992. https://doi.org/10.2514/6.1992-4228, Guidance, Navigation and Control Conference.

[19] Baize, e., D.G., "1997 NASA High-Speed Research Program Aerodynamic Performance Workshop. Volume I - Configuration Aerodynamics," *NASA*, 1999. Proceedings CP-1999-209691/VOL1/PT1.

[20] Ting, K.-Y., Nelson, C. P., and Livne, E., "Tare & Interference Corrections for SCALOS Configurations tested at the University of Washington's Kirsten Wind Tunnel," *AIAA SciTech 2024 Forum*, 2024. AIAA Paper 2024-0899.

[21] Siemens, "Best Pratices: External Aerodynamics for Aerospace Applications," , 2024. URL https://support.sw.siemens.com/knowledge-base/KB000031728_EN_US.